FEDERAL UNIVERSITY OF SANTA CATARINA - UFSC
TECHNOLOGIC CENTER OF JOINVILLE - CTJ
NAVAL ENGINEERING

Leandro Souza Pinheiro da Silva

Design of an optimized fully submerged point absorber in Santa Catarina, Brazil.

Joinville, 2017

Leandro Souza Pinheiro da Silva

Design of an optimized fully submerged point absorber in Santa Catarina, Brazil.

Final years project submitted to the Federal University of Santa Catarina as part of the requirements for obtaining the degree of Bachelor of Science in Naval Engineering.
Supervisor: Dr. Thiago Pontin Tancredi
Co-supervisor. Dr. Boyin Ding

Joinville, 2017

UNIVERSIDADE FEDERAL
DE SANTA CATARINA

THE UNIVERSITY
of ADELAIDE

This work is a collaboration between the Federal University of Santa Catarina and the School of Mechanical Engineering at The University of Adelaide. Due to the co-supervision, this work was written in English to attend both institutions.

Founded in 1874, The University of Adelaide is the third oldest university in Australia. Since its creation, the university has attracted notable academics of international distinction, which contributed to its international reputation of excellence in education and research for a broad spectrum of areas.

The university is a member of the Group of Eight, which represents the leading research intensive universities in Australia. Moreover, the university is consistently ranked in the top 1% of the universities worldwide and has honored with 5 Nobel prize. The University has over 25,000 students and over 3,500 staff across its three main campuses.

ACKNOWLEDGEMENTS

First and above all, I praise God, the almighty for providing me this opportunity and granting me the capability to proceed successfully.

This line of research would never have been carried out without Dr. Boyin Ding and Nataliia Sergiienko. Their support, guidance, and tutoring were essential to understanding wave energy devices. I also want to thank all the members of the Ocean Wave Energy Research Group at The University of Adelaide, for devoting their time to assist me.

I would like to give a special thank to my friend and supervisor Professor Thiago Pontin Tancredi for his guidance and support. A very special gratitude goes out to all my professors at the Federal University of Santa Catarina, with a special mention to Thiago Fiorentin, André Fujarra, and Sueli Fischer. They were fundamental in my education.

This project is dedicated to my girlfriend Marielle de Oliveira; my family Maria de Fátima, Acácio, João Paulo and Gilmar; and all my friends, which always supported me during my graduation.

ABSTRACT

Ocean wave energy has a significant capacity to contribute to the future of power generation, of which the south of Brazil possesses a valuable amount of wave resources. In this regards, this work initiates with the assessment of the wave resources in the state of Santa Catarina. Subsequently, it optimizes the power extraction of an optimized fully submerged Point Absorber, through the selection of the best power take-off configuration. The methodology adopted in this work, model the physics of Point Absorber in the Spectrum domain, which is relatively new in the wave energy field, and compares the model with time domain simulations available in the literature. Several sensitivity studies are conducted in regular waves, and posteriorly in irregular waves to investigate the wave energy converter performance and select the best design. The final result indicates that a fixed Power Take-off mechanism with a stiffness of 67.5 kN/m and damper of 67.8 kN.s/m provides 18.7kW of power per Point Absorber, resulting in a reasonable solution for the power extraction in Imbituba, Santa Catarina.

Keywords: Wave Energy Converter. Fully Submerged Point Absorber. Santa Catarina. CETO technology.

RESUMO

A energia das ondas oceânicas tem uma capacidade significativa para contribuir para o futuro da geração de energia, do qual o sul do Brasil possui uma valiosa quantidade de recursos de ondas. Baseado nisto, este trabalho inicia com a avaliação dos recursos das ondas no estado de Santa Catarina. Posteriormente, otimiza a extração de energia de um Absorvedor pontual otimizado totalmente submerso, através da seleção da melhor configuração de tomada de força. A metodologia adotada neste trabalho, modela a física do Absorverdor pontual no domínio do Espectro, que é relativamente novo no campo de energia das ondas, e compara com as simulações no domínio do tempo disponíveis na literatura. Vários estudos de sensibilidade são realizados em ondas regulares e, posteriormente, em ondas irregulares para investigar o desempenho do conversor de energia da onda e selecionar o melhor projeto. O resultado final indica que um mecanismo de tomada de força fixo com uma rigidez de 67,5 kN/m e amortecimento de 67,8 kN.s/m fornece 18,7 kW de potência por Absorvedor pontual, resultando em uma solução adequada para a extração de energia em Imbituba, Santa Catarina.

Keywords: Conversor de Energia das Ondas. Absorvedor Pontual Totalmente Submerso. Santa Catarina. Tecnologia CETO.

NOMENCLATURE

Symbols:

Λ	Cross product
∇	Differential operator
$\mathit{\nabla}$	Water displacement
τ	Time dependent function
β	Angle between the wave propagation and the x axis
σ_{ς}	Standard deviation of the sea elevation
δ	Wave Slope
ν	Kinematic viscosity
ρ	Specific mass
$\mathrm{\phi}$	Velocity potential
ϕ	Phase between the force and the buoy displacement
ς	Surface elevation
ς_a	Wave amplitude
ς_{a_n}	Wave amplitude of the n^{th} wave component
λ	Wavelength
ω	Wave frequency
$\vec{\omega}$	Rotation of the velocity field vector
ω_n	Wave frequency of the n^{th} wave component
$\mathit{\Gamma}$	Water displacement in the x direction
$\mathit{\Omega}$	Water displacement in the z direction
ψ_n	Random phase angle of the n^{th} wave component
ξ	Body displacement amplitude
χ	Function that depends on the position x
γ	Peak enhancement factor
ʒ	Function that depends on the position z

Roman letters:

$A(\omega)$	Hydrodynamic added mass
$B(\omega)$	Hydrodynamic damping coefficient
B_{PTO}	Magnitude of the PTO damping
B_{eq}	Equivalent viscous-damping coefficient
c	Wave velocity
C_D	Drag coefficient
c_g	Wave group velocity
D_{buoy}	Diameter of the buoy
D_j	Quasilinear drag coefficient
dm	Differential element of mass
E_p	Wave potential energy per unit of area
E_c	Wave kinetic energy per unit of area
$F_{buoyancy}$	Buoyancy Force
F_{ext}	External forces attached to the body
F_f	Wave/fluid induced forces
F_H	Hydrostatic force
$F_{K\ Hydro}$	Hydrodynamic stiffness force
$F_{mooring}$	Mooring force
F_{PTO}	PTO force
F_R	Radiation force
F_s	Excitation force
g	Gravitational acceleration
H	Wave height
Hs or $H_{1/3}$	Significant height
h	Water depth
k	Wave number
k_n	Wave number of the n^{th} wave component
K_c	Keulegan-Carpenter number
$K_{mooring}$	Stiffness of the mooring system
m_{buoy}	Mass of the buoy

n	Wave component
p	Pressure
p_{atm}	Atmospheric pressure
P_{mean}	PTO mean power absorption
$\mathcal{R}e$	Reynolds number
S_{ς}	Power spectral density of the surface elevation
T	Wave period
t	Time
T_e	Energy wave period
T_z	Mean zero-crossing wave period.
$\vec{U}$	Vector that represents the total velocity
$\mathbb{X}_{inc}$	Incident waves
$\mathbb{X}_{diff}$	Diffracted waves
x	Horizontal position
W	Wave work
z	Location at the vertical axis
$\bar{z}$	Geometric center at the z axis of the differential element of mass
Z	Vertical displacement about its equilibrium position

ABBREVIATIONS

BNDES	*Banco Nacional de Desenvolvimento Econômico e Social*
CTJ	Technologic Center of Joinville
ECMWF	European Centre for Medium-Range Weather Forecasts
ITTC	International Towing Tank Conference
JONSWAP	Joint North Sea Wave Project
MME	*Ministério de Minas e Energia*
OWC	Oscillating Water Column
PSD	Power Spectral Density
PTO	Power-Take-off
UFSC	Federal University of Santa Catarina
UoA	The University of Adelaide
WECs	Wave Energy Converters

LIST OF FIGURES

LIST OF TABLE

TABLE OF CONTENTS

1 INTRODUCTION

Global energy demand has considerably risen over the last decades. Thus, the use of renewable sources of energy is playing a significant role, due to the limited reserve of fossil fuels. Moreover, environmental awareness alerts a need for renewable energy, owing to the concerns about the climate changes and pollution (Karimirad, 2014). In this general context, several types of renewable sources such as the wind, solar and hydro, have been explored to overcome the growing energy demand and environmental issues. However, one primary resource remained insufficiently exploited until the past few decades and has a significant capacity to contribute to the future of energy production, the ocean wave energy (Drew, Plummer and Sahinkaya, 2009).

The harvesting of ocean energy uses wave's kinetic and potential energy to produce power. This type of energy carries a substantial amount of power that can be indeed advantageous (Cruz, 2008). The idea of harvesting the ocean wave energy exists for at least two centuries. However, just after the oil crisis of the 1970s, the wave energy mostly started. To date, many Wave Energy Converters (WECs) types have been developed to extract the waves' kinetic and gravitational potential energy. Nevertheless, Karimirad (2014) reminds that just a low quantity of models has reached feasibility and have been installed, and even fewer have produced energy for the grid. As a result, ocean wave energy has attracted the interest of industrial and scientific communities to improve energy extraction and has become a growing research field of energy production. The successful implementation of wave energy depends on the type of technology proposed and site selection. Regarding the location, countries such as Australia, New Zealand, South Africa, Chile and the south of Brazil possesses a significant potential for wave energy with low seasonal variations (Pecher and Kofoed, 2016).

Brazil holds the largest electricity market in South America and the third in America. The current electrical system requires an addition of approximately 6000 MW of capacity every year to supply the growing and prosperous population (Constestabile, Ferrante and Vicinanza, 2015). An alternative to attending the energy demand with environmental awareness is via renewable sources of energy. According to the "*Ministério de Minas e Energia (MME),"* renewable sources will increase in the coming decades, and present a significant role in the Brazilian energy mix (MME, 2017). The transformation in the energy mix will be facilitated due to governmental supports such as "*Programa de Incentivo às Fontes Alternativas de Energia Elétrica*" (PROINFA) and supports from the "*Banco Nacional de Desenvolvimento Econômico e Social* (BNDES)" (Portal Brasil, 2016). Moreover, the government of Santa Catarina has also a clean energy program called "*Programa Catarinense de Energias Limpas*," that supports the project of renewable resources (SC mais Energia, 2017). To date, this program expects to provide more than 1 GW of capacity of renewable energy for the Santa Catarina State.

The primary objective of these renewable energy source programs is to diversify the energy mix, increase the reliability in the electric power supply, and allow the enhancement of regional and local characteristics and potentials (MME, 2017). The south of Brazil possesses considerable potential for wave energy (Pecher, Kofoed, 2016). This new technology shows many advantages compared to other renewable sources, such as its power density, availability, infinite resource. Also, as the population is centralized near the coast, the use of wave energy appears to be a rational solution. Besides the advantages mentioned, according to Parkinson et. al. (2015), large-scale wave energy has been found to provide an exceptional capacity value and cost less to integrate than equivalent amounts of wind energy. Therefore, the ocean wave energy extraction can provide a valid option to attend the market requirements.

Among the available solutions for the harvesting of wave energy, the CETO presents several benefits compared to other WEC systems. The CETO technology is a device classified as a fully submerged point absorber that has been successfully implemented in Perth, Australia by the Carnegie Clean Energy Limited. This technology offers high survivability, reduced environmental impact and a considerable amount of energy extraction for a broad range of conditions (Carnegie Clean Energy Limited, 2017). As a result, the CETO can be a remarkable candidate of WEC device to be used in Brazil.

The development of this work is a collaboration between The University of Adelaide (UoA) and the Federal University of Santa Catarina (UFSC). The Wave Energy Research Group at The University of Adelaide assists the company Carnegie Clean Energy Limited to develop some control technology and optimization on some

CETO prototypes. Several studies have been conducted to optimize the energy absorption and increase the feasibility of fully submerged point absorbers. This work aims to promote the use of wave energy in Brazil, by the design of the fully submerged point absorber technology, to increase energy mix reliability and provides a considerable amount of renewable energy. Moreover, it can contribute to the researches being conducted by the Wave Energy Research Group; consequently, it might support the project industry partner.

This work analyzes the performance of a fully submerged point absorber. The mathematical modeling regards the coupling of the hydrodynamics and vibrations theory. The hydrodynamics properties have their root grounded on the hypotheses of the linear wave theory, which supported the development of WECs (Cruz, 2008). The suggested technology is designed for wave conditions located at a particular site in Santa Catarina. In this regard, the project discusses site selection, presents the physics of point absorbers, and optimizes the operating condition to enlarge the power extraction. The optimization is conducted by sensitivity studies, which analyzes parameters such as Power-take-off coefficients (stiffness and damping), mass, and stroke length. Firstly, regular wave conditions are investigated; then irregular sea conditions. Finally, the optimized device is suggested to implement in the Brazilian energy mix.

2 LITERATURE REVIEW

This section presents the knowledge required for the development of this work. Firstly, several types of Wave Energy Converters and their fundamental characteristics are introduced. Secondly, information about wave resources and site selection are provided. Finally, the mathematical foundation and the main hydrodynamic and vibration theories for energy devices are derived.

2.1 WAVE ENERGY CONVERTERS (WECS)

During more than two centuries, several devices have been proposed for ocean wave energy extraction. Unlike the wind industry where the three-bladed turbine has a predominant design, the wave energy has an extensive variety of WEC technologies. The WECs varies with the wave absorption mechanism, water depth and location (shoreline, near-shore, offshore). According to Falcão (2010), about one hundred projects have been identified at various stages of development. Several approaches have been suggested to classify WECS devices regarding its energy conversion principle, location, and size. This work sorts the WEC systems into three main groups: overtopping devices, oscillating water columns, and oscillating body systems.

2.1.1 Overtopping Energy Devices

Overtopping energy devices convert wave energy power by the overtopping phenomenon to allow the water to fall through the designed outlet (Li and Yu, 2012). In this type of device, the incoming waves go over an ascending ramp to a reservoir above the sea level. These incoming waves can have its magnitude amplified by reflectors designed to enlarge the quantity of overtopping water, which guide with a minimum loss of energy (Karimirad, 2014). The overtopping mechanism changes the kinematic energy of ocean waves into potential energy. The stored water releases back to sea through one or more low-head hydro turbines, which are the Power-Take-off (PTO) system, and produces electric power (Karimirad, 2014). Wave Dragon is an example of overtopping device. Figure 2.1 illustrates an Overtopping Energy Device.

Figure 2.1: Overtopping Energy Devices

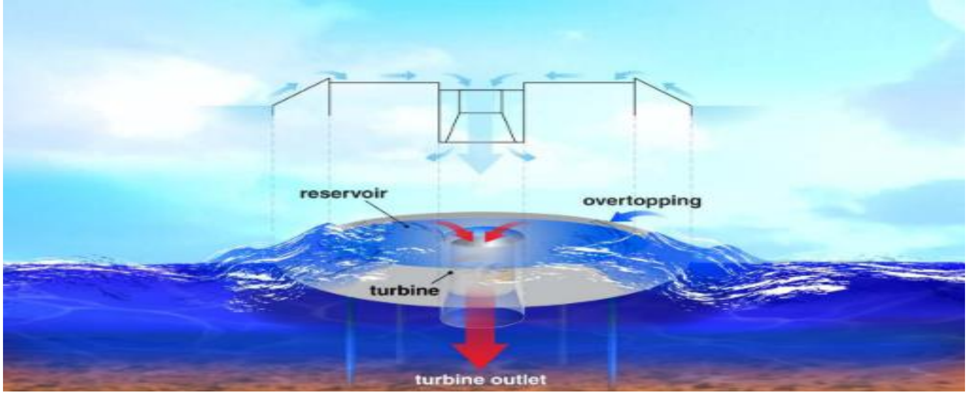

Source: Li and Yu (2012).

2.1.2 Oscillating Water Column

Oscillating Water Column (OWC) devices use a chamber, which works as a cylinder/piston to produce energy. The OWC is partially submerged and has an opening subsurface that receives the incoming waves that move the water up and down inside the chamber, creating fluctuations in the air pressure (Karimirad, 2014). For crest conditions, the air is compressed toward the air turbines. On another hand, for trough conditions, the air is pulled in from the exterior into the chamber. This airflow movement rotates the PTO system that is composed by air turbines producing electricity (Karimirad, 2014). Figure 2.2 illustrates an Oscillating Water Column device.

Figure 2.2: Oscillating Water Column

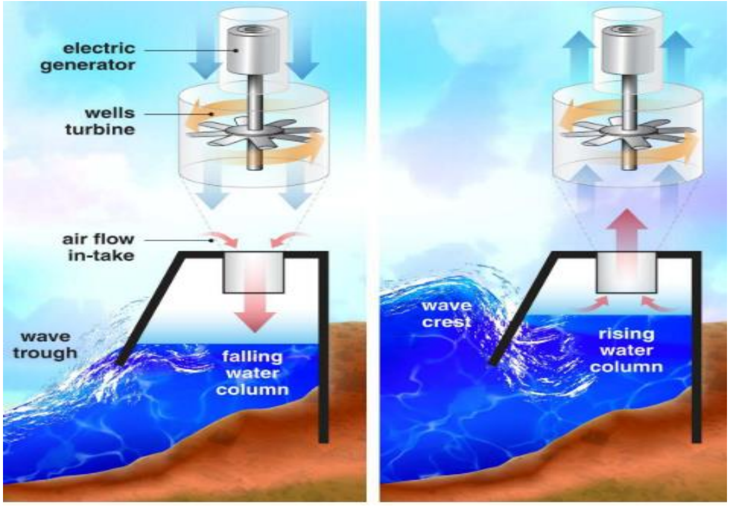

Source: Li and Yu (2012).

2.1.3 Oscillating body systems

Oscillating body systems are wave induced devices that extract energy due to its relative motion. There are several types of oscillating body systems, which are frequently divided into two principal categories: pitching devices (Attenuator, Terminator, and Oscillating wave surge converter) and heaving devices (Point Absorber).

2.1.3.1 Attenuator

Attenuators are multiple-segment floating devices that operate on the water surface parallel to the wave direction and “ride” the waves. On this type of device, the power extraction occurs due to the pitching motion in the joints of each segment, which compresses the hydraulic pump or other PTO systems (Xie and Zuo, 2013). The attenuator length is highly dependent on the wavelength to enlarge power extraction. Pelamis is an example of attenuator device, and it is illustrated in Figure 2.3.

Figure 2.3: Attenuator

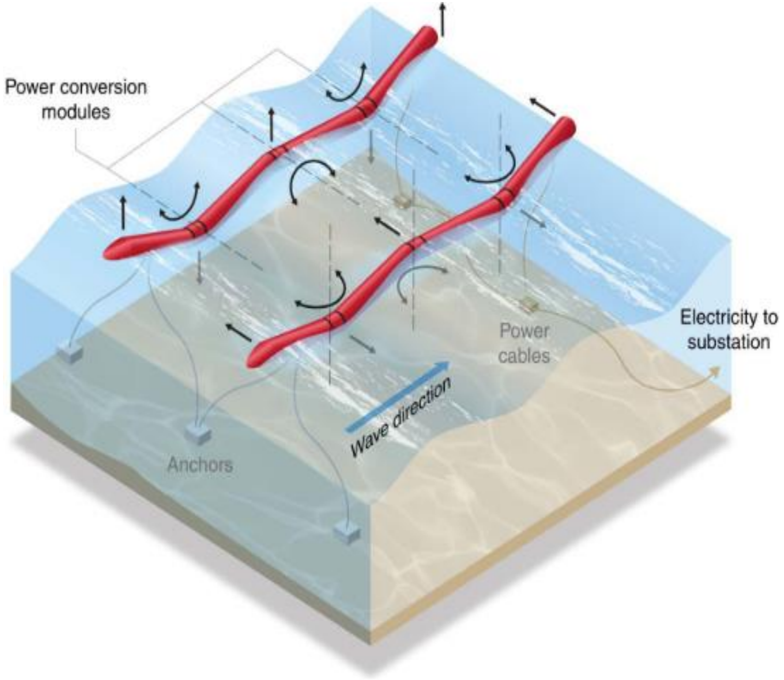

Source: Li and Yu (2012).

2.1.3.2 Terminator

Terminators are floating pitching devices that can be composed of a single or multiple bodies. For terminators, the wave induces a pitch moment against a common cylindrical spine and creates a relative rotational motion of the bodies (Falnes, 2007). This relative motion runs a hydraulic power take-off machinery that extracts wave energy (Falnes, 2007). The power extraction is intensified when the principal axis of the terminator is perpendicular to the wave direction, due to its rotational degree of freedom. An example of terminators is the Salter's Duck, which is illustrated in Figure 2.4.

Figure 2.4: Terminator

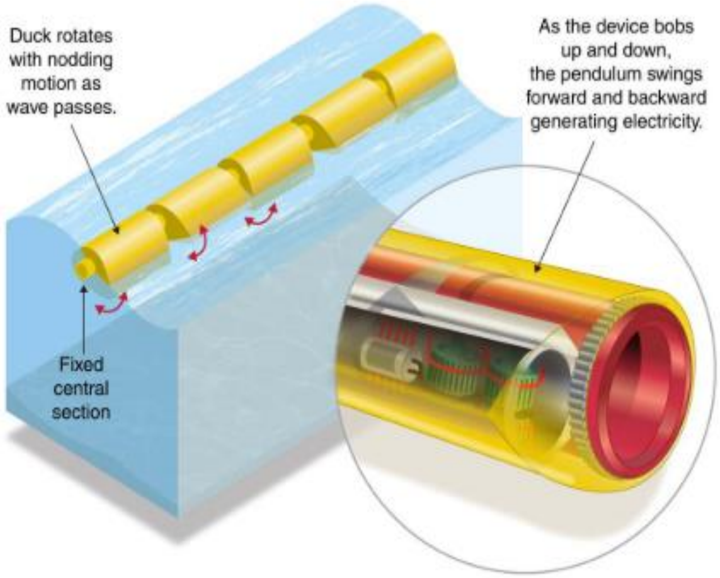

Source: Li and Yu (2012).

2.1.3.3 Oscillating wave surge converter

Oscillating wave surge converters extract wave energy power by the pitching motion of the device. This device is composed by a paddle or a flap, usually higher than the wave free surface, which is connected to a hinge deflector on the seabed. The back and forward motions are generated by the horizontal particle wave velocity and pressure, which is enlarged when the device is positioned perpendicular to the wave direction (Karimirad, 2014). As the device oscillates, it pumps the hydraulic fluid to the PTO system that converts the wave energy into electrical power. The working principle is based on the inverted pendulum concept (Karimirad, 2014). A typical oscillating wave surge converter is the Oyster device. Figure 2.5 illustrates an oscillating wave surge converter.

Figure 2.5: Oscillating wave surge converter

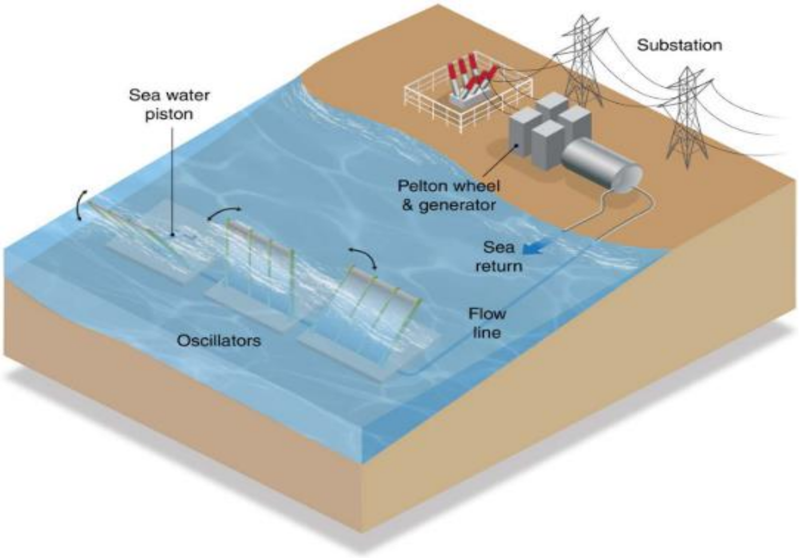

Source: Li and Yu (2012).

2.1.3.4 Point absorbers

Point Absorbers are floating buoys that extract wave energy mainly from heave motion. Typically, the structure can be composed by one or two buoys, fully or partially submerged, that move per wave-induced motions (Li and Yu, 2012). The single buoy device extracts energy by reacting against the foundation at the seabed, and the two buoy device extracts energy from the relative motion between both buoys. The idea of the two buoy system appeared due to the difficulties caused by the distance to connect point absorber to the foundation at the seabed. For both systems, the relative body motion drives the PTO mechanism that is usually composed by a closed hydraulic system or an electric inductor. One example this WEC device is the CETO system developed by Carnegie Clean Energy Limited. Since the focus of this work is on point absorbers, its principles are described in more details in the following sections. Figure 2.6 illustrates an example of Point absorber.

Figure 2.6: Point Absorber

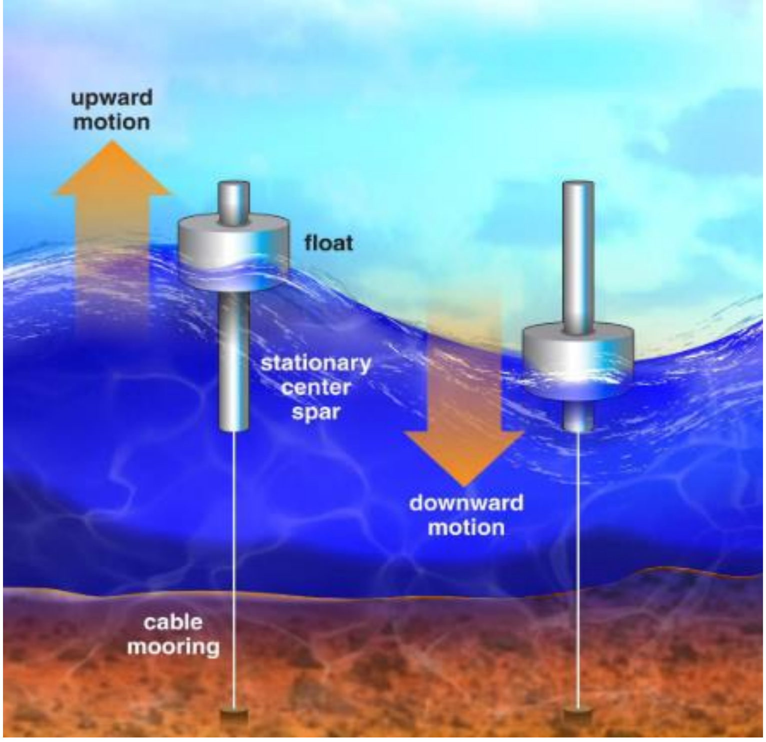

Source: Li and Yu (2012).

The CETO technology consists of a fully submerged point absorber developed by the company Carnegie Clean Energy Limited. According to Karimirad (2014), Point absorbers are one of the principals and earliest concepts of WECs in the wave energy industry. To date, three CETO 5 units are operating at Perth Wave Energy Project Site off Garden Island, Western Australia (Carnegie Clean Energy Limited, 2017).

The CETO 5 is composed of a buoyant actuator, tether, PTO, and foundation. The buoyant actuator moves and drives a hydraulic piston of the PTO via tether coupling, which is attached to the foundation at the seabed. This hydraulic piston produces a high-pressure fluid that generates electricity, or power a reverse osmosis desalination plant to provide fresh water. This project was the first in the world to build a complete grid-connected system. Moreover, it was the only wave project to produce fresh water and electricity, which innovated the wave energy sector (Carnegie Clean Energy Limited, 2017).

The CETO technology presents some benefits compared to other WECs. For instance, CETO is flexible and can operate in a wide range of conditions, such as different water depths, wave directions, and seabed conditions (Carnegie Clean

Energy Limited, 2017). Also, the fully submerged point absorbers have a negligible visual impact and minimal environmental impact of the marine life. Moreover, the buoy is protected from breaking waves and safer from storms, increasing its survivability. Figure 2.7 illustrates the CETO 5 technology.

Figure 2.7: CETO 5

Source: Carnegie Clean Energy Limited (2017).

2.2 OCEAN WAVE ENERGY

An ocean wave is a form of concentrated solar energy. As the sun irradiates the earth's surface, it creates a differential heating that generates thermal air currents. These air currents transfer part of their energy exerting a tangible stress that creates waves and results in a rapidly variable shear, stresses and pressure fluctuations in the water surface. Consequently, the wind flux generates ripples, which rises into swells (Cruz, 2008). The magnitude of the energy depends on the wind velocity, contact distance and time duration of wind blow (Pecher, Kofoed, 2016). This wave energy is accumulated during long distances and travels with a minimum loss of energy, resulting a substantial amount of power. According to Cruz (2008), the global wave energy is estimated to be more than 2 TW. Figure 2.8 illustrates the formation of ocean waves.

Figure 2.8: Ocean wave formation

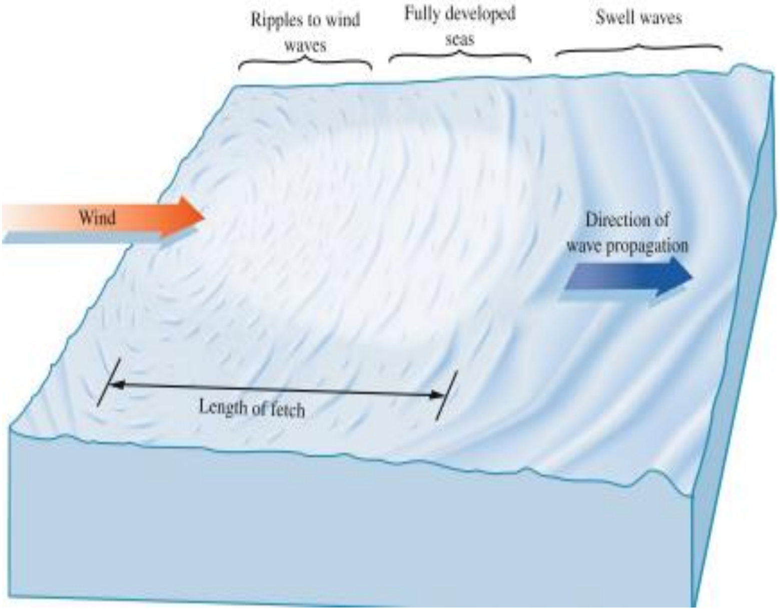

Source: Pecher and Kofoed (2016).

Besides the substantial amount of power, the waves have additional benefits, which contribute to an enormous market potential (Falnes, 2007). As the wave energy is a concentrated source of solar and wind energy, the sea offers the highest energy density of the renewable energy sources, which can be observed in Table 2.1. Moreover, wave energy is more regular in the power extraction available than other renewable sources. According to Pelc and Fujita (2002), WECs devices can extract energy up to 90% of the time, compared to 20-30% for solar and wind energy devices. All these benefits promote the use of ocean wave energy for power generation. However, just a limited number of sites are feasible to implement WEC devices. Therefore, the site location is crucial for a successful implementation.

Table 2.1: Time-averaged power flow

Renewable source	**Time-averaged power flow (spatial concentration)**	**Unit**
Solar energy intensity	0.1-0.3	kW/m²
Wind energy intensity	0.5	kW/m²
Wave energy intensity	3-2	kW/m²

Source: Falnes (2007).

2.2.1 Site

The first procedure in the ocean wave energy is the evaluation of the site resources, which is accomplished during preliminary studies (Cruz, 2008). According to Karimirad (2014), a suitable starting point to determinate favorable sites is to investigate the offshore site dominant frequencies and metocean data. This investigation is made monitoring waves under various sea states over a considerable wide period (Cruz, 2008). Figure 2.9 shows the mean annual wave power over ten years for all global points. As it can be observed, the southern hemisphere has more energy resources. Moreover, the power distribution is more uniform in the southern hemisphere, which is also advantageous (Cruz, 2008). This low variability in the power distribution presents an important feature to implement a WEC device due to the uniform consumption of the population and the need of a stable energy source. Thus, countries such as Chile, Australia, New Zealand, South Africa and the south of Brazil, presents a large potential in ocean wave energy (Pecher, Kofoed, 2016).

Figure 2.9: Global wave energy resource

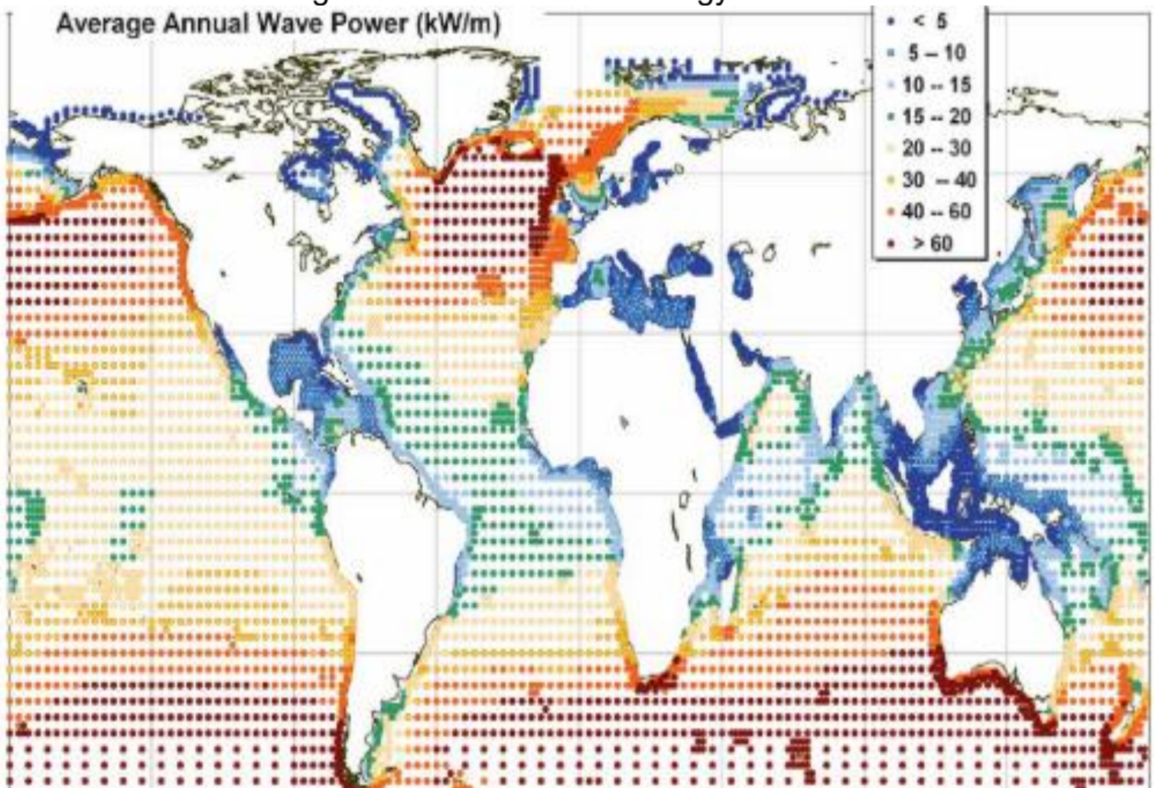

Source: Cruz (2008).

Over the sites mentioned, the state of Santa Catarina, located in the south of Brazil, is a suitable candidate for the implementation of wave energy. Besides the favorable ocean environment in Santa Catarina, Brazil has a large electricity market, which needs to diversify the energy mix. Moreover, the country receives support from the government to develop the electricity market. These characteristics encourage the use of renewable energies in Santa Catarina, which, according to Constestabile, Ferrante and Vicinanza (2015), is one of the most suitable regions for the installations of WEC devices.

The establishment of the site presents a major factor for the design of WEC system. Therefore, a detailed analysis needs to be performed. In "Wave Energy Resources along the coast of Santa Catarina (Brazil)," Constestabile, Ferrante and Vicinanza (2015) presented an assessment of wave energy resources along the Santa Catarina's coastline. The study was accomplished by the analysis of the hindcast data from the European Centre for Medium-Range Weather Forecasts (ECMWF) during January 2004 to December 2014. The authors analyzed eight sites from Praia da Enseada to Cabo de Santa Marta Grande, and studied the nearshore energetic pattern using the coastal propagation model (Mike21 SW). The results were compared to the Wave Buoy Data collected by the Federal University of Santa Catarina in 1996 in Alves and Melo (2001), at São Francisco do Sul. Table 2.2 presents the average power and yearly energy to the respective site, and Figure 2.10 shows the location of the site along the Santa Catarina coastline.

Table 2.2: Wave resources at each site

Sites	**Locality Name**	**Average Power (kW/m)**	**Yearly Energy (MWh/m)**
S1	Praia da Enseada	8.67	75.95
S2	Bupeva	8.83	77.35
S3	Barra Velha	9.92	86.90
S4	Balneário Camboriú	10.13	88.74
S5	Ingleses do Rio Vermelho	12.31	107.84
S6	Campeche	13.25	116.07
S7	Imbituba	13.95	122.20
S8	Cabo de Santa Marta Grande	14.35	125.71

Source: Constestabile, Ferrante and Vicinanza (2015).

Figure 2.10: Sites location in Santa Catarina

Source: Constestabile, Ferrante and Vicinanza (2015).

Subsequently to the site selection, the water depth is critical to the feasibility of WEC devices, due to the cost associated with the installation and maintenance in deep water (Cruz, 2008). For instance, the greater the water depth is, the greater are the costs with foundation, substructure and mooring system (Constestabile, Ferrante and Vicinanza, 2015). On the other hand, there is a possible reduction of the wave energy magnitude for shallow waters. Therefore, there is a range of possible conditions to operate WEC devices. According to Constestabile, Ferrante, and Vicinanza (2015), at 20 m water depth, the waves preserved nearly the same wave characteristics in deep water that in transitional water. For water depths less than 20 m, the WEC farm can experience more Breaking waves and others nearshore related phenomena such as corrosion due to sediment and increased fouling. Moreover, non-technical such as visual and environmental impact, minimum safety distance from the coastline, are also important because it can affect the tourism (Constestabile, Ferrante and Vicinanza, 2015). Figure 2.11 shows the mean wave power flux per unit crest on 20m-isobaths, which present a more comparable characterization of the inshore energetic pattern.

Figure 2.11: Mean wave power flux per unit crest on 20m-isobaths

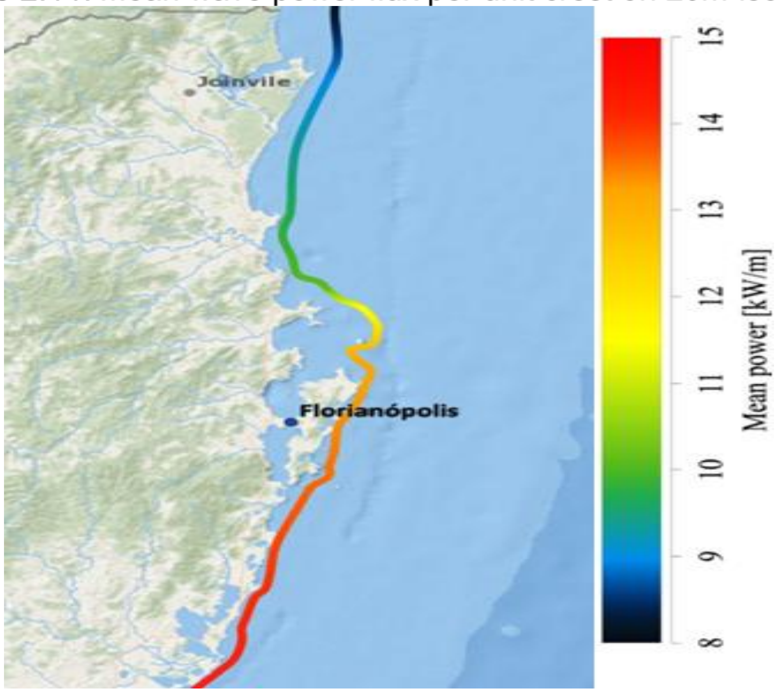

Source: Constestabile, Ferrante and Vicinanza (2015).

The cost reduction associated with construction and maintenance is determinant economic factors for the WEC implementation (Cruz, 2008). Besides the water depth, costs can be minimized selecting sites with small distances from the coastline, urban aggregate, highway, and ports (Constestabile, Ferrante and Vicinanza, 2015). For instance, the implementation of WEC devices in shoreline site is more convenient for the construction, access and maintenance, and grid connection, even with a lower energy (Constestabile, Ferrante and Vicinanza, 2015). Also, the accessibility of port facilities and proximity to grid transmission, and urban aggregate have a positive impact on the implementation of WEC devices (Constestabile, Ferrante and Vicinanza, 2015). Table 2.3 presents the distances of each site from the coastline, urban aggregate, highway, and ports in Santa Catarina. According to the aspects mentioned, Balneário Camboriú and Imbituba are considered suitable locations. The most favorable site is in Imbituba, due to a moderate distance from the electrical grid and the port, and from an energetic point of view, it also possesses higher levels of energy. Therefore, Imbituba’s site is selected in this work.

Table 2.3: Main distances from the ports

Sites	Distance from the Coastline	Distance from Urban Aggregate	Distance from Highway		Distance from Port Facilities (Km)		
	Km	Km	Km	Odonym	São Franc. do Sul	Itajaí	Imbituba
S1	6	7	7	BR-2280	39	89	232
S2	13	12	16	SC-415	59	70	210
S3	14	15	14	SC-415	90	38	187
S4	4	9	10	SC-486	123	16	161
S5	4	5	7	SC-406	180	104	95
S6	6	6	7	SC-405	215	131	67
S7	4	5	5	SC-43	265	82	5
S8	3	3	5	SC-100	295	212	45

Source: Constestabile, Ferrante and Vicinanza (2015).

Fundamentally, the central wave energy flux in Imbituba is provided by wave of significant height $(Hs \text{ or } H_{1/3})$ between 1.5 and 2.5 m, which is the average height between the one third of the waves with higher height, and energy periods between 8 and 11 s. Besides the low seasonal variability, the site presents a very poor occurrence of calm sea (approximately 4%) and few extreme storm conditions (Constestabile, Ferrante and Vicinanza, 2015). Therefore, the WEC device will operate in an appropriated range. The Figure 2.12 shows the scatter diagram in Imbituba, which represents the number of sea state occurrences of the site.

Figure 2.12: Imbituba site wave resources

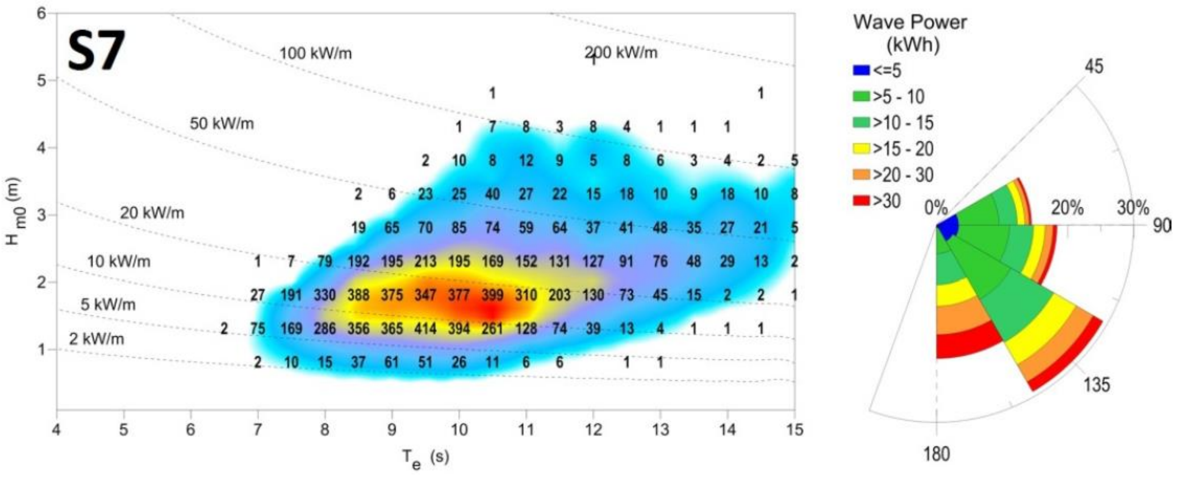

Source: Constestabile, Ferrante and Vicinanza (2015).

2.3 MODELLING THE RESOURCE

The hydrodynamics properties of WEC systems have their mathematical modeling grounded on the hypotheses of the linear wave theory. This approach is based on the assumption of small wave amplitudes compared to the wavelength and water depth; consequently, higher order terms of the equation can be neglected (Journée and Massie, 2001). This central assumption permitted the use of an extensively existed literature of ship hydrodynamics and offshore structures that contributes to the development of wave energy applications in the prediction of the WECs behavior and its viability (Cruz, 2008).

2.3.1 Potential Theory of Gravitational waves

The development of this work initiates with the physics of regular waves, which are characterized by a single frequency, and posteriorly extends to irregular waves. The potential theory uses the linear wave theory, which can describe the behavior of gravitational waves; including surface elevation, wave potential, dispersion relation, and so forth. The method considers a linear relationship of the displacements, velocity, acceleration, and pressure with the surface elevation (Journée and Massie, 2001).

Some simplifications are applied in this theory to describe the waves physically and mathematically. For instance, gravitational waves are treated as incompressible, inviscid and irrotational. The first assumption is made due to the insignificant water compressibility that results in the Continuity Equation (Equation 2.1). The fluid can be regarded as inviscid because the viscosity is mostly critical in a thin boundary layer near the seabed and surface; the effects of viscosity can be neglected in the entire fluid domain (Equation 2.2). Thus, it is also possible to consider the fluid irrotational due to the inviscid flow (Equation 2.3).

$$\nabla \cdot \vec{U} = \frac{\partial u}{\partial x} + \frac{\partial v}{\partial y} + \frac{\partial w}{\partial z} = 0, \qquad \vec{U} = u\hat{\imath} + v\hat{\jmath} + w\hat{k} \tag{2.1}$$

$$\vartheta = 0 \tag{2.2}$$

$$\vec{\omega} = \nabla \wedge \vec{U} = \vec{0}\,, \tag{2.3}$$

where, $\vec{U}$ is the vector that represents the velocity, Λ the cross product, ∇ the differential operator, $\vec{\omega}$ the rotation of the velocity field, ϑ the kinematic viscosity. Regarding the linearity, the theory is validy for waves with a small slope δ, typically lower than 0.05 (Fujarra, 2017):

$$\delta_{max} = \frac{H}{\lambda} \tag{2.4}$$

where, H the wave height, and λ is the wave length. The linear wave theory is grounded on two main equations: Bernoulli's equation and Laplace's equation. Bernoulli's equation is derived from the Euler's equation, which, according to the velocity potential ϕ, for an unsteady flow is given by (Journée and Massie, 2001):

$$\frac{\partial \phi}{\partial t} + \frac{1}{2}\nabla\phi \cdot \nabla\phi + \frac{p}{\rho} + gz = \text{Cte}(t) \tag{2.5}$$

where p is the pressure, ρ the specific mass, g the gravitational acceleration, and z the location at the vertical axis. Laplace's equation is derived by the Continuity equation, which, according to the velocity potential is given by:

$$\nabla^2\phi = 0 \tag{2.6}$$

where:

$$\nabla\phi = \vec{U} \tag{2.7}$$

It is important to notice that the Laplace's equation is linear and homogeneous. Therefore, it allows solutions based on the superposition of elementary results, such as waves superposition and potential fields. The principle of superposition of regular waves is vital to describe the aleatory behavior of oceans (irregular waves). Based on the superposition principle and statistical aspects, the sea, which is not deterministic, can be modeled. The superposition of potential fields allows theoretical descriptions of loads and moments caused by waves on floating structures.

The velocity potential function requires satisfying the Laplace and Bernoulli equation to characterize gravitational waves. The coefficients are defined based on the boundary conditions of the gravitational waves. The wave is treated as two-dimensional to facilitate the mathematical modeling, where the surface elevation $\varsigma(x,t)$ describes the horizontal position x and the instant of time t. To determine the potential velocity, the method of Separation of variables is applied:

$$\phi(x, y, t) = \chi(x)\, \mathfrak{z}(z)\, \tau(t) \tag{2.8}$$

where, χ is a function that depends on the position x, $\mathfrak{z}$ a function that depends on the depth z, and τ a function that depends of the time t. The right side of Figure 2.13 represents the two-dimensional wave observed at a fixed point over the time, and the left side, represents the two-dimensional wave observed in a fixed time over the length.

Figure 2.13: Harmonic wave definitions

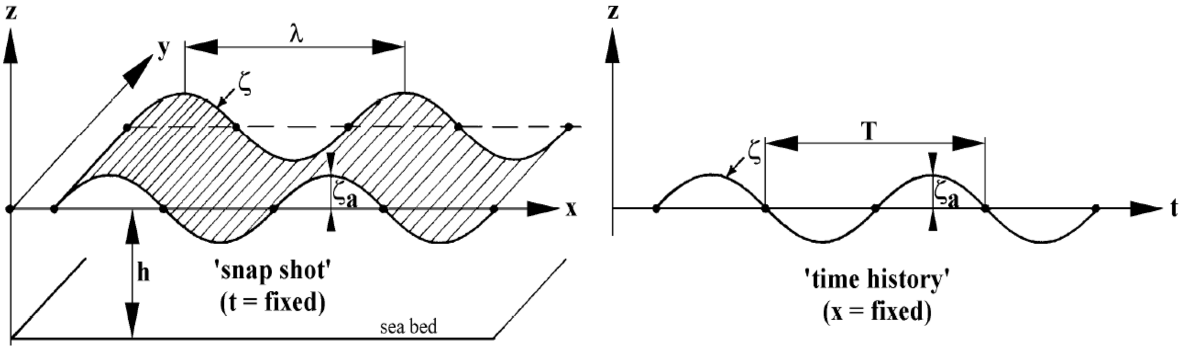

Source: Journee and Massie (2001).

Where ς_a is the wave amplitude, T the wave period, and h the water depth. It can be observed by the behavior of gravitational waves, that the potential function is periodic on time. Therefore, the function τ can be described as:

$$\tau(t) = \sin(\omega t) \tag{2.9}$$

Another important aspect that can be noticed is the wave periodicity. The wave angular frequency can be defined as:

$$\sin(\omega t) = \sin[\omega(t + T)] \tag{2.10}$$

$$\omega T = 2\pi \tag{2.11}$$

$$\omega = \frac{2\pi}{T}, \tag{2.12}$$

where, ω is the wave frequency. Substituting the result of the Equation 2.9 in the Laplace equation (Equation 2.6), dividing by the potential function, and manipulating the resulting equation, the following equation is resulted (Fujarra, 2017):

$$\frac{1}{\chi}\frac{d^2\chi(\mathrm{x})}{dt^2}+\frac{1}{\text{ʒ}}\frac{d^2\text{ʒ}(\mathrm{z})}{dt^2}=0 \qquad (2.13)$$

This equation can be divided into two parts:

$$\frac{1}{\text{ʒ}}\frac{d^2\text{ʒ}(\mathrm{z})}{dt^2}=+k^2 \qquad (2.14)$$

$$\frac{1}{\chi}\frac{d^2\chi(x)}{dt^2}=-k^2 \qquad (2.15)$$

Both differential equations are solved separately. The physic observation of gravitational waves allows the mathematical modeling of the differential equations. The function $\chi(\mathrm{x})$ is a harmonic progression in the direction x. On another hand, the function $\text{ʒ}(\mathrm{z})$ decays with the depth. Therefore, the solution of the potential equation can be given by:

$$\phi(x,y,t)=[C_1\,cos(kx)+C_2\,sin(kx)]\;[D_1e^{kz}+D_2e^{-kz}]\sin(\omega t) \qquad (2.16)$$

According to the geometric cyclicity observed on the gravitational waves, the wave number k can be defined:

$$C_1\,cos(k\,x)+C_2\,sin(kx)=C_1\,cos(kx+k\lambda)+C_2\,sin(kx+k\lambda) \qquad (2.17)$$

$$k\lambda=2\pi \qquad (2.18)$$

$$k=\frac{2\pi}{\lambda} \qquad (2.19)$$

The coefficients in Equation 2.17 are determined based on the boundary conditions illustrated in Figure 2.14.

Figure 2.14: Wave boundary conditions

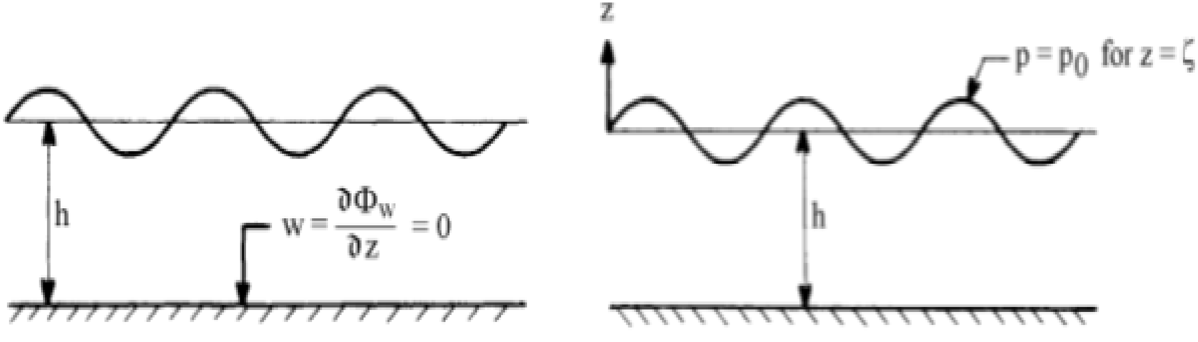

Source: Journee and Massie (2001).

At the seabed, the boundary condition states the impermeability of the wave effects:

$$\frac{d\phi(\mathrm{x}, -\mathrm{h}, \mathrm{t})}{dz} = 0 \tag{2.20}$$

An additional boundary condition is the dynamic free surface. For $z = 0$, it is necessary the compatibility between the surface elevation and the instantaneous vertical coordinate:

$$z = \varsigma(x, t) \tag{2.21}$$

$$p(z = 0) = p_{atm} \tag{2.22}$$

where, p_{atm} is the atmospheric pressure. Applying the result to the Bernoulli (Equation 2.5) and assuming waves with small wave amplitude compared to the length, the squared velocity can be neglected compared to the term $\frac{d\phi}{dt}$, therefore:

$$\varsigma(x, t) = -\frac{1}{g}\frac{d\phi}{dt} \tag{2.23}$$

Based on the physical observation, the surface elevation function can be described as:

$$\varsigma(x, t) = \varsigma_a \, cos(kx - \omega t) \tag{2.24}$$

Applying the boundary conditions of Equation 2.20 and Equation 2.22, the wave potential can be described as:

$$\phi(\mathrm{x}, \mathrm{z}, \mathrm{t}) = \frac{g\ \varsigma_a}{\omega}\frac{\cosh[k(h + z)]}{\cosh(kh)} \sin(kx - \omega t) \tag{2.25}$$

2.3.2 Dispersion equation and wave velocity

The dispersion equation is a transcendental equation that relates the cyclicity of time with the geometrical cyclicity of the gravitational wave. The equation results in a unique solution expressed as:

$$\omega^2 = gk[\tanh(kg)] \tag{2.26}$$

$$\frac{\omega^2 h}{\mathrm{g}}\frac{1}{(kh)} = \tanh(kh) \tag{2.27}$$

The solution of the dispersion equation gives the wave number for each frequency, which can be manipulated to result in wave velocity c:

$$c = \frac{\lambda}{T} = \frac{\omega}{k} = \sqrt{\frac{g}{k}\tanh(kh)} \tag{2.28}$$

2.3.3 Kinematics of the particle

Based on the surface elevation of the particle associated with the potential equation and the dispersion equation; it is possible to describe the velocity of any point of a progressive wave. The horizontal velocity is given by:

$$u = \frac{d\phi}{dx} = \frac{g\,k\,\varsigma_a}{\omega}\frac{\cosh[k(h+z)]}{\cosh(kh)}\cos(kx - \omega t) \tag{2.29}$$

$$u = \frac{d\phi}{dx} = \varsigma_a \omega \frac{\cosh[k(h+z)]}{\sinh(kh)}\cos(kx - \omega t) \tag{2.30}$$

Analog to the horizontal velocity, the vertical velocity is given by:

$$w = \frac{d\phi}{dz} = \varsigma_a \omega \frac{\sinh[k(h+z)]}{\sinh(kh)}\sin(kx - \omega t) \tag{2.31}$$

The equations show that the extreme values of horizontal velocity are achieved when $\cos(kx - \omega t) = 1$, which represents the crests and troughs. On the other hand, the extreme values for vertical velocity occurs for $\sin(kx - \omega t) = 1$, which happens when the surface elevation cross the undisturbed free surface. The term related to the particle depth and water depth shows an exponential decay of the velocities when the particle depth is increased. The minimum velocity occurs at the seabed, and the maximum velocity at the free surface. These observations can be verified in Figure 2.15, which illustrates the velocity field in shallow water on the left side, and deep water on the right side.

Figure 2.15: Wave velocity field in Shallow water and Deep-water

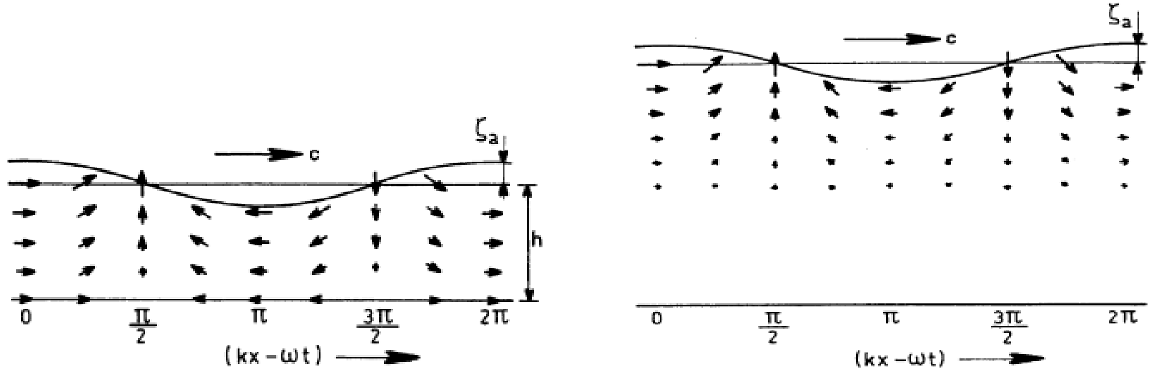

Source: Journee and Massie (2001).

Due to the small steepness of the wave, the coordinates x and z on the right hand of the Equation 2.30 and Equation 2.31 can be substituted by the mean position x_1 and z_1. Hence, the water motion position shifts can be neglected. Therefore, integrating the velocity by time, the particle displacement around a position x_1 and a depth z_1 can be written as:

$$\Gamma(x_1, z_1, t) = \int u(x_1 + \eta, z_1 + \xi, t)\, dt = -\varsigma_a \frac{\cosh[k(h + z_1)]}{\sinh(kh)} \sin(kx_1 - \omega t) \qquad (2.32)$$

$$\Omega(x_1, z_1, t) = \int w(x_1 + \eta, z_1 + \xi, t)\, dt = +\varsigma_a \frac{\sinh[k(h + z_1)]}{\sinh(kh)} \cos(kx_1 - \omega t) \qquad (2.33)$$

where, Γ is the water displacement in the horizontal axis, and Ω the water displacement in the vertical axis. Figure 2.16 illustrates the displacements in shallow water on the left, and deep water on the right.

Figure 2.16: Wave displacement in Shallow water and Deep-water

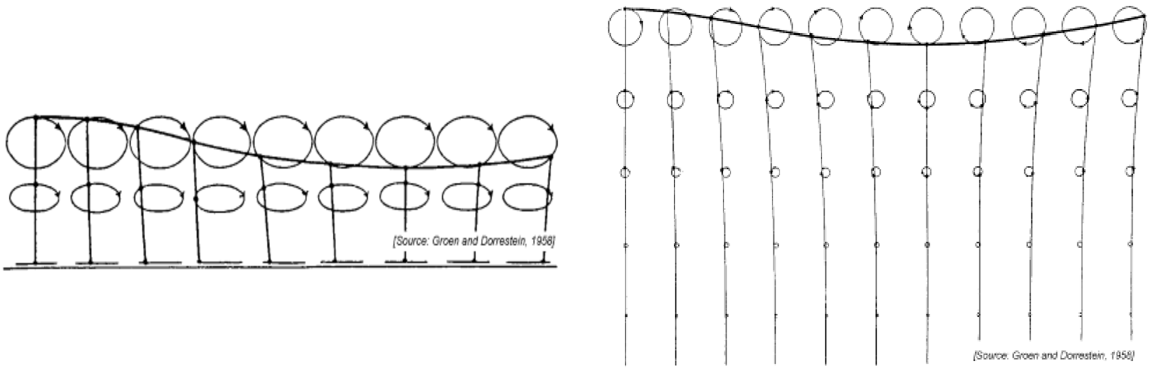

Source: Journee and Massie (2001).

2.3.4 Pressure field of the gravitational wave

The wave pressure is obtained integrating the Euler’s equation over the vertical direction:

$$\frac{Dw}{Dt} = -\frac{1}{\rho}\frac{\partial p}{\partial z} - g \tag{2.34}$$

where:

$$\frac{Dw}{Dt} = \frac{\partial w}{\partial t} + u\frac{\partial u}{\partial x} + v\frac{\partial v}{\partial y} + w\frac{\partial w}{\partial z} \tag{2.35}$$

It is important to notice that the order of magnitude of the first component is greater than the other elements:

$$\frac{\partial w}{\partial t} \gg u\frac{\partial u}{\partial x} + v\frac{\partial v}{\partial y} + w\frac{\partial w}{\partial z} \tag{2.36}$$

Therefore, the Equation 2.34 can be simplified to:

$$-\varsigma_a\omega^2\frac{\sinh[k(h+z)]}{\sinh(kh)}\cos(kx-\omega t) = -\frac{1}{\rho}\frac{\partial p}{\partial z} - g \tag{2.37}$$

Which can be rewritten as:

$$p = -\rho g z + \rho\varsigma_a g\frac{\cosh[k(h+z)]}{\cosh(kh)}\cos(kx-\omega t) \tag{2.38}$$

The first term of the Equation 2.38 refers to the hydrostatic pressure and the second term to the hydrodynamic pressure. Figure 2.17 shows the hydrodynamic pressure distribution for a regular wave.

Figure 2.17: Non-dimensional hydrodynamic pressures

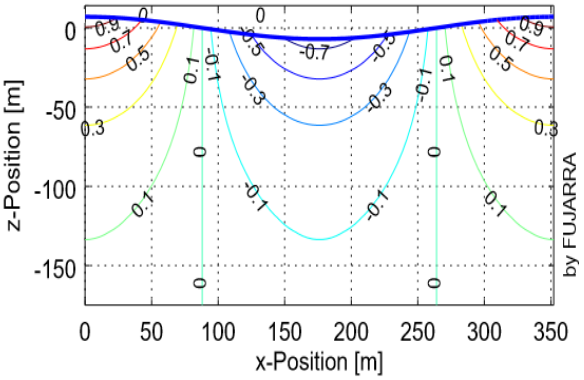

Source: Fujarra (2017).

The magnitude of the hydrodynamic pressure is maximum at the free surface and minimum at the seabed. Also, the hydrodynamic pressure is maximum at the crest, minimum at the troughs, and null when the surface elevation crosses the undisturbed free surface.

2.3.5 Propagation of gravitational wave energy

The mathematical description of the wave energy is important to analyze the gravitational wave behavior towards the coast; the power necessary of the paddle to generate waves (small-scale experiments, such as Chapman Lab at The University of Adelaide); and the power available for energy harvesting. The wave energy is usually referred as the energy per unit of horizontal area.

The total wave energy is composed of potential and kinetic energy. Where the first energy refers to the surface elevation, and the second energy refers to the movement of the fluid particles. The potential energy of a gravitational wave occurs due to the displacement of the water surface, which can be derived integrating the water column over the wavelength.

$$(E_p)_T = \frac{1}{\lambda}\int g\bar{z}dm \tag{2.39}$$

Figure 2.18: Wave energy

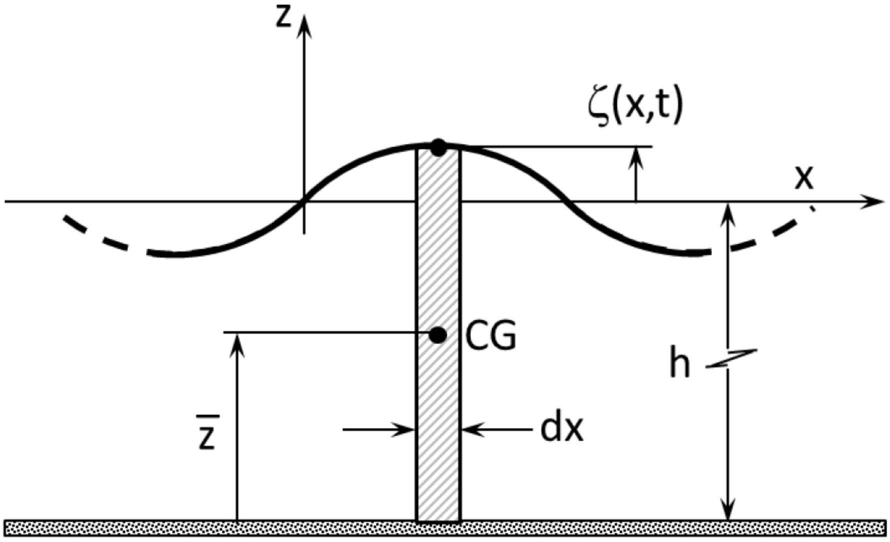

Source: Fujarra (2017).

Where, $\bar{z}$ is the geometric center at the z axis of the differential element of mass dm.

$$\bar{z} = \frac{(h + \varsigma)}{2}\ , \qquad dm = \rho(h + \varsigma)dx \tag{2.40}$$

Therefore, the Equation 2.39 can be written as:

$$(E_p)_T = \frac{1}{\lambda}\int_{x}^{x+\lambda} \frac{\rho g(h + \varsigma)^2}{2} dx \tag{2.41}$$

$$(E_p)_T = \frac{\rho g h^2}{2} + \frac{\rho g {\varsigma_a}^2}{4} \tag{2.42}$$

The first term is related to the potential energy without a wave, and the second is related to the potential energy due to the gravitational wave. Therefore, the potential energy of a regular wave can be written as:

$$(E_p)_{wave} = \frac{\rho g {\varsigma_a}^2}{4} \tag{2.43}$$

It can be observed that the energy depends only on the wave amplitude squared. For an irregular wave, the potential energy can be obtained through the superposition of regular waves as:

$$(E_p)_{wave} = \frac{\rho g}{4}\sum_{n=1}^{N} {\varsigma_{a_n}}^2 \tag{2.44}$$

The total kinetic energy per unit of area is calculated via integration of the particle's kinetic energy over the water depth and wavelength.

$$(E_c)_{wave} = \frac{1}{\lambda}\int_{x}^{x+\lambda}\int_{-h}^{\varsigma} \rho \frac{u^2 + w^2}{2} dz dx \tag{2.45}$$

Solving the Equation 2.45, it results in:

$$(E_c)_{wave} = \frac{\rho g {\varsigma_a}^2}{4} \tag{2.46}$$

Therefore, the total wave energy per unit of area of the free surface is given by:

$$E_{wave} = (E_c + E_p)_{wave} = \frac{\rho g {\varsigma_a}^2}{2} \tag{2.47}$$

2.3.6 Wave energy transport or Wave power per unit crest

The Wave power refers to the average work done over one period. It represents the amount of work delivered against the fluid pressure that passes through a plane vertical plane of a unit width and height dz. Figure 2.19 illustrates the wave power. The wave work W realized by the wave is equal to the fluid force multiplied by the distance:

$$dW = \{1\,p\,dz\}\,\{udt\} \tag{2.48}$$

Figure 2.19: Wave power per unit crest

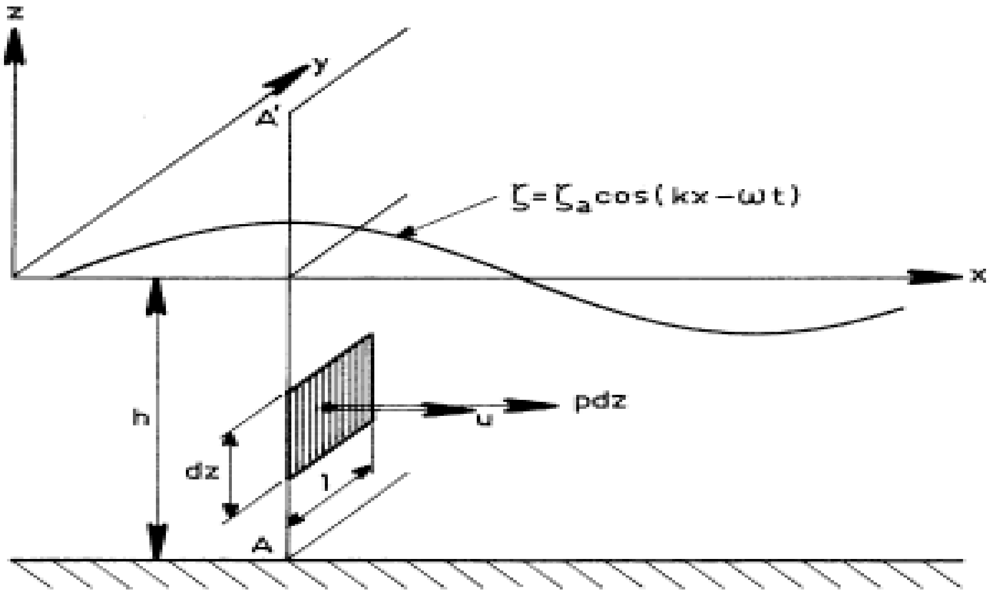

Source: Journee and Massie (2001).

The wave energy is transported at the wave group velocity c_g that is perpendicular to the wave propagation plane (Journee and Massie, 2001). Substituting the variables p and u by its respective functions (Equation 2.38 and Equation 2.30), and manipulating, the wave power can be written as:

$$\overline{W} = E\,c_g \tag{2.49}$$

where c_g is the wave group velocity (Journee and Massie, 2001):

$$c_g = \frac{c}{2}\left(1 + \frac{2\mathrm{kh}}{\sinh(2kh)}\right) \tag{2.50}$$

2.3.7 Irregular waves

The irregular waves can be modeled according to the linear wave theory. A common approach to representing irregular waves is to use a summation of waves with amplitude according to its respective frequency and apply a random phase for each component. In the Cartesian coordinates, the surface elevation can be described by a linear sum of an infinite number of frequency components (Cruz, 2008):

$$\varsigma(x, y, t) = \sum_{n=o}^{\infty} \varsigma_{a_n} \cos(k_n \mathrm{x} \cos \beta_n + k_n \mathrm{y} \sin \beta_n - \omega_n t - \psi_n) \qquad (2.51)$$

where, for each wave component n, ς_{a_n} represents the respective wave amplitude, k_n the wave number component, ω_n the circular wave frequency component, and ψ_n the random phase angle component. Figure 2.20 illustrates an irregular wave representation.

Figure 2.20: Irregular wave composition

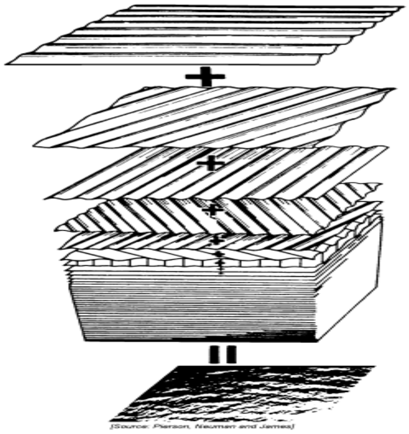

Source: Journee and Massie (2001).

The directionality in the wave field (β_n) is the angle between the wave propagation and the x-axis, which is irrelevant in this analysis due to the axisymmetric about a vertical axis of the point absorbers. Therefore, for a unidirectional wave, the surface elevation can be described as:

$$\varsigma(x, t) = \sum_{n=1}^{N} \varsigma_{a_n} \cos(k_n x - \omega_n t + \psi_n) \qquad (2.52)$$

The surface elevation for a fixed position is illustrated in Figure 2.21.

Figure 2.21: Surface elevation (time domain)

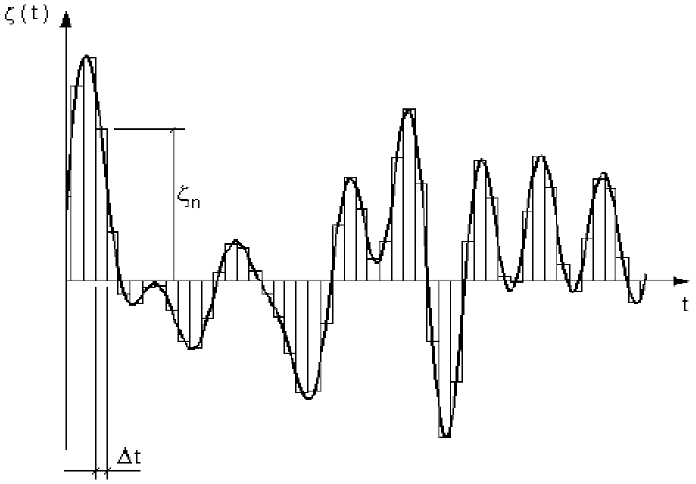

Source: Fujarra (2017).

According to Journée and Massie (2001), the use of Fourier series analysis is reasonable to study the frequency characteristics of an irregular signal such as the ocean waves. The main information is the statistical properties in terms of representation of the wave's amplitude distribution over the frequencies, which represents the wave spectrum. Figure 2.22 illustrates the Frequency domain representation.

Figure 2.22: Frequency domain representation

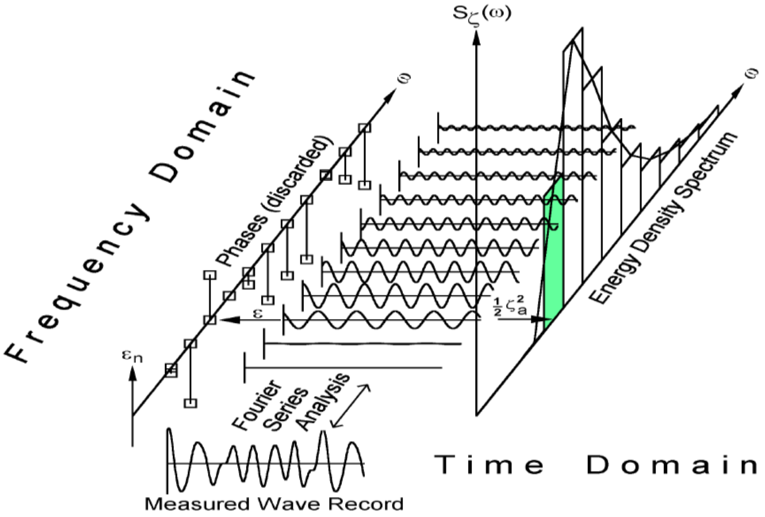

Source: Journée and Massie (2001).

2.3.8 Wave Spectrum

The wave spectrum is an analytical representation of the power spectral density, which is obtained by measurements of the wave surface elevation over long periods of time, and characterized by a stochastic process (Fujarra, 2009). This representation is important to design offshore structures due to the limited number of sea parameters necessary to model the spectrum, such as wave period, significant wave height, zero-up-crossing period, shape factors, and so forth (Chakrabarti, 1987). There are several formulations to describe the wave spectra, such as ITTC, JONSWAP, Bretschneider, and Pierson-Moskowitz.

This work presents the ITTC and JONSWAP spectrums. The first spectrum is used during the studies at The University of Adelaide; and the second is widely employed in studies referring to the Bacia de Campos (Fujarra, 2009). Therefore, due to the location used in this work is near to the Bacia de Campos, JONSWAP is used for the wave analysis. The wave spectrum $S_{\varsigma}(\omega)$ represents the energy distribution present in each regular component, which provides the results in Power Spectral Density (PSD):

$$S_{\varsigma}(\omega) = \frac{[\varsigma_a(\omega)]^2}{2\Delta\omega} \tag{2.53}$$

Hence, the spectrum can be converted in amplitude by:

$$\varsigma_{a_n} = \sqrt{2\ S_{\varsigma}(\omega)\ d\omega} \tag{2.54}$$

As the surface elevation, several wave's properties can be treated as a summation of regular components, such as the pressure, velocity and wave energy.

2.3.8.1 ITTC Spectrum

During the International Towing Tank Conference (ITTC), some modifications to the Pierson-Moskowitz spectrum model was proposed. Pierson-Moskowitz (P-M) spectrum is broad and very used spectrum, which can be described by:

$$S_{\varsigma}(\omega) = \left(\frac{\mathcal{A}}{\omega^5}\right) e^{-\mathcal{B}/\omega^4} \tag{2.55}$$

The constants $\mathcal{A}$ and $\mathcal{B}$ depends on the spectrum selected, for some spectrum the formulation is defined using two parameters, significant wave height (H_s) and wave peak period (T_p):

$$T_z = 0.71\, T_p \tag{2.56}$$

$$\mathcal{A} = \frac{4\, H_s\, \pi^3}{{T_z}^4} \tag{2.57}$$

$$\mathcal{B} = \frac{16\, \pi^3}{{T_z}^4}, \tag{2.58}$$

where, T_z is the mean zero-crossing wave period. These coefficients are recommended by the International Towing Tank Conference (ITTC), and the spectrum above is named as ITTC spectrum (Pawlowski, 2009).

2.3.8.2 JONSWAP Spectrum

JONSWAP spectrum was originated during an extensive program called Joint North Sea Wave Project (JONSWAP), which describes developing sea. In 1979, Goda derived an approximated solution based on the significant wave height and peak period (Fujarra, 2009):

$$S_\varsigma(\omega) = \alpha^* {H_s}^2 \frac{\omega^{-5}}{{\omega_p}^{-4}}\ \exp\left\{-1.25\left(\frac{\omega}{\omega_p}\right)^{-4}\right\} \gamma^{\exp\left\{-\frac{(\omega-\omega_p)^2}{2\tau^2 {\omega_p}^2}\right\}} \tag{2.59}$$

where:

$$\begin{aligned} \tau = \tau_a = 0.07; \qquad & for \qquad \omega \le \omega_p \\ \tau = \tau_b = 0.09; \qquad & for \qquad \omega > \omega_p \end{aligned} \tag{2.60}$$

$$\gamma = 3.3 \tag{2.61}$$

$$\alpha^* = \frac{-0.0624}{0.23 + 0.0336\gamma - 1.185(1.9+\gamma)^{-1}} \tag{2.62}$$

where γ is the peak enhancement factor.

Figure 2.23 compares ITTC spectrum and JONSWAP spectrum with $\gamma = 3.3$, and $\gamma = 1$ to illustrate the influence of the peak enhancement factor, which is used during this study. It can be observed that if the peak enhancement factor is set to a unit, the ITTC is comparable to a JONSWAP spectrum.

Figure 2.23: Peak enhancement factor comparison

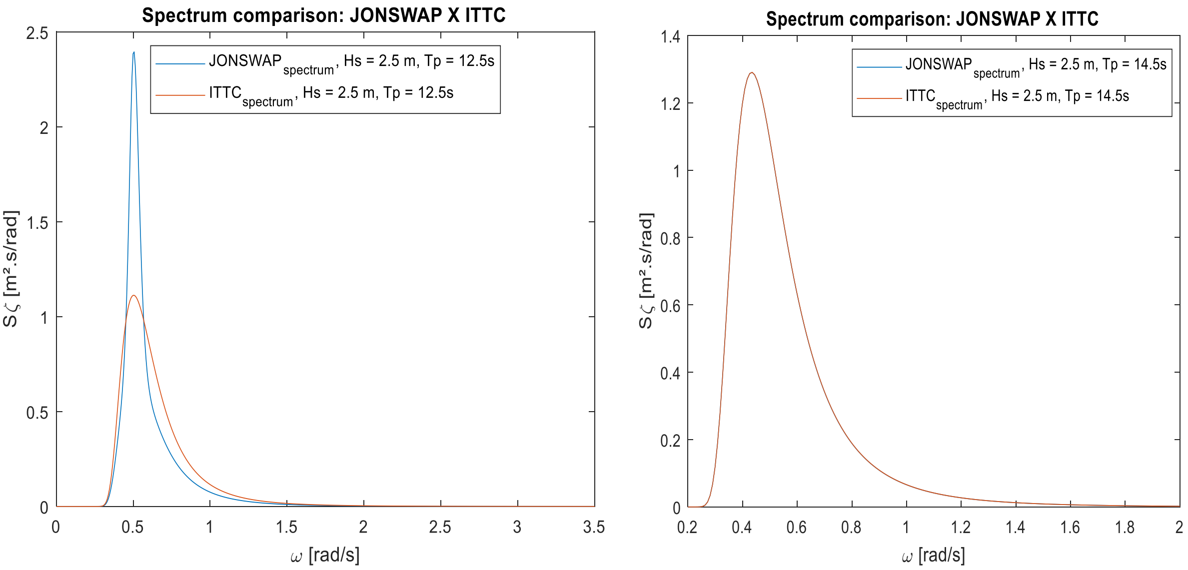

$(\gamma = 3.3)$ $(\gamma = 1)$

Source: Author (2017).

2.3.8.3 Wave Energy and Wave Power for a spectrum

The calculation of the ocean wave energy for irregular condition is made via integration of the power spectral density (S_ς) (Journée and Massie, 2001):

$$E_{wave} = \frac{\rho g}{2} \int_{-\infty}^{\infty} S_\varsigma(\omega)\, d\omega \tag{2.63}$$

The wave power of the swell is expressed as:

$$\bar{W} = p\ g \int_{-\infty}^{\infty} S_\varsigma(\omega)\, c_g(\omega)\, d\omega \tag{2.64}$$

For an infinite water depth, the equation can be simplified to (Multon, 2012):

$$\bar{W}_{approx} = \frac{p\ g^2}{64\pi} H_s T_e \tag{2.65}$$

where, T_e is the energy wave period.

2.3.9 Probability density distribution and probability function

The probability density function represents the number of occurrences in each interval, divided by the total number of occurrences. For ocean waves the equation can be approximated to a Gaussian distribution as:

$$f(\varsigma) = \frac{1}{\sigma_\varsigma \sqrt{2\pi}} e^{\left(\frac{-\varsigma^2}{2(\sigma_\varsigma)^2}\right)} \tag{2.66}$$

where, σ_ς is the standard deviation of the sea elevation. Figure 2.24 illustrates the probability density function of an irregular wave.

Figure 2.24: Probability density function of an irregular wave

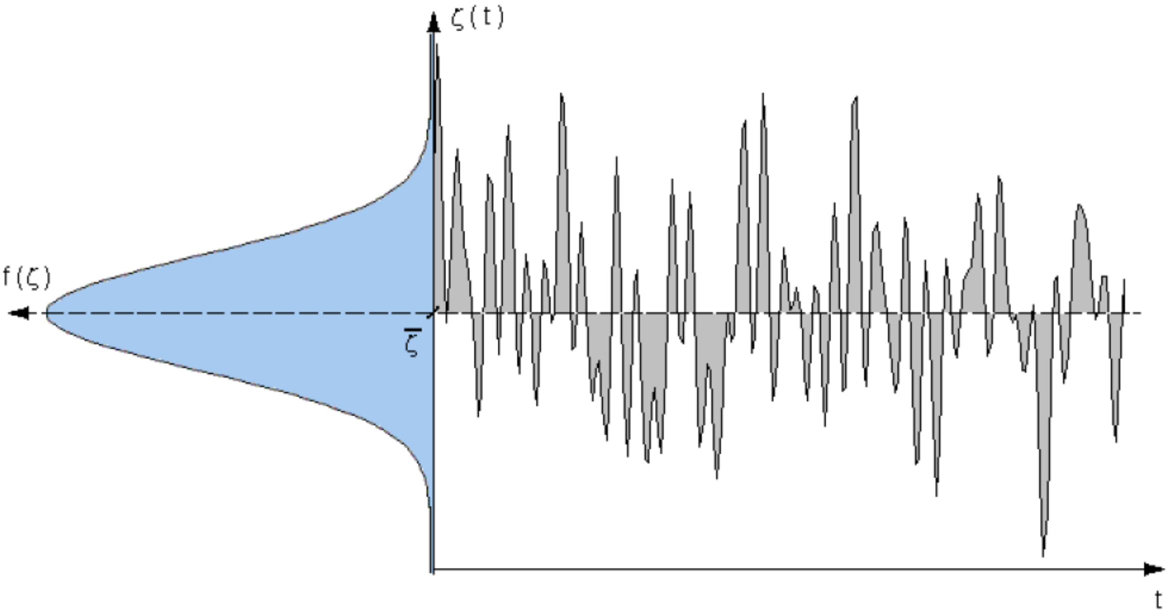

Source: Fujarra (2017).

Based on this function, it is possible to estimate the probability function of the surface elevation integrating the density probability function over the specified range, which is usually described as a multiple of the standard deviation.

$$Prob\{-\lambda\sigma_\varsigma \leq \varsigma(t) \leq \lambda\sigma_\varsigma\} = \frac{1}{\sigma_\varsigma \sqrt{2\pi}} \int_{-\lambda\sigma_\varsigma}^{\lambda\sigma_\varsigma} e^{\left(\frac{-\varsigma^2}{2(\sigma_\varsigma)^2}\right)} d\varsigma \tag{2.67}$$

2.3.10 Time domain and frequency domain correlation

The mean elevation of the ocean represents the centroid of the area under the curve $f(\varsigma)$.

$$\bar{\varsigma} = \int_{-\infty}^{\infty} \varsigma\, f(\varsigma)\, d\varsigma \qquad (2.68)$$

The mean square value of elevations is given by:

$$\overline{\varsigma^2} = \int_{-\infty}^{\infty} \varsigma^2\, f(\varsigma)\, d\varsigma \qquad (2.69)$$

Which can be related to the moment of inertia of the area under the curve $f(\varsigma)$. The standard deviation of sea elevations is equal to:

$$\sigma_{\varsigma}{}^2 = \int_{-\infty}^{\infty} (\varsigma - \bar{\varsigma})^2\, f(\varsigma)\, d\varsigma \qquad (2.70)$$

Manipulating the Equation 2.70, and assuming the mean value as zero, it is possible to define the standard deviation as:

$$\sigma_{\varsigma} = \sqrt{\overline{\varsigma^2}} \qquad (2.71)$$

According to the Parseval theorem, which is a result of the sea spectrum energy, the following relationship is derived:

$$\int_{-\infty}^{\infty} [\varsigma(t)]^2\, dt = \frac{1}{\pi} \int_{-\infty}^{\infty} [\varsigma_a(\omega)]^2\, dw \qquad (2.72)$$

As the ocean is assumed to have a mean displacement of $\bar{\varsigma} = 0$, and assuming the standard deviation of the elevations of a register of time τ, it is possible to write:

$$\sigma_{\varsigma}{}^2 = \overline{[\varsigma(t)]^2} = \frac{1}{\tau} \int_{0}^{\tau} [\varsigma(t)]^2\, dt \qquad (2.73)$$

As a result, it is possible to correlate the frequency domain and time domain as:

$$\sigma_{\varsigma}{}^2 = \int_{0}^{\infty} S_{\varsigma}(\omega)\, d\omega \qquad (2.74)$$

2.4 MODELING OF POINT ABSORBERS

The modeling of WECs devices is fully described using three translational modes of motions (surge, sway and heave) and three rotational modes of motion (roll, pitch, and yaw). Figure 2.25 illustrates the modes of motion of a Point Absorber. However, a common approach for initial studies is the modeling using three degrees of freedon for the plane motion, or focused on a specific motion, such as heave or surge (Cruz, 2008).

Figure 2.25: Point Absorber modes of motion

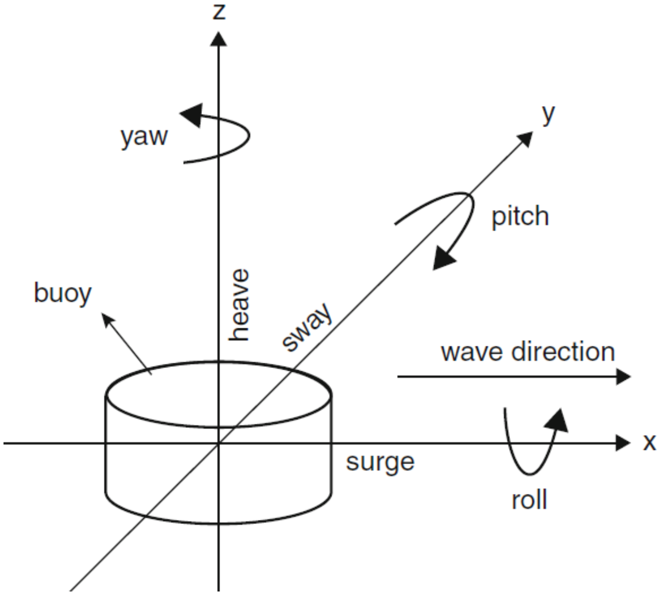

Source: Pecher and Kofoed (2016).

Point absorber oscillates according to the stochastic behavior of Ocean waves, which can be represented by a composition of waves with different frequencies and directions. For this reason, it is common to model WECs in the frequency domain using linear superposition. The model of a WEC device in a single translational mode for a long-crested incident wave was firstly presented by Jefferys (1980):

$$\mathrm{m}_{buoy}\,\ddot{Z}(t) = F_f(t) + F_{ext}(Z, \dot{Z}, t) \tag{2.75}$$

Where F_f represents the Wave/fluid induced forces, F_{ext} is the External forces attached to the body, m_{buoy} is the mass of the buoy, and Z is the vertical displacement of the buoy about its equilibrium position.

2.4.1 External Forces

The mathematical representation of external forces is crucial to the accuracy of the body motion equation. External forces include forces caused by components attached to the buoy. Therefore, its characteristics vary with the type of mechanism. For a point absorber, the external forces are generally related to the mooring and PTO forces ($F_{mooring}$ and F_{PTO}, respectively). When the buoy moves up, the PTO system extracts energy from the motion and part of the energy is stored by the mooring system, which is converted into energy during the downward motion (Cruz, 2008). Therefore, for this study, the external force is composed of both components.

$$F_{ext} = F_{mooring} + F_{PTO} \tag{2.76}$$

According to Cruz (2008), a common approximation for the force of the PTO mechanism, which is not always realistic, is the representation of a linear viscous damper model. Power Take-off is a system connected to the renewable energy device, that converts the energy of the motion of the body into a useful form of energy, such as electric and pneumatic. The magnitude of the PTO damping B_{PTO} is dependent on the amount of power the generator delivers to the grid.

$$F_{PTO} = -B_{PTO} * \dot{Z} \tag{2.77}$$

The mooring forces have a significant influence on the WECs motion and are generally represented by a linear spring model:

$$F_{mooring} = -K_{mooring} * Z \tag{2.78}$$

where, $K_{mooring}$ represents the stiffness of the mooring system.

2.4.2 Wave/fluid-induced forces

For preliminary WEC models, the forces remain in the diffraction regime (Cruz, 2008). The wave/fluid-induced forces are composed of three forces (excitation, radiation and hydrostatic), each component can be calculated separately. The excitation and radiation forces represent the reaction of the body to the incident wave motion. In contrast, the hydrostatic component is unrelated to the incident wave motion.

$$F_f(t) = F_s(t) + F_R(t) + F_H(t) \tag{2.79}$$

Where F_s represents the Excitation force, F_R correspond to the Radiation force, and F_H is the Hydrodynamic force. The Excitation force refers to the force that would act in the body by the fluid if the body was fixed in its monimal position (Cruz, 2008). This force is composed by two contributions: incident and diffracted waves that depends on the wave amplitude.

$$F_s(t) = Re\left[\varsigma_a(\mathbb{X})\, e^{i\omega t}\right], \qquad \mathbb{X} = \mathbb{X}_{inc} + \mathbb{X}_{diff} \tag{2.80}$$

Where $\mathbb{X}_{inc}$ represents the forces of the incident waves, and $\mathbb{X}_{diff}$ the Diffracted waves. The $\mathbb{X}_{inc}$ component is obtained integrating the pressure caused by the incident waves over the wetted surface of the body (Cruz, 2008). This contribution is associated to the Froude-Krylov force. Figure 2.26 illustrates the incident and diffracted waves.

Figure 2.26: Incident waves and diffracted waves

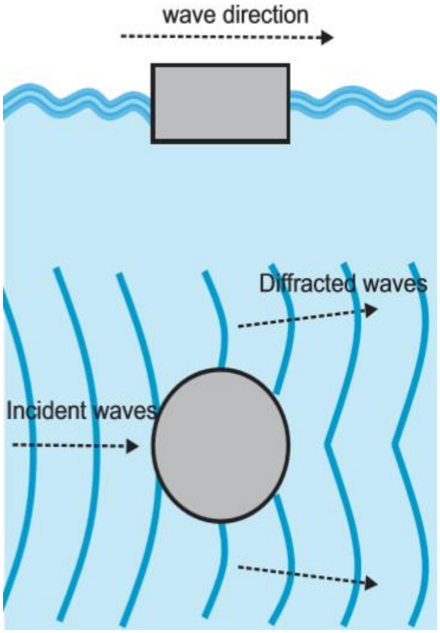

Source: Author (2017).

It is necessary to determine the pressure field over the whole body to calculate the component related to the diffracted waves. If the diffracted component has an insignificant magnitude compared to the incident component $|\mathbb{X}_{inc}| \gg |\mathbb{X}_{diff}|$, the exciting force can be simplified to the incident waves (Cruz, 2008). This simplification is known as Froude-Krylov Approximation. This simplification is valid for buoys with small radius compared to the wavelength.

The Radiation force refers to the force that the body experience due to its own oscillatory movement (Cruz, 2008). This component does not have the influence of the incident wave field. The magnitude of the force is proportional to the body velocity $\dot{\xi}$ in the linear theory. Usually the radiation force is described by two components: one term is in phase with the body acceleration (added mass), and the other with the body velocity (damping coefficient).

$$F_R = -A(\omega)\ddot{Z} - B(\omega)\dot{Z} \tag{2.81}$$

Where $A(\omega)$ represents the Hydrodynamic added mass, and $B(\omega)$ is the Hydrodynamic damping coefficient. The determination of $A(\omega)$ and $B(\omega)$ analytically are restricted to simple geometries, consequently, the components are solved by numerical method. Figure 2.27 illustrates the radiated waves.

Figure 2.27: Radiated waves

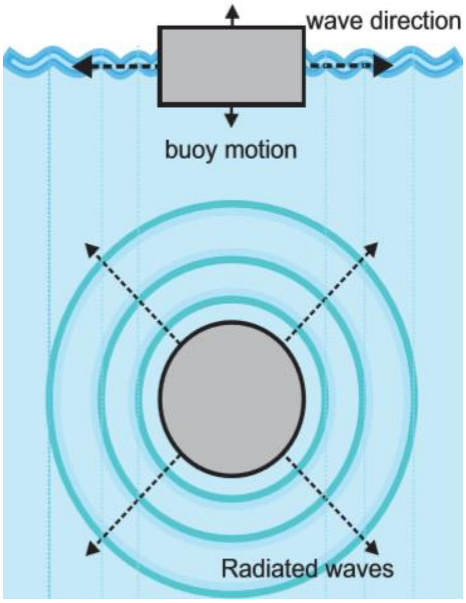

Source: Author (2017).

This work divides the hydrostatic force (F_H) into two distinct forces, Hydrodynamic stiffness force ($F_{K\,Hydro}$) and Buoyancy Force ($F_{buoyancy}$). The hydrodynamic stiffness force refers to the buoyancy force around its equilibrium position (heave) or restoring moment (pitch) that acts in the body.

$$F_H(t) = F_{K\ Hydro}(t) + F_{buoyance} \tag{2.82}$$

For a floating-Point Absorber in heave, the force is caused due to the variation of submerged volume, resulting in an oscillatory motion. For a geometry with a constant transverse area, the buoyancy stiffness is proportional to the elevation, and the hydrostatic force can be described as a linear function. However, for a fully submerged buoy, the hydrostatic force in heave motion is null. The Hydrodynamic stiffness force for pitching is like the ship intact stability theory, and the magnitude of the hydrodynamic stiffness depends on the GZ curve.

$$F_{K\ Hydro}(t) = -K_{Hydro}\ \mathrm{Z} \tag{2.83}$$

The buoyancy force results in a pre-tension in the tether equal to the difference between the buoyancy force ($F_{buoyancy}$) and the Body weight force (F_{weigth}). According to Archimedes' principle, the buoyancy force is equal to the weight of fluid displaced by the body, and acts at the center of buoyancy. Therefore, pre-tension force can be written as:

$$F_{pre-tension} = F_{buoyancy} - F_{weight} \tag{2.84}$$

$$F_{pre-tension} = g(\ \nabla\ \rho - \mathrm{m}_{buoy}) \tag{2.85}$$

Where ∇ is the water displacement of the buoy. The resulting equation for a single degree of freedom is performed combining the hydrodynamic approximations for the wave-fluid interaction forces. The terms that does not depend on the time, does not interfere in the oscillatory motion in heave. Therefore, the oscillatory response of the body can be written for heave motion as:

$$\left(\mathrm{m}_{buoy} + A\right)\ddot{Z} + (B + B_{PTO})\dot{Z} + (K_{mooring} + K_{Hydro})Z = Re\left\{\varsigma_a \mathbb{X}\, e^{-i\omega t}\right\} \tag{2.86}$$

Assumptions:

- the forces remain in the diffraction regime
- the amplitude of the body and the wave are comparable
- linear waves
- external forces are in an agreeable form

The equation represents a single translational mode of motion. To describe the entire movement is necessary to include three translational modes of motion (surge, heave, and sway) and three rotational modes (roll, pitch, and yaw). The equation can be extended to a column vector of six elements, where the first three components are associated with the translational modes and the second three are associated with the rotational modes. In a similar manner, the forces and moments are represented by a vector according to the translational and rotational modes.

$$\sum_{j=1}^{6}\left[(\mathrm{m}_{buoy\ kj}+A_{kj})\ddot{X}_j+(B_{kj}+B_{PTO_{kj}})\dot{X}_j+(K_{Hydro_{kj}}+K_{mooring_{kj}})X_j\right]=Re\{\varsigma_a\mathbb{X}_k e^{-i\omega t}\} \qquad (2.87)$$

Where $k = 1,2, \ldots ,6$.

Considering that the ocean waves can be represented as a sum of independent harmonic series, the incident waves will excite the buoy in different frequencies. The summation will be a combination of all sea state frequencies and their phases. Therefore, $A(\omega)$ and $B(\omega)$ needs to be estimated for the sea spectrum, just the hydrostatic component remains unchanged.

2.4.3 Purely Heaving motion of a fully submerged Point Absorber

The modeling of a single point absorber in heave motion can be represented as a mechanical oscillator composed of a spring-mass-damper with external force, which represents the wave excitation (Backer, 2009). The mass and damping coefficients are dependent on the frequency of excitation.

Figure 2.28: Free-body diagram

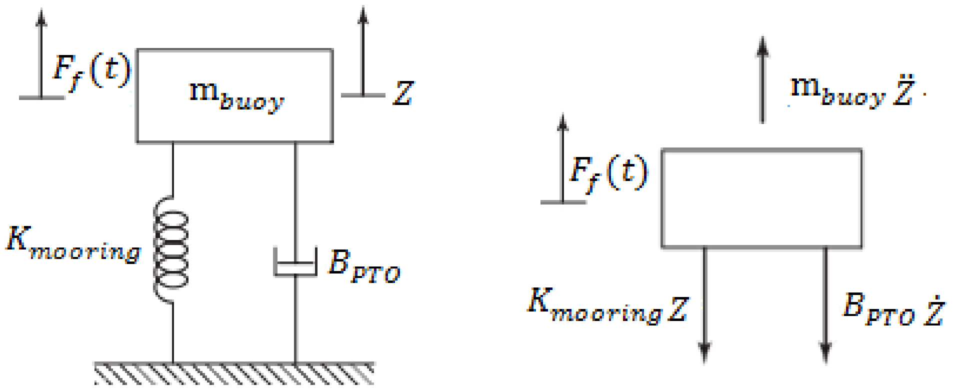

Source: Author (2017).

The governing equation that describes the motion can be derived from Newton's Second Law of motion, which states that the rate of change of momentum of a mass is equal to the force acting on it (Rao, 2011). Therefore, for a single-degree-of-freedom, the system can be described as:

$$\sum F = \frac{d}{dt}\left(\mathrm{m}_{buoy}\ \frac{d\vec{x}(t)}{dt}\right) \tag{2.88}$$

$$\mathrm{m}_{buoy}\ \ddot{Z} = F_s(t) + F_R(t) + F_{mooring} + F_{PTO} \tag{2.89}$$

$$\mathrm{m}_{buoy}\ \ddot{Z} = Re(\varsigma_a(\omega)\mathbb{X}\,(\omega)e^{-i\omega t}) - A(\omega)\ddot{Z} - B(\omega)\dot{Z} - K_{mooring}Z - B_{PTO}\dot{Z} \tag{2.90}$$

$$\left[\mathrm{m}_{buoy}\ + A(\omega)\right]\ddot{Z} + [B(\omega) + B_{PTO}]\dot{Z} + K_{mooring}Z = Re\left(\varsigma_a(\omega)\mathbb{X}(\omega)\ e^{-i\omega t}\right) \tag{2.91}$$

Assumptions for heave motion:

- The viscous friction can be neglected;
- Fully submerged buoy does not have hydrodynamic stiffness;
- The pre-tension force does not affect the body response;
- The forces remain in the diffraction regime;
- Linear waves;
- The body is considered a material point;

The body is expected to oscillate at the same frequency as the force (Rao, 2011). Therefore, its motion can be described as a harmonic motion in complex form.

$$Z(t) = Re\ \left(\xi\ e^{i\omega t}\right) \tag{2.92}$$

$$\dot{Z}(t) = Re\left(i\ \omega\ \xi\ e^{i\omega t}\right) \tag{2.93}$$

$$\ddot{Z}(t) = Re\ \left(-\xi\omega^2 e^{i\omega t}\right) \tag{2.94}$$

The complex constant ξ is the body displacement amplitude, and it is determined solving the general equation, which corresponds to the magnitude of the wave oscillation. The phase is also important and may present a delay from the incident wave. Combining the hydrodynamic approximations for the wave-fluid interaction forces, it results in:

$$Re\left\{\left[-\left(\mathrm{m}_{buoy}\ + A(\omega)\right)\omega^2 - (B(\omega) + B_{PTO})i\omega + (K_{mooring})\right]\xi e^{i\omega t}\right\} = Re\left(\mathbb{X}(\omega)\ e^{i\omega t}\right) \tag{2.95}$$

$$\xi(\omega) = \frac{\varsigma_a(\omega)\mathbb{X}(\omega)}{\{K_{mooring} - [\mathrm{m}_{buoy} + A(\omega)]\omega^2\} + [B(\omega) + B_{PTO}]i\omega} \tag{2.96}$$

Separating the equation into the real and imaginary part, the equation can be written as:

$$\xi(\omega) = \varsigma_a(\omega)\mathbb{X}(\omega)\left[\frac{K_{mooring} - [\mathrm{m}_{buoy} + A(\omega)]\omega^2}{\{K_{mooring} - [\mathrm{m}_{buoy} + A(\omega)]\omega^2\}^2 + [B(\omega) + B_{PTO}]^2\omega^2} \right. \dots$$
$$\left. - i\frac{[B(\omega) + B_{PTO}]\omega}{\{K_{mooring} - [\mathrm{m}_{buoy} + A(\omega)]\omega^2\}^2 + [B(\omega) + B_{PTO}]^2\omega^2}\right] \tag{2.97}$$

via the following relations:

$$x + iy = Ae^{i\phi} \tag{2.98}$$

$$A = \sqrt{x^2 + y^2} \tag{2.99}$$

$$\phi = \frac{y}{x} \tag{2.100}$$

Equation 2.97 can be rewritten as:

$$\xi(\omega) = \frac{\varsigma_a(\omega)\mathbb{X}(\omega)}{\sqrt{\{K_{mooring} - [\mathrm{m}_{buoy} + A(\omega)]\omega^2\}^2 + \{[B(\omega) + B_{PTO}]\omega\}^2}}e^{-i\phi} \tag{2.101}$$

$$\phi = \tan^{-1}\left(\frac{[B(\omega) + B_{PTO}]\omega}{K_{mooring} - [\mathrm{m}_{buoy} + A(\omega)]\omega^2}\right) \tag{2.102}$$

where ϕ is the phase between the force and the buoy displacement. It can be observed that the heave amplitude is proportional to the wave amplitude, and the phase shift does not depend on the wave amplitude. The time domain solution for a fully submerged point absorber oscillating in heave can be represented as:

$$Z(t) = \frac{\varsigma_a(\omega)\mathbb{X}(\omega)}{\sqrt{\{K_{mooring} - [\mathrm{m}_{buoy} + A(\omega)]\omega^2\}^2 + \{[B(\omega) + B_{PTO}]\omega\}^2}}e^{i(\omega t-\phi)} \tag{2.103}$$

The instantaneous power $P(t)$ represents the instantaneous rate of work. The mathematical model for a general force $F(t)$, acting on a body in a single translational mode of motion, can be described as:

$$P(t) = F_{PTO}(t) * \dot{Z} \tag{2.104}$$

For a Point absorber, the conversion of energy represents the energy dissipated from the mechanical system, which is converted into electrical energy. The average of the power extracted (P_{mean}) from the wave by the PTO system over the time interval [0,t] is given by:

$$P_{mean} = \frac{1}{t}\int_0^t B_{PTO}\dot{Z}^2 \, dt \tag{2.105}$$

In the frequency domain, the PTO mean power absorption can be described as:

$$P_{mean}(\omega) = \frac{1}{2} B_{PTO} * \left|\dot{\xi}(\omega)\right|^2 \tag{2.106}$$

2.4.4 Response to irregular waves – Frequency Domain

The response amplitude, also referred as Response Amplitude Operator (RAO), is represented as:

$$\left|\frac{\xi}{\zeta_a}(\omega)\right| = \frac{\mathbb{X}(\omega)}{\sqrt{\left\{K_{mooring} - \left[\mathrm{m}_{buoy} + A(\omega)\right]\omega^2\right\}^2 + \{[B(\omega) + B_{PTO}]\omega\}^2}} \tag{2.107}$$

The response can be divided into three parts: low frequency, natural frequency, and high frequency, which depends mostly on the restoring spring, damping, and mass respectively. Figure 2.29 illustrates the range of response in each case for a floating cylinder.

Figure 2.29: RAO of a floating cylinder

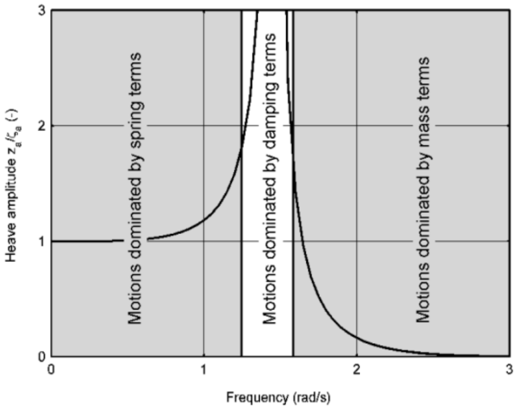

Source: Journée and Massie (2001).

The buoy heave response spectrum can be calculated using the transfer function and the wave spectrum. Figure 2.30 illustrates the response of the body according to the wave spectrum. The following equation describes the heave response spectrum (Journée and Massie, 2001):

$$S_{\xi}(\omega) = \left|\frac{\xi}{\varsigma_a}(\omega)\right|^2 S_{\varsigma}(\omega) \tag{2.108}$$

Figure 2.30: Principle of transfer of waves into responses

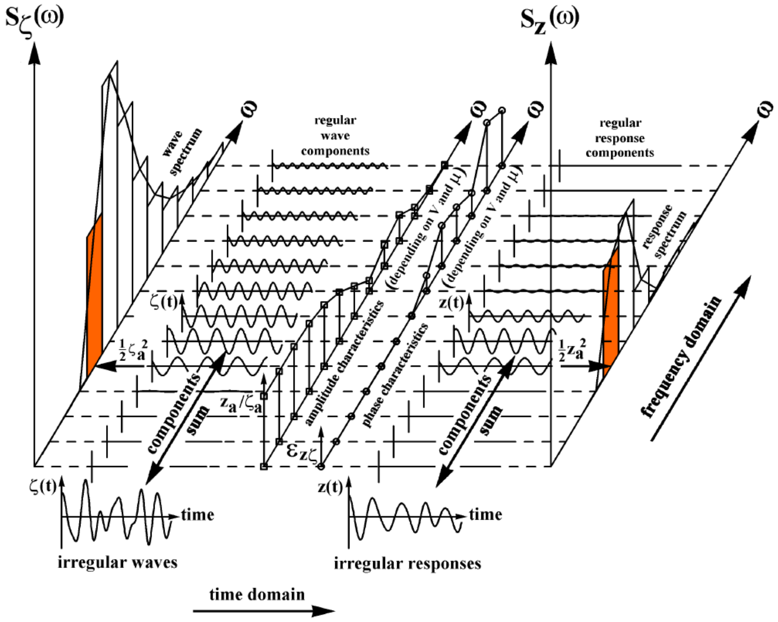

Source: Journée and Massie (2001).

The main objective for WEC devices is the power extracted from the waves. For an irregular wave, the power is calculated summing all contributions of each component, as:

$$P_{mean} = \sum_{n=1}^{N} \frac{1}{2} B_{PTO} * \left|\dot{\xi}_n(\omega)\right|^2 \tag{2.109}$$

2.4.5 Response to irregular waves – Spectral-Domain Model

The frequency domain model assumes that each wave frequency is analyzed independently and the power estimation is calculated by the linear summation of the entire spectrum. This approach provides reasonable results for small displacements and when the non-linear forces are insignificant. However, the physics of WEC devices involves non-linear hydrodynamics even in moderate sea states (Folley and Whittaker, 2010). A common alternative to the frequency domain is the time domain model that allows the implementation of non-linear force. Unfortunately, the time domain model is the high computational effort, which makes it inappropriate to evaluate a large number of scenarios and optimization.

The Spectral domain model is an extension of the frequency-domain model that permits the inclusion of non-linear forces (Folley and Whittaker, 2010). Therefore, it can provide a better estimation of the WEC performance. An advantage of this method is the low computational cost compared to the time-domain model.

Figure 2.31: Spectral domain transfer function

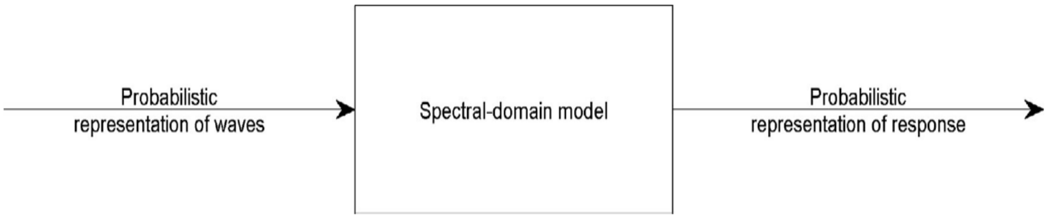

Source: Folley (2016).

The spectral model uses an iterative process to estimate the quasi-linear coefficients for the non-linear elements. This quasi-linear coefficient depends on the complete field, which includes a contribution to the velocity component of other frequencies (Folley, 2016). This quadratic damping pushes the energy to other frequency components, which goes contrary to the orthogonality. However, as the amount of energy is comparatively small, the assumption of orthogonality is still valid.

2.4.5.1 Spectral modeling of quadratic damping

The quadratic damping is proportional to the velocity squared, and it is the most common approximation for nonlinear forces in hydrodynamic of WEC caused by a turbulent boundary layer and vortices. The Morison's equation models the drag force as:

$$F_{Drag} = C_{quadratic} * \dot{\xi} * \left|\dot{\xi}\right| \qquad (2.110)$$

where,

$$C_{quadratic} = \frac{1}{2} * C_D * \rho * S_{\text{Area}} \tag{2.111}$$

where C_D is the draf coefficient, and S_{Area} is the projected area. It is important to notice that the quasi-linear damping is different from the linearized damping coefficient for quadratic damping of a monochromatic wave. The quasilinear drag coefficient is given by:

$$D_j = 2C_{quadratic}\sqrt{\frac{1}{\pi}\sum_j \omega_j{}^2 * \left|\xi_j\right|^2} \tag{2.112}$$

The spectral domain is formulated using the same structure of the frequency-domain except by the quasi-linear coefficient D_j. The response of the WEC device can be obtained from (Folley, 2016):

$$\xi(\omega) = \frac{\varsigma_a(\omega)\mathbb{X}(\omega)}{\left\{K_{mooring} - \left[\mathrm{m}_{buoy} + A(\omega)\right]\omega^2\right\} + \left[B(\omega) + B_{PTO} + D_j\right]i\omega} \tag{2.113}$$

This representation appears similar to a frequency domain model. However, it differs significantly, as the response depends on all frequencies.

2.4.5.2 Solving a Spectral domain model

The spectral domain solution has no analytical solution. Hence, an iterative method is applied to solve the equation. The solution requires an initial guess, and subsequently, it generates successive approximations until the convergence. For an initial guess, the nonlinear forces are considered negligible. Hence, the system is considered linear, and the frequency domain solutions can be applied, which is easily calculated. The estimated results of each iteration are used as an initial guess for the next iteration until the convergence is reached. The convergence criteria is a residual error less than 0.1% of the response.

As the nonlinear forces are not dominant, the solutions converge effortlessly. A suitable relaxation method can contribute to guarantee the convergence, where it is applied a weight factor to the previous quasilinear coefficient, where r is the weight factor that defines the relaxation rate, and j is the frequency of interest:

$$D_j = rD_j{}^- + (1-r)D_j{}^+ \tag{2.114}$$

2.4.6 Relative-motion analysis (translating coordinate system)

The motion in a general plane can be expressed as a combination of translation and rotation (Hibbeler, 2015). This type of analysis is valid to determinate the motion on the same rigid body (Hibbeler, 2015). Therefore, it is important to analyze the buoy motion for a non-distributed mass with a tether attached to a certain distance of the center of gravity. The relative motion is based on a common base point, for this specific purpose, all the forces are translated to the center of buoyancy of the buoy. The relative displacement of a point can be described as:

$$dr_B = dr_A + dr_{B/A} \tag{2.115}$$

$$dr_{B/A} = r_{B/A} d\theta \tag{2.116}$$

Figure 2.32: Relative displacement

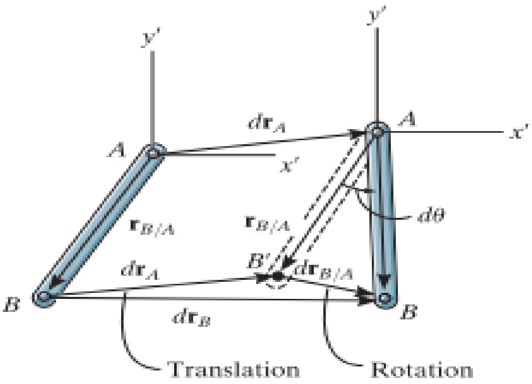

Source: Hibbeler (2015).

The total displacement of the point B (dr_B), is a sum of two components, the translational displacement of the point A (dr_A) and the rotational displacement about A ($dr_{B/A}$) (Hibbeler, 2015). The velocity is estimated dividing the displacement by dt (Hibbeler, 2015).

$$V_B = V_A + V_{B/A} \tag{2.117}$$

$$\frac{dr_B}{dt} = \frac{dr_A}{dt} + \frac{dr_{B/A}}{dt} \tag{2.118}$$

$$\frac{dr_{B/A}}{dt} = r_{B/A}\dot{\theta} = \dot{\theta} \times r_{B/A} \tag{2.119}$$

Figure 2.33: Relative velocity

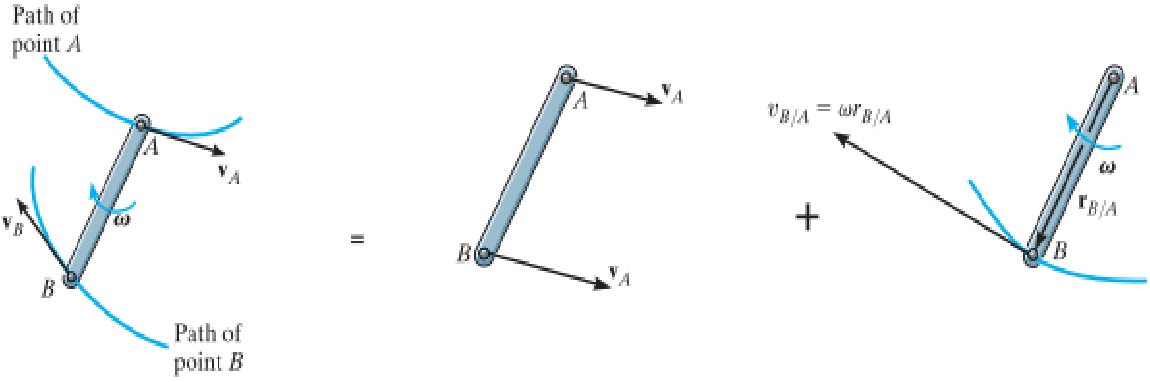

Source: Hibbeler (2015).

The velocity of point B (V_B) is determined considering two components, the translational velocity of the point A (V_A) and the rotational velocity about A ($V_{B/A}$). In the Cartesian vector analysis, the rotational velocity is written as a cross product. The relative acceleration of two points is determined differentiating the relative velocity with respect to time

$$\frac{dV_B}{dt} = \frac{dV_A}{dt} + \frac{dV_{B/A}}{dt} \tag{2.120}$$

Figure 2.34: Relative acceleration

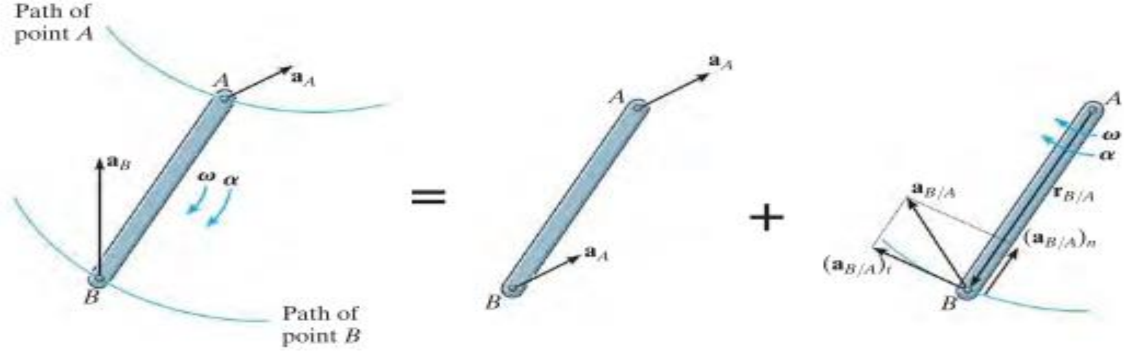

Source: Hibbeler (2015).

The acceleration component of B with respect to A is composed by a tangential and normal acceleration. Therefore, the final equation is described as:

$$a_B = a_A + \ddot{\theta} \times r_{B/A} - \dot{\theta}^2 r_{B/A} \tag{2.121}$$

3 METHODOLOGY

In this section, the methodology is divided into four parts. Firstly, the site and wave properties are analyzed, and the mean energy of the site is calculated. Secondly, the mathematical modeling of Point Absorbers is derived, and some simplifications are presented to evaluate the power extraction. Thirdly, a sensitivity study is conducted to investigate point absorber parameters that influence in the power extraction under regular and irregular waves. Finally, the best configuration is defined, and the power extraction is calculated.

3.1 IMBITUBA ANALYSIS

The literature review suggests the implementation of WEC devices in South America. This work implements the CETO 5 in Imbituba, located in the south of Santa Catarina, Brazil. The main parameter for a site selection is the available wave power. To estimate the wave power, the evaluation of the power available in each sea state and its respective probability of occurrence is necessary. The estimation of the site sea probability of occurrence uses the scatter diagram presented by Constestabile, Ferrante, and Vicinanza (2015), described the scatter diagram regarding T_e, illustrated in Figure 2.12. As this work utilizes a JONSWAP spectrum, and the input variables for this spectrum uses the peak period T_p , a relationship between T_p and T_e was made to calculate the spectrum.

$$T_p = C1 * T_e \tag{3.1}$$

In this regard, several spectrum were computed using Equation 2.58, and the peak period was varied in the whole range of the Imbituba sea state. The mean energy period was calculated for each condition according to the following equation:

$$T_e = 2\pi \frac{\int_0^\infty \omega^{-1}\, S_\varsigma(\omega)\, d\omega}{\int_0^\infty S_\varsigma(\omega)\, d\omega} \tag{3.2}$$

Table 3.1 presents the results obtained for each period calculated.

Table 3.1: T_p, T_e, and T_p/T_e.

$\boldsymbol{T_p}$ **[s]**	$\boldsymbol{T_e}$ **[s]**	$\boldsymbol{T_p/T_e}$
8.0	7.24	1.11
8.5	7.69	1.11
9.0	8.14	1.11
9.5	8.59	1.11
10.0	9.04	1.11
10.5	9.49	1.11
11.0	9.94	1.11
11.5	10.39	1.11
12.0	10.84	1.11
12.5	11.29	1.11
13.0	11.75	1.11
13.5	12.20	1.11
14.0	12.65	1.11
14.5	13.10	1.11
15.0	13.55	1.11
15.5	14.00	1.11
16.0	14.45	1.11
16.5	14.91	1.11

Source: Author (2015).

The results indicated that for a JONSWAP spectrum with $\gamma = 3.3$, T_p is approximately:

$$T_p = 1.1 * T_e \tag{3.3}$$

Based on this relationship a scatter diagram was written in terms of the peak period. The conversion of the scatter diagram into the probability of occurrence of irregular sea state is made taking the number of each event and dividing by the sum of all events and multiplied by 100. Figure 3.1 illustrates the probability of occurrence of irregular sea states.

Figure 3.1: Probability of occurrence of irregular Sea States [%]

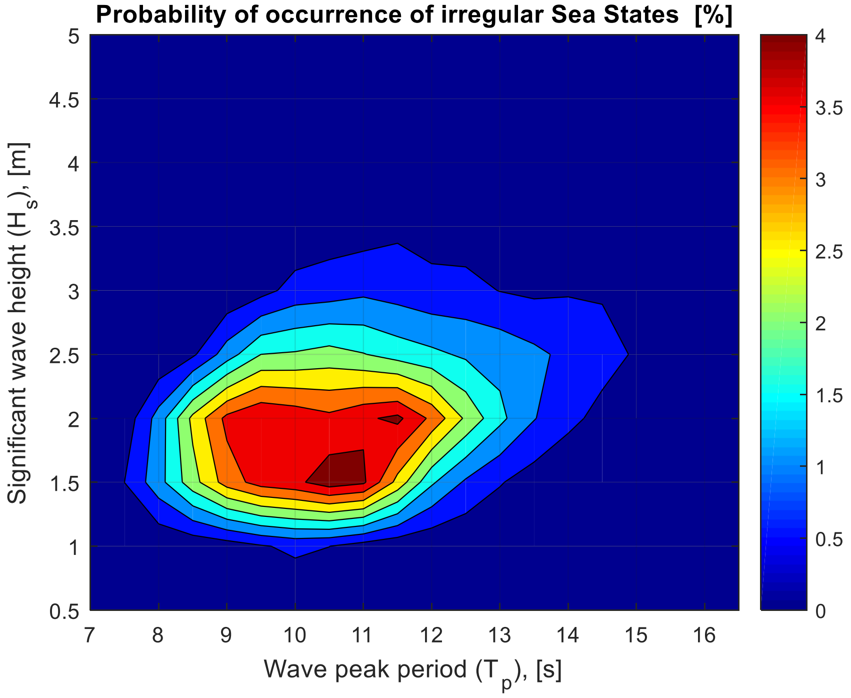

Source: Author (2017).

In order to check the validity of the linear wave theory for the selected sea site, the calculation of the wave slope was conducted according to the Equation 2.4. The result is presented in Figure 3.2, which confirms the theory validity range.

Figure 3.2: Wave Slope for 20 m water depth

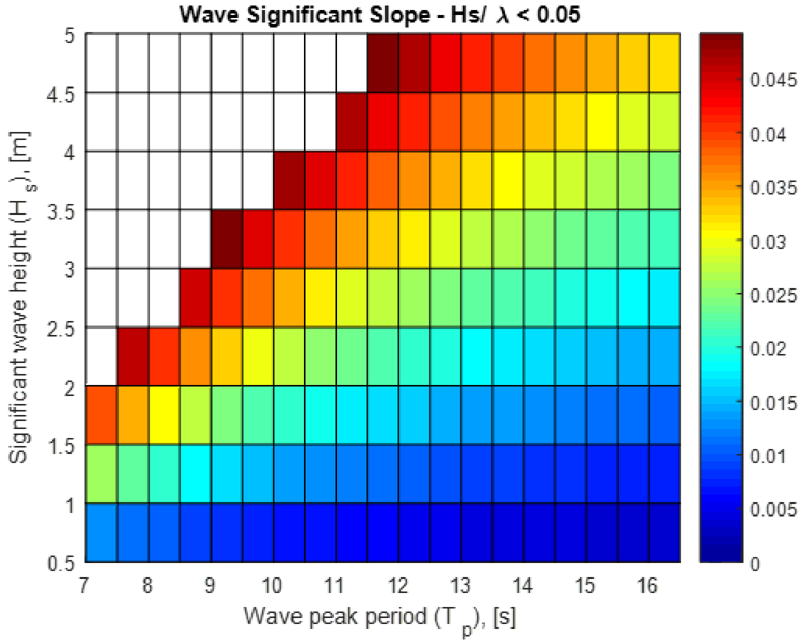

Source: Author (2017).

The probability of occurrence illustrated in Figure 3.1 is used to calculate the mean power of the site and the power extracted by the Point Absorber. Each point in the probability of occurrence of irregular sea state can be represented by a wave spectrum. Figure 3.3 illustrates the wave power spectrum density for several sea states. During this work, the frequency range is discretized into 500 elements, from 0.001 to 3.5 rad/s.

Figure 3.3: JONSWAP spectrum

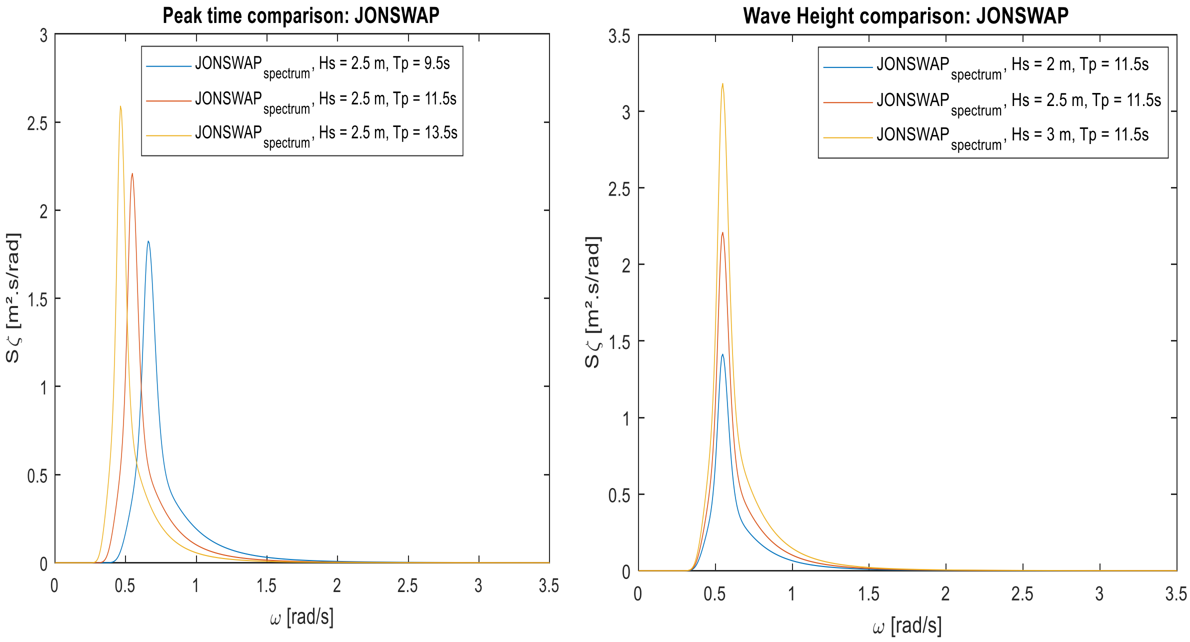

Source: Author (2017).

The wave energy of each sea state was calculated using Equation 2.62 based on the wave power spectrum density. The wave power in shallow water requires a more complex method to calculate. Firstly, the wave number of each frequency was calculated using the fsolve.m function in MATLAB to solve the transcendental equation (Equation 2.27). Secondly, the wave group velocity of each frequency component was calculated based on the wave number. Finally, the Equation 2.64 is computed integrating the entire range of frequencies for all Sea States to calculate the wave power. Figure 3.3 illustrates the wave energy and wave power per unit of horizontal area for 20 m of water depth.

Figure 3.4: Wave Energy and Power - 20 m water depth

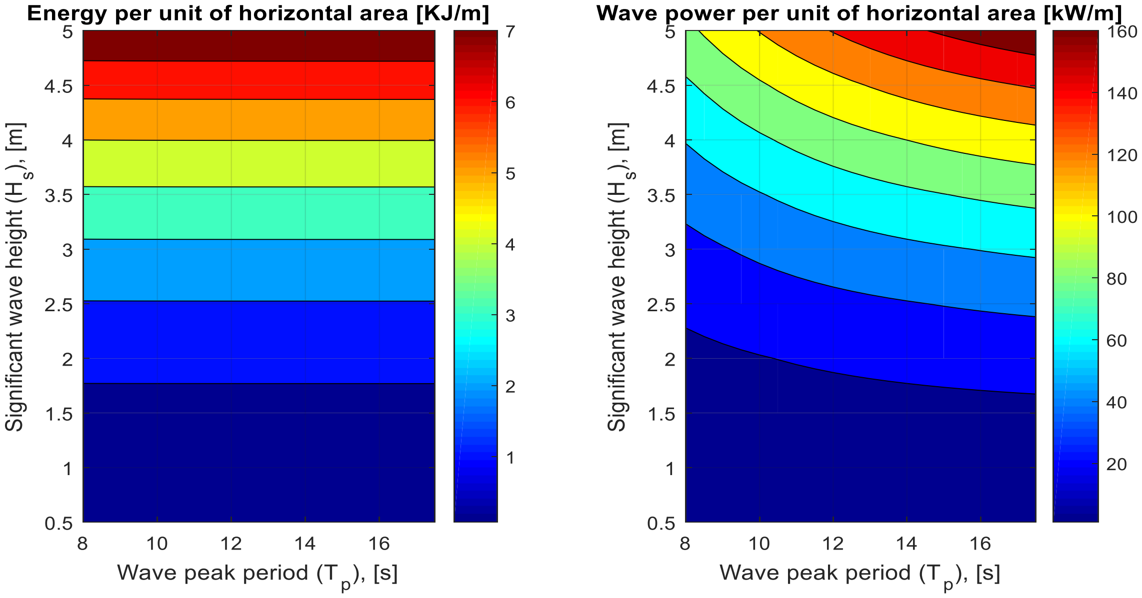

Source: Author (2017).

It can be observed that the wave power increases quadratically with the wave height. As a result, even with less probability of occurrence, the power present at higher wave height is more significant than small waves with a higher probability of occurrence. Figure 3.5 represents the multiplication of the probability of occurrence by its own wave power, representing the approximated wave power in each condition.

Figure 3.5: Wave power probability per unit of horizontal area [W/m]

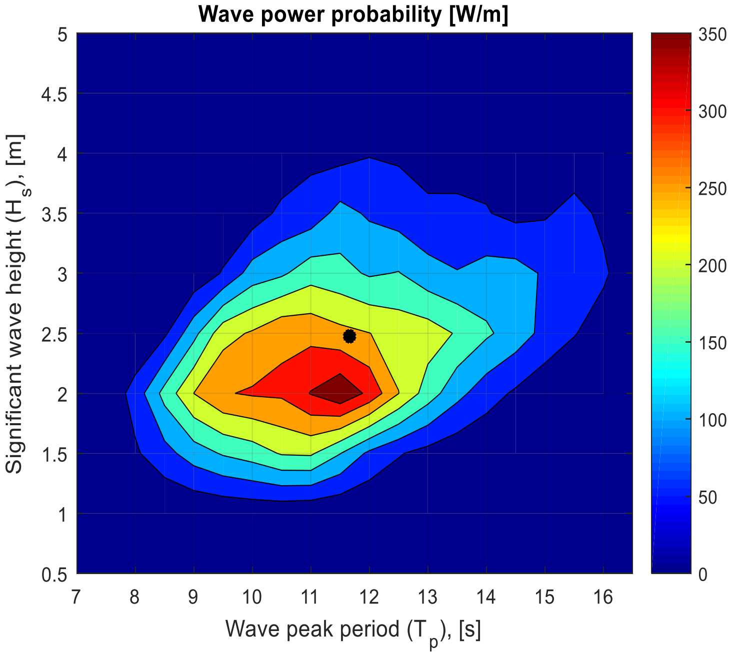

Source: Author (2017).

The center of power probability of Imbituba site is located at wave peak period of $11.5\,seconds$ and $Hs = 2.5\,m$. This value was computed calculating the centroid of the wave power probability, which is represented by a black point in Figure 3.5.

The integral of the wave power probability in each condition results in the average power of the site. The average power estimated by Constestabile, Ferrante and Vicinanza (2015) is 13.95 kW/m. However, the result calculated in this work based on to the scatter diagram was:

$$\bar{W} = 24.4\,kW/m$$

It can be observed that the results of this work diverge from those given by Constestabile, Ferrante and Vicinanza (2015). However, it agrees with Figure 2.9 presented by Cruz (2008). In order to check the validity of the results, it was assumed a water depth equal to 2000 m, to assume deep water condition, and the wave power calculated was:

$$\bar{W} = 21.88\,kW/m$$

An approximated solution, which was described in Equation 2.65, for deep water resulted in:

$$\bar{W}_{approx} = 21.97\,kW/m$$

Therefore, the results are appropriated for deep water. The validation of the model in shallow water is made calculating the wave power of several sites described in Babarit et al. (2012), illustrated in Figure 3.6. The results were compared with Babarit and Hals (2011), that used JONSWAP spectrum ($\gamma = 3.3$). Table 3.2 presents the comparison results.

Table 3.2: Comparison of the wave power per unit crest [kW/m]

Wave Power per unit crest [kW/m]	**SEM-REV**	**EMEC**	**Yeu**
Babarit and Hals (2011)	15.6	23.0	26.8
$\bar{W}$	15.4	22.5	25.9
$\bar{W}_{approx}$ (deep water)	14.3	20.5	23.1

Source: Adapted from Babarit and Hals (2011).

Figure 3.6: Scatter diagram: SEM-REV, EMEC, and Yeu respectively.

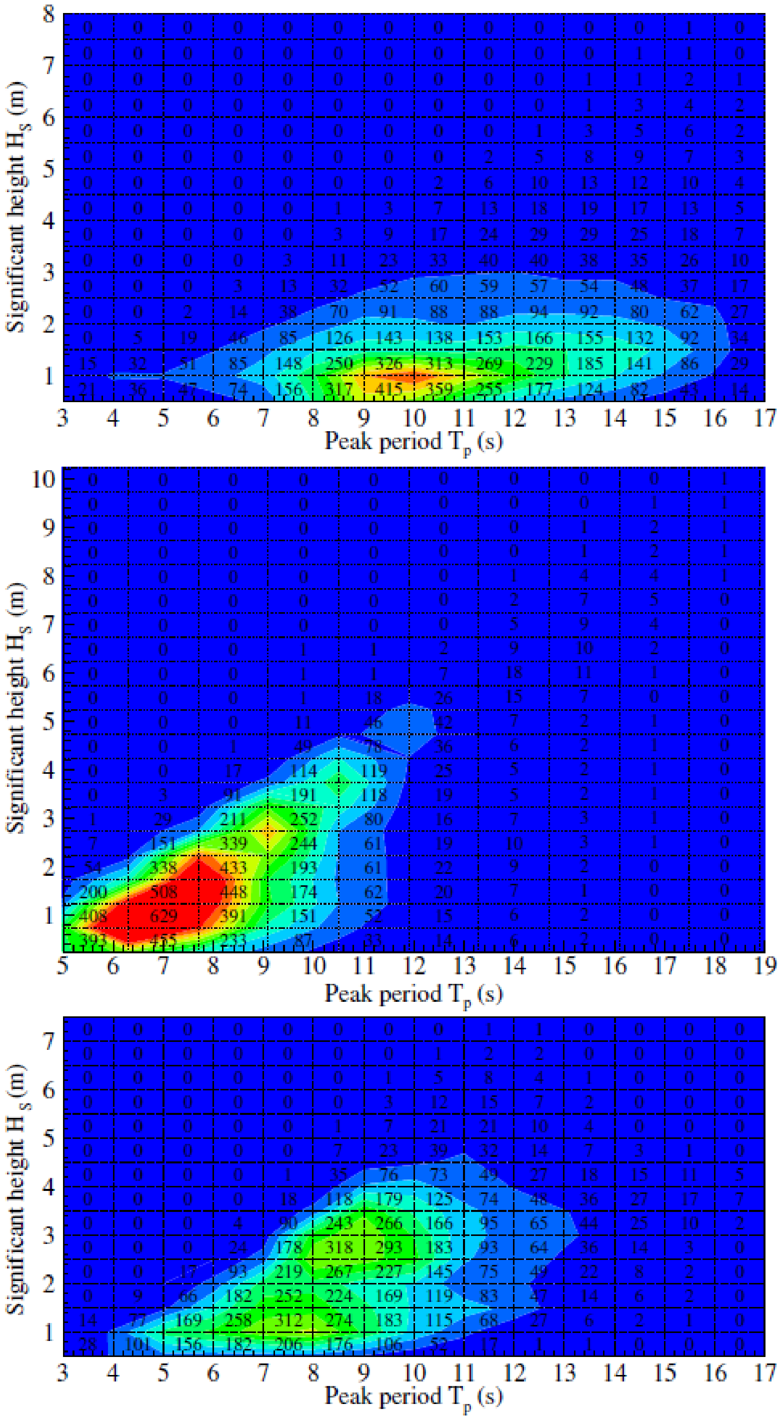

Source: Babarit et Al. (2012).

It can be verified that the results in shallow water are consistent to Babarit and Hals (2011). Hence, this work assumes a wave power available as 24.4 kW/m. As a result, the power available at Imbituba is superior than 20 kW/m, which, according to Milton (2012) is generally accepted as the profitability limit for WECs.

3.2 MATHEMATICAL MODELLING OF POINT ABSORBER

The following studies investigate the complete motion of the fully submerged point absorber, including mass offset, pre-tension force, external forces location, and hydrodynamic coefficients. The first assumption made is: the Point Absorber is insensible to the wave direction. This effect occurs due to its axisymmetric. Hence, the body, which is fully described using 6 degrees of freedom, can be approximated to 3 degrees of freedom (surge, heave, and pitch). Figure 3.7 illustrates the modes of motion, surge, heave, and pitch respectively.

Figure 3.7: Modes of motion

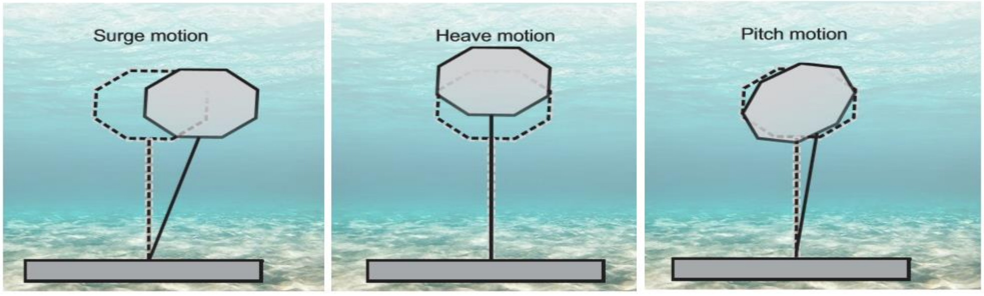

Source: Author (2017).

The modeling of the fully submerged point absorber is based on the CETO 5 characteristics, such as geometry properties and operating conditions, described by Babarit et al. (2012), which is detailed in Figure 3.8.

Figure 3.8: CETO 5 dimensions and properties

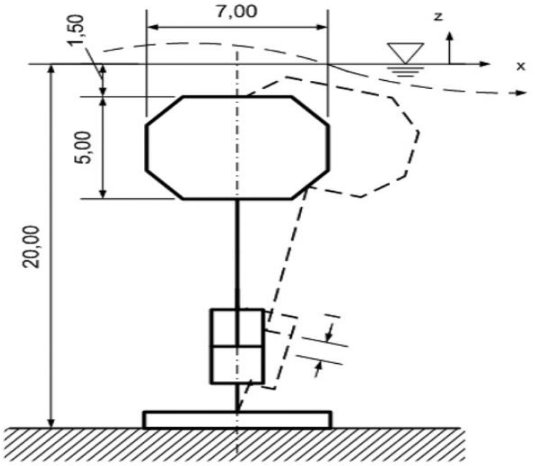

Property	Value	Unit
Diameter	7	m
Height	5	m
Displacement	148	m^3
Mass of the buoy	35000	Kg
Stroke length	6	m
PTO model	Linear	
Char. surface area	220	m^2
Characteristic mass	200000	Kg
Water depth	20	m

Source: Babarit et al. (2012).

As the stiffness and damping parameters are designed according to the respective sea site, these parameters are modified to achieve higher power extraction in this work. The only difference in the geometry is a fillet made at the edges in order to reduce the risk of fluid vorticities, which is suggested by Cruz (2008). Moreover, it is important to notice that the water depth specification described by Babarit et al. (2012) matchs with the conditions proposed by Constestabile, Ferrante, and Vicinanza (2015).

3.2.1 Effect of an offset mass on the body motion

The offset mass impacts mainly in two different aspects of the Point Absorber motion in this work: restoring moment, and relative acceleration.The restoring moment occurs due to the gravitational forces tends to align the center of buoyancy and center of gravity of the buoy in the vertical axis. Figure 3.9 illustrates the moment due to the effect of an offset mass. As the buoy is fully submerged, the equivalent moment acting on the center of buoyancy is equal to:

$$\mathrm{M}_{momentum_{cb}} = -\mathrm{m}_{buoy}\, g\, R_{cg/cb} \sin(\theta_{cb}) \tag{3.4}$$

$$\mathrm{M}_{momentum_{cb}} \approx -\mathrm{m}_{buoy}\, g\, R_{cg/cb}\, \theta_{cb} \tag{3.5}$$

Figure 3.9: Mass restoring moment in pitch motion

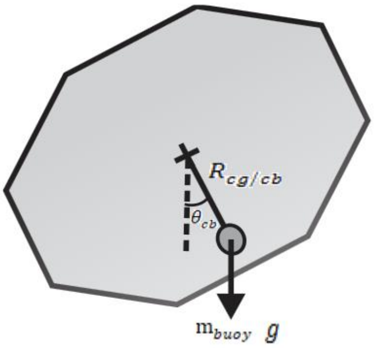

Source: Author (2017).

The effect of an offset mass on the motion due to the relative acceleration occurs when the coordinate is not coincident with the center of mass of the body. The equation that describes the relative acceleration was presented in the Equation 2.121. However, for small displacements, the quadratic angular velocity can be neglected. Therefore, the condition described in Figure 3.10 can be calculated as:

Figure 3.10: Offset mass

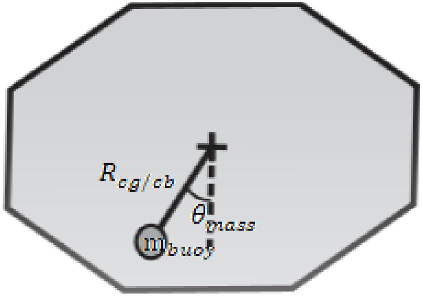

Source: Author (2017).

$$a_B = a_A + \ddot{\theta} \times r_{B/A} \tag{3.6}$$

Where, θ_{mass} is the angle of the mass installation. The matrix representation of the inertia can be expressed as:

$$\begin{bmatrix} \mathrm{m}_{buoy} & 0 & 0 \\ 0 & \mathrm{m}_{buoy} & 0 \\ 0 & 0 & I \end{bmatrix} \begin{Bmatrix} \ddot{x}_{cg} \\ \ddot{z}_{cg} \\ \ddot{\theta}_{cg} \end{Bmatrix} = \begin{bmatrix} \mathrm{m}_{buoy} & 0 & \mathrm{m}_{buoy}\, R_{x_{cg/cb}} \\ 0 & \mathrm{m}_{buoy} & \mathrm{m}_{buoy}\, R_{z_{cg/cb}} \\ \mathrm{m}_{buoy}\, R_{x_{cg/cb}} & \mathrm{m}_{buoy}\, R_{z_{cg/cb}} & I_{cg/cb} \end{bmatrix} \begin{Bmatrix} \ddot{x}_{cb} \\ \ddot{z}_{cb} \\ \ddot{\theta}_{cb} \end{Bmatrix} \tag{3.7}$$

$$R_{x_{cg/cb}} = R_{cg/cb} * \cos(\theta_{mass}) \tag{3.8}$$

$$R_{z_{cg/cb}} = R_{cg/cb} * \sin(\theta_{mass}) \tag{3.9}$$

Where, $I_{cg/cb}$ is the mass moment of inertia that according to the perpendicular axis theorem, is given by (Hibbeler, 2011):

$$I_{cg/cb} = I + \mathrm{m}_{buoy}\, {R_{cg/cb}}^2 \tag{3.10}$$

As the angle of the mass installation in this work is equal to zero, and the pitch angle in steady-state is also zero, the Equation 3.7 can be simplified to:

$$\begin{bmatrix} \mathrm{m}_{buoy} & 0 & 0 \\ 0 & \mathrm{m}_{buoy} & 0 \\ 0 & 0 & I \end{bmatrix} \begin{Bmatrix} \ddot{x}_{cg} \\ \ddot{z}_{cg} \\ \ddot{\theta}_{cg} \end{Bmatrix} = \begin{bmatrix} \mathrm{m}_{buoy} & 0 & \mathrm{m}_{buoy}\, R_{x_{cg/cb}} \\ 0 & \mathrm{m}_{buoy} & 0 \\ \mathrm{m}_{buoy}\, R_{x_{cg/cb}} & 0 & I_{cg/cb} \end{bmatrix} \begin{Bmatrix} \ddot{x}_{cb} \\ \ddot{z}_{cb} \\ \ddot{\theta}_{cb} \end{Bmatrix} \tag{3.11}$$

3.2.2 Effect of the pre-tension force on the body motion

The pre-tension force is equal to the difference between the fluid weight and the buoy weight. In this work, the effect of the pre-tension force is analyzed in the heave, surge, and pitch motion.The pre-tension force results in a tether elongation in the vertical axis. This force changes the mean position of the buoy; however, it does not affect the oscillatory motion in heave.

$$F_{pre-tension_{tether}} = -K_{mooring} * Z_{static_{tether}} \tag{3.12}$$

Unlike the heave motion, the pre-tension force affects the oscillatory in surge motion. Similar to the analysis of an oscillating pendulum, the pre-tension force creates lateral stiffness in surge mode of motion, identical to the weight force in a pendulum. Figure 3.11 illustrates the effect of the pre-tension force in the surge motion of the Point Absorber.

Figure 3.11: Pre-tension force (surge motion)

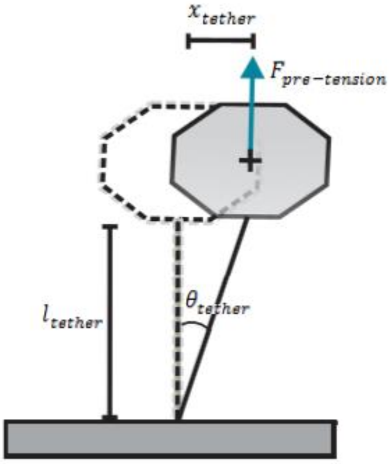

Source: Author (2017).

The force acting on the tether has the same direction as the displacement. Therefore, the lateral stiffness can be written as:

$$\tan(\theta_{tether}) = \frac{x_{tether}}{l_{tether}} = \frac{-F_{x_{tether}}}{\sqrt{F_{z_{tether}}{}^2 + F_{x_{tether}}{}^2}} \approx \frac{-F_{x_{tether}}}{F_{pre-tension}} \tag{3.13}$$

$$F_{x_{tether}} = -\frac{F_{pre-tension}}{l_{tether}} x_{tether} \tag{3.14}$$

Where, l_{tether} is the static displacement of the tether. The translation of the pre-tension force acting on the tether connection to the center of buoyancy is illustrated in Figure 3.12.

Figure 3.12: Pre-tension force (surge motion) - tether

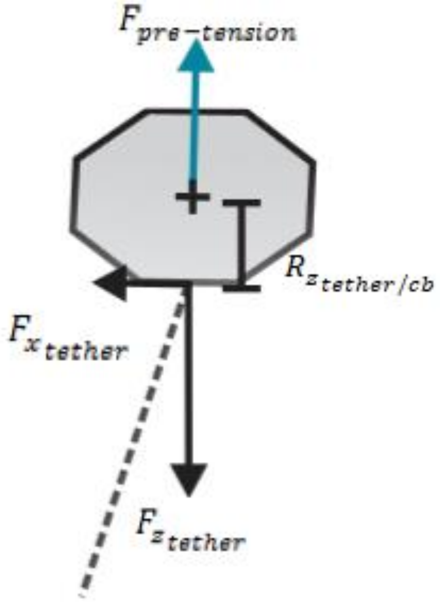

Source: Author (2017).

The mathematical representation is given by:

$$F_{x_{tether}} = -\frac{F_{pre-tension}}{l_{tether}} * (x_{cb} + R_{z_{tether/cb}} * \theta_{cb}) \tag{3.15}$$

The coupling between pre-tension force and tether also affects the pitch angle. The equation that relates the pitch motion is derived via the summation of all moments acting on the buoy. Figure 3.13 illustrates the effect of the pre-tension condition on the pitch motion.

Figure 3.13: Pre-tension force – pitch motion

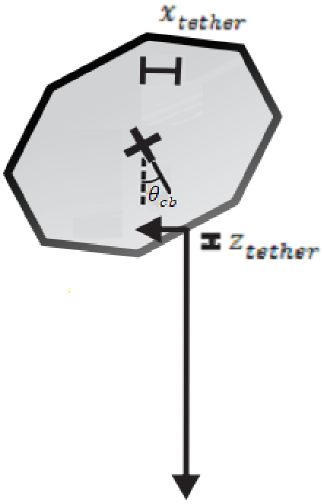

Source: Author (2017).

The displacements to calculate the moments acting is equalt to:

$$x_{tether} = R_{tether/cb}\sin(\theta_{cb}) \approx R_{tether/cb}\,\theta_{cb} \tag{3.16}$$

$$z_{tether} = R_{tether/cb}[1 - \cos(\theta_{cb})] \approx 0 \tag{3.17}$$

The forces can be represented as:

$$F_{x_{tether}} = -\frac{F_{pre-tension}}{l_{tether}} x_{tether} \tag{3.18}$$

$$F_{z_{tether}} = -F_{pre-tension} \tag{3.19}$$

Finally, the moments acting at the center of buoyancy due to the pitch motion can be written as:

$$\sum M_{cb} = F_{x_{tether}} * 0 + F_{z_{tether}} * x_{tether} \tag{3.20}$$

$$\sum M_{cb} = -F_{pre-tension} * R_{tether/cb}\,\theta_{cb} \tag{3.21}$$

The sum of the pre-tension force the and mass restoring moment acting at the center of buoyancy results in the following matrix:

$$\begin{bmatrix} -\frac{F_{pre-tension}}{l_{tether}} & 0 & -\frac{F_{pre-tension} * R_{z_{tether/cb}}}{l_{tether}} \\ 0 & 0 & 0 \\ -\frac{F_{pre-tension} * R_{z_{tether/cb}}}{l_{tether}} & 0 & -\mathrm{m}_{buoy} g R_{cg/cb} - F_{pre-tension} R_{z_{tether/cb}} \end{bmatrix} \begin{Bmatrix} x_{cb} \\ z_{cb} \\ \theta_{cb} \end{Bmatrix} \tag{3.22}$$

3.2.3 External forces (PTO and mooring system)

The external forces analyze the influence of the heave, surge and pitch motion in the PTO mechanism and the mooring system. The external forces depend on the tether elongation and tether velocity and its respective stiffness and damping coefficients. Figure 3.14 illustrates the influence of the heave, surge, and pitch motion on the tether elongation.

Figure 3.14: Elongation due to heave, surge and pitch motion

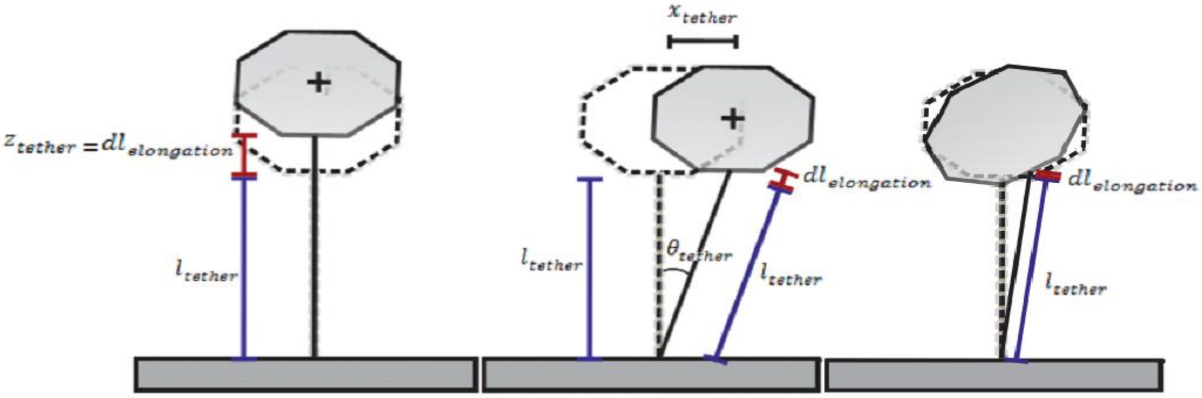

Source: Author (2017).

It can be observed that the heave motion is in the same direction that the tether elongation, therefore:

$$F_{tether_{heave(tether)}} = -K_{mooring}[(l_{tether} + z_{tether}) - l_{tether}] = -K_{mooring} * z_{tether} \tag{3.23}$$

The translation of coordinates to the center of buoyancy results in:

$$F_{tether_{heave(cb)}} = -K_{mooring} * (z_{cb} + R_{x_{tether/cb}} * \theta_{cb}) \tag{3.24}$$

For this case, $R_{x_{tether/cb}}$ is zero, therefore, the equation can be written as;

$$F_{tether_{heave(cb)}} = -K_{mooring} * z_{cb} \tag{3.25}$$

Analog to the $F_{z_{tether}}$, the power take-off can be modelled as:

$$F_{pto_{heave(cb)}} = -B_{PTO} * \dot{z}_{cb} \tag{3.26}$$

On another hand, the surge motion of the buoy has a minor influence on the tether elongation, which is described as:

$$F_{tether_{surge(tether)}} = -K_{mooring}\left[\sqrt{\left({l_{tether}}^2 + {x_{tether}}^2\right)} - l_{tether}\right] \approx 0 \tag{3.27}$$

Similarly, the pitch motion has a minor influence on the tether elongation, and it is described as:

$$F_{tether_{pitch(tether)}} = -K_{mooring}\left\{\sqrt{[(l_{tether} + R_{tether/cb}[1 - \cos(\theta_{cb})]^2) + R_{tether/cb}\sin(\theta_{cb})^2]} - l_{tether}\right\} \approx 0 \tag{3.28}$$

Therefore, the linearization on the mean position results in a neglectable power extraction in surge and pitch motion.

3.2.4 Hydrodynamic coefficients

As the main objective of this section is to model the body response, this work does not extend to the analysis of the hydrodynamics coefficients, and some of the results are presented in APPENDIX A, B, and C. The hydrodynamic coefficients were calculated via computational simulation using the commercial software AQWA by ANSYS, at the University of Adelaide. This software uses the three-dimensional panel method to analyze the hydrodynamic behavior. The method is based on the potential fluid theory and discretizes the structure surface into quadrilateral or triangular panels (mesh), and computes the hydrodynamics coefficients as an average value over each panel surface (ANSYS, 2013).

The hydrodynamic added mass and radiation damping can be represented by a 3x3 matrix. Where, by convention, the index 1, 3, and 5 refers to the surge, heave, and pitch motion respectively.

$$[A(\omega)] = \begin{bmatrix} A_{11}(\omega) & A_{13}(\omega) & A_{15}(\omega) \\ A_{31}(\omega) & A_{33}(\omega) & A_{35}(\omega) \\ A_{51}(\omega) & A_{53}(\omega) & A_{55}(\omega) \end{bmatrix} \tag{3.29}$$

$$[B(\omega)] = \begin{bmatrix} B_{11}(\omega) & B_{13}(\omega) & B_{15}(\omega) \\ B_{31}(\omega) & B_{33}(\omega) & B_{35}(\omega) \\ B_{51}(\omega) & B_{53}(\omega) & B_{55}(\omega) \end{bmatrix} \tag{3.30}$$

The order of magnitude of the hydrodynamic added mass calculated by the software is attached in APPENDIX A. The results show that the heave motion affects the pitch motion and the pitch motion affects the surge motion. On the other hand, the heave motion is independent of the other modes of motion. Therefore, owing to the order of magnitude of the elements, the matrix in Equation 3.29 and Equation 3.30 can be simplified to:

$$[A(\omega)] = \begin{bmatrix} A_{11}(\omega) & 0 & A_{15}(\omega) \\ 0 & A_{33}(\omega) & 0 \\ A_{51}(\omega) & 0 & A_{55}(\omega) \end{bmatrix} \tag{3.31}$$

$$[B(\omega)] = \begin{bmatrix} B_{11}(\omega) & 0 & B_{15}(\omega) \\ 0 & B_{33}(\omega) & 0 \\ B_{51}(\omega) & 0 & B_{55}(\omega) \end{bmatrix} \tag{3.32}$$

The excitation force of a wave with one-meter amplitude acting on the buoy was also computed using AQWA. The order of magnitude of the forces is illustrated in APPENDIX B. The results demonstrate a comparable order of magnitude between the diffraction force and Froude & Krylov force, which might be due to the boys' size. The multiplication between the wave amplitude spectrum and Excitation force results in the force acting on the buoy.

3.2.4.1 Mesh study and verification

As the hydrodynamic coefficients are calculated via panels method; it is important to conduct a mesh study analyzing the effect on the results. In this study, three local element size were selected: 2 m, 1 m, and 0.5 m. Figure 3.15 shows the mesh configuration used to calculate the hydrodynamic properties.

Figure 3.15: Mesh study – buoy - sketch

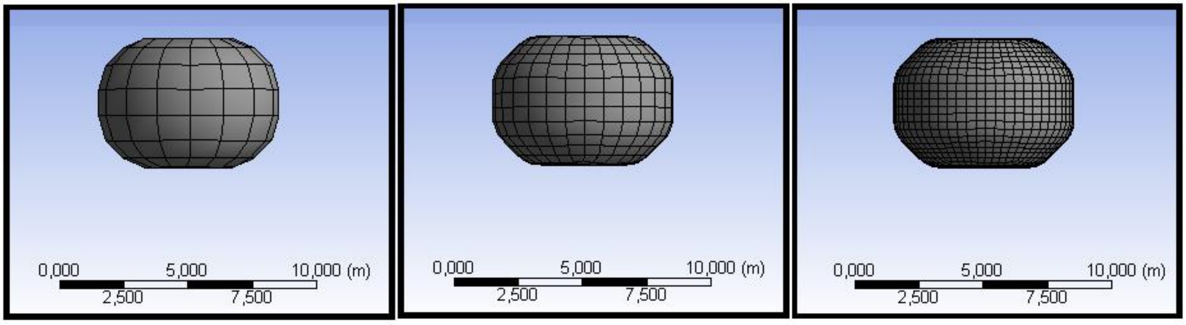

Source: Author (2017).

The number of elements generated in each case was: 144, 422, and 1558 respectively. Only the heave motion was analyzed during the mesh study, and the results can be verified in the APPENDIX C. The element size used to calculate the hydrodynamic properties that is used in this work is equal to 0. 5m.

The results generated by the software AQWA were compared against Babarit and Hals (2011), which used the software Aquaplus. The data were collected visually, and therefore, it might have some small differences with the original source. Figure 3.16 shows the comparison of Radiation damping and Added mass, and Figure 3.17 shows a comparison of the Excitation force.

Figure 3.16: Added mass and Radiation damping - comparison

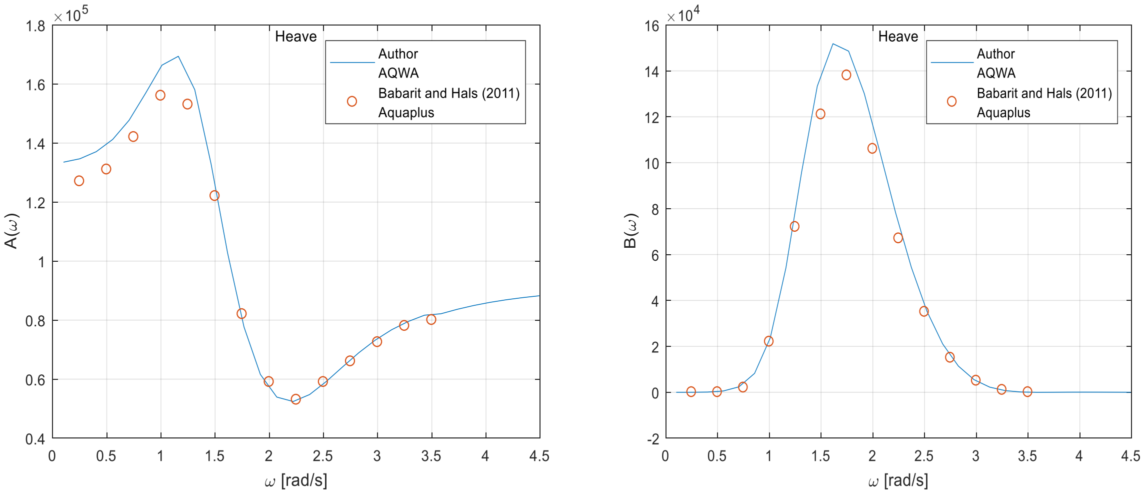

Source: Author (2017).

Figure 3.17: Excitation force comparison

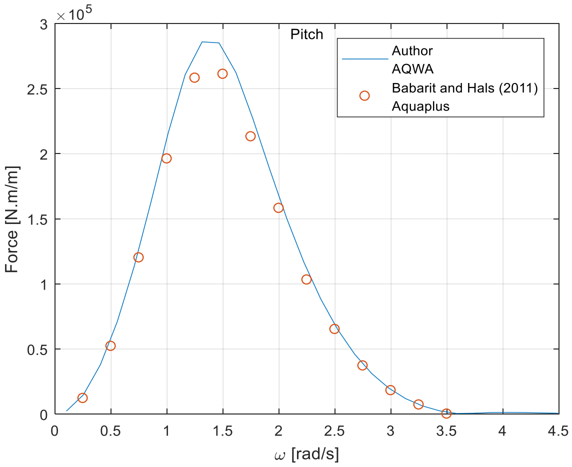

Source: Author (2017).

It can be verified that the order of magnitude between the values computed in the software AQWA and the results from Babarit and Hals (2011) is comparable.

3.2.5 Resulting equation

The resulting equation is composed of three matrices: inertia, damping, and stiffness; and two vectors: force and displacement vector. Each matrix is written as a matrix $n_x n$, where n represents the degrees of freedom. The sum of all components presented in the previous sections are described in the following equations:

Inertia matrix:

$$[M] = \begin{bmatrix} \mathrm{m}_{buoy} + A_{11}(\omega) & 0 & \mathrm{m}_{buoy}\, R_{x_{cg/cb}} + A_{15}(\omega) \\ 0 & \mathrm{m}_{buoy} + A_{33}(\omega) & 0 \\ \mathrm{m}_{buoy}\, R_{x_{cg/cb+}} + A_{51}(\omega) & 0 & I_{cg/cb} + A_{55}(\omega) \end{bmatrix} \tag{3.33}$$

Damping matrix:

$$[B] = \begin{bmatrix} B_{11}(\omega) & 0 & B_{15}(\omega) \\ 0 & B_{PTO} + B_{33}(\omega) & 0 \\ B_{51}(\omega) & 0 & B_{55}(\omega) \end{bmatrix} \tag{3.34}$$

Stiffness matrix:

$$[K] = \begin{bmatrix} \dfrac{F_{pre-tension}}{l_{tether}} & 0 & \dfrac{F_{pre-tension} * R_{z_{tether/cb}}}{l_{tether}} \\ 0 & K_{mooring} & 0 \\ \dfrac{F_{pre-tension} * \ R_{z_{tether/cb}}}{l_{tether}} & 0 & \mathrm{m}_{buoy} g R_{cg/cb} + F_{pre-tension}\, R_{z_{tether/cb}} \end{bmatrix} \tag{3.35}$$

Force vector:

$$\{F_s\} = \begin{Bmatrix} F_{s_x} \\ F_{s_z} \\ F_{s_\theta} \end{Bmatrix} \tag{3.36}$$

Displacement vector:

$$\{u\} = \begin{Bmatrix} x_{cb} \\ z_{cb} \\ \theta_{cb} \end{Bmatrix} \tag{3.37}$$

The body response is written as:

$$\{F_s\} = [M]\{\ddot{u}\} + [B]\{\dot{u}\} + [K]\{u\} \tag{3.38}$$

As it can be observed, the surge motion is coupled to the pitching motion. On the other hand, the heave motion is decoupled from the surge and pitch motion for frequency domain model linearized around the mean position. Therefore, the heave motion can be treated as independent, and the equation can be simplified to:

$$F_{s_z} = \left[\mathrm{m}_{buoy} + A_{33}(\omega)\right]\ddot{z}_{cb} + \left[B_{PTO} + B_{33}(\omega)\right]\dot{z}_{cb} + \left[K_{mooring}\right]z_{cb} \tag{3.39}$$

Hence, the position of the mass is not investigated in this model. The decoupled equation shows that for small displacements, only the heave motion can extract the energy of the system. The power extracted was calculated using Equation 2.109, where the vertical velocity $\dot{\xi}$ is equal to:

$$\dot{\xi}(\omega) = \frac{i\omega\mathbb{X}\chi_z(\omega)}{\{K_{mooring} - [\mathrm{m}_{buoy} + A(\omega)]\omega^2\} + [B_{33}(\omega) + B_{PTO}]i\omega} \tag{3.40}$$

3.2.5.1 Verification

The verification of the RAO and power absorbed functions were made simulating a condition with stiffness equal to 100 kN/m and damping 25kN/m.s The results were compared against the values provided by Babarit and Hals (2011) for the same condition. Figure 3.18 shows the comparison of RAO functions, and power absorbed functions.

Figure 3.18: Frequency domain verification

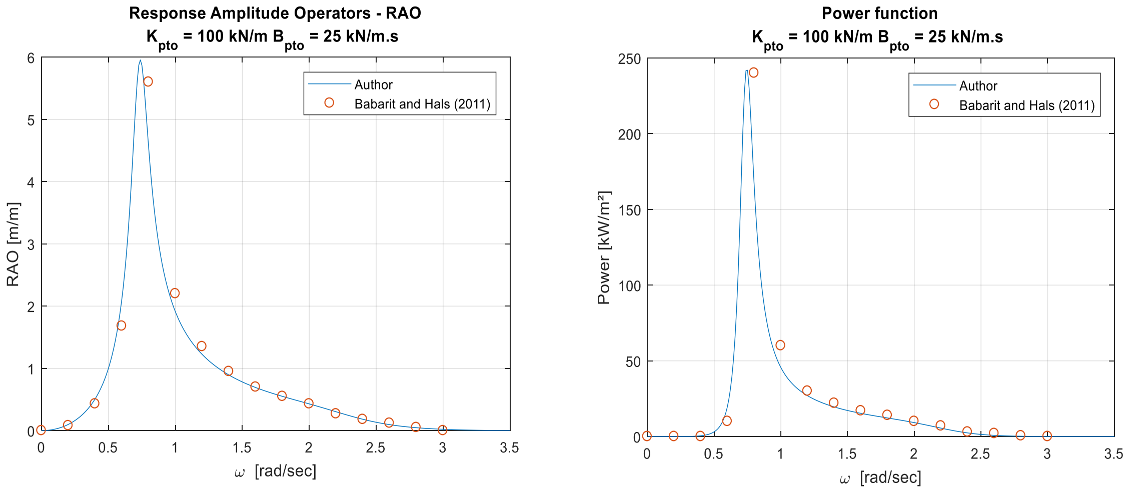

RAO

Power Absorbed

Source: Author (2017).

3.3 SENSITIVITY STUDIES

In this subsection, several sensitivity studies are conducted to investigate the effects of some parameters such as damping, stiffness, mass, and stroke limitation in the power absorption for regular and irregular waves. As the performance in irregular waves is the main objective of this work, a simple analysis is conducted on regular waves, assuming neglectable viscous forces. On the other hand, the analysis in irregular waves is more detailed and includes the viscous drag effect.

3.3.1 Power extraction optimization under regular waves

If the system's natural frequency ω_n for heave matches to the incident wave frequency, the system will operate in a resonant condition that enlarge its power extraction (Cruz, 2008). This condition can be achieved setting the mass of the buoy and stiffness of the spring. As a result, the magnitude of the displacement, velocity, and acceleration of the system increases substantially.

$$\omega_n = \sqrt{\frac{K_{mooring}}{\mathrm{m}_{buoy} + A(\omega)}} \tag{3.41}$$

Moreover, when the hydrodynamic damping is equal to the external damping B_{PTO}, the optimal power absorption condition is achieved (Cruz, 2008)

$$B_{PTO} = B(\omega_n) \tag{3.42}$$

Therefore, the combination of these conditions results in the highest power extraction condition under regular waves. In order to investigate these statements, two conditions are analyzed. The first condition investigates the variation of the tether stiffness and set the PTO damping to be the same as the radiation damping for each frequency, which is illustrated in Figure 3.19. The second condition is the variation of the PTO damping, and the buoy operates in a resonant condition, which is shown in Figure 3.20. For both conditions the power absorbed was calculated using Equation 2.106, the velocity was calculated using Equation 3.40, and the force used as an input is for 1-meter wave amplitude.

The first condition, which is illustrated in Figure 3.19, varies the tether stiffness. The red line represents the highest power absorbed condition value over the frequency, which was computed using a max. m function in the MATLAB code. The asterisk represents the stiffness necessary to match the natural frequency.

Figure 3.19: Stiffness Variation

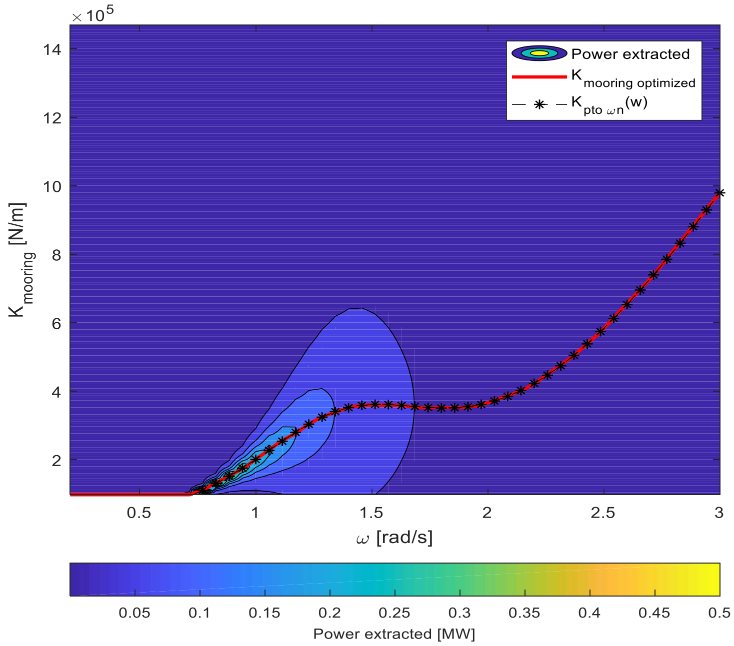

Source: Author (2017).

The second condition, which is illustrated in Figure 3.20, varies the PTO damping, while keeping the resonant condition. As in the first condition, the red line was obtained selecting the highest power absorbed value over the frequency, and the asterisk represents the Radiation damping of the Point Absorber.

Figure 3.20: Damping variation

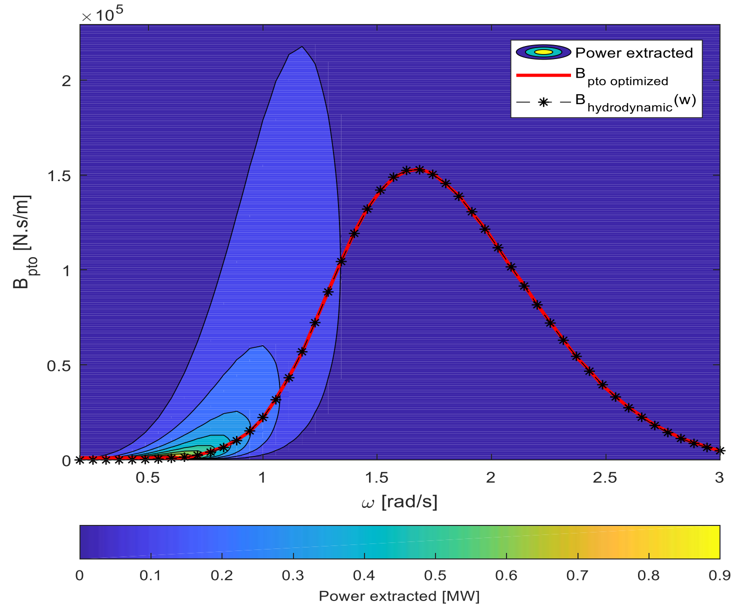

Source: Author (2017).

As stated previously, the combination of both statements results in the maximum power absorption. However, the theoretical value of optimized damping might not be achievable in practice, due to the high displacement and the limited stroke length. Therefore, the sub-optimized damping of the PTO unit depends also on the stroke length, which limits the maximum displacement of the Point Absorber. The sub-optimal PTO damping was calculated manipulating Equation 2.01, where the displacement was set to be equal to the stroke length, and the resulting damping was considered the sub-optimal condition. The resulting equation is:

$$B_{PTO\_sub\ optimal} = \frac{\sqrt{\left(\frac{|\mathbb{X}|(\omega)}{L_{stroke}}\right)^2 - \left\{K_{mooring} - \left[\mathrm{m}_{buoy} + A(\omega)\right]\omega^2\right\}^2}}{\omega} - B(\omega) \qquad (3.43)$$

Therefore, the best damping coefficient for regular waves is a combination of the optimized damping and the damping that results in the buoy displacement equals to the stroke length. Figure 3.21 shows the optimal and sub-optimal PTO damping coefficients for regular waves at different frequencies using a stroke of 6 meters long. The magnitude of the force $\mathbb{X}$ depends on the waves amplitude, which in this case was assumed to be one meter.

Figure 3.21: Limited stroke (6m) – suboptimal PTO damping.

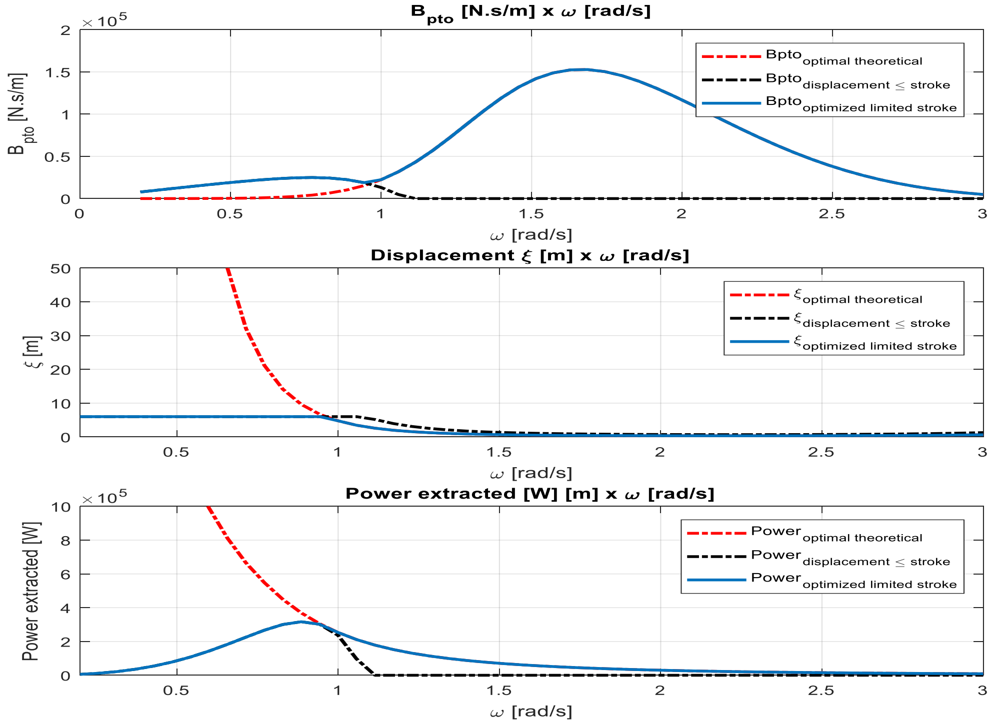

Source: Author (2017).

Considerations:

- If the optimized damping causes a displacement higher than the stroke length, the damping is equal to $B_{PTO\_sub\ optimal}$.
- Viscous forces are neglectable

Figure 3.22 compares the effect of a limited stroke in the power absorption of a Point Absorber under a 1-meter wave amplitude. The figure shows that the stroke impacts on the power absorption in lower frequencies, which requires higher displacements and possesses higher power.

Figure 3.22: Limited strokes effect on regular waves – Power absorbed

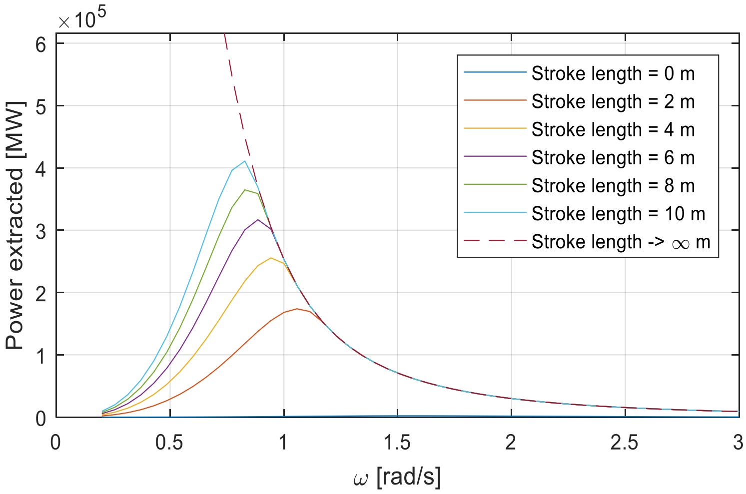

Source: Author (2017).

The next analyze investigates the mass influences on the power absorption. In this regards, the mass was varied from 50% to 150% from its actual mass $35000\ kg$, which was described in Babarit et al. (2012). The stiffness was varied in all cases to match the natural frequency of the system. The previous procedures were applied in this investigation (optimal and sub-optimal PTO damping). Figure 3.23 illustrates the power absorbed without stroke limitation on the left side, and on the right side, the power absorbed with stroke limitation.

Figure 3.23: Mass effect on regular waves – Power absorbed

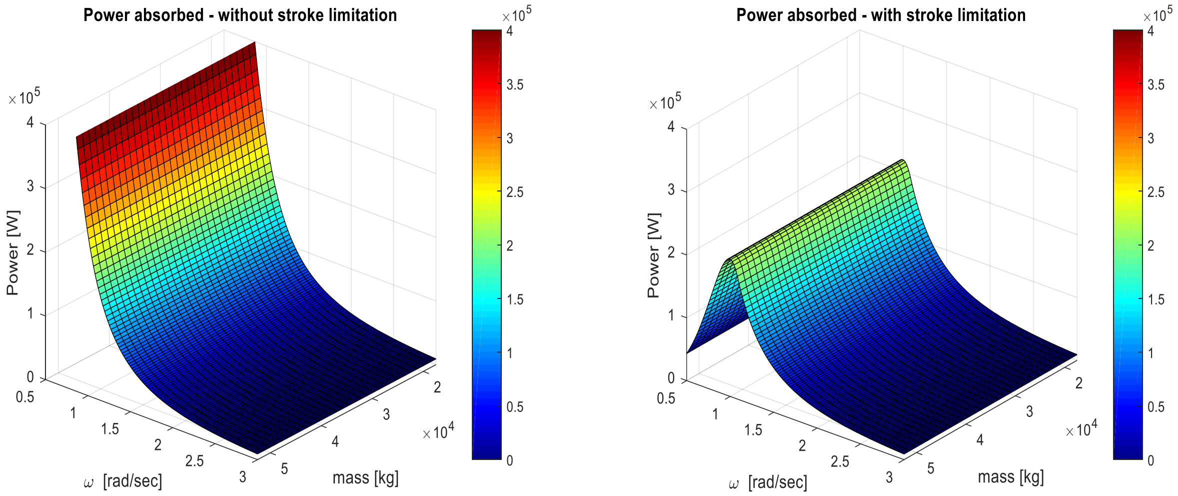

Source: Author (2017).

The Figure 3.23 shows that the power extraction in heave is independent of the mass for the Point Absorber described in this work. However, it is important to remember that the buoy mass changes the pre-tension force that affects the surge and pitch motion, which in reality can modify the power absorption. This effect is not included in the frequency domain due to the limitation of the frequency domain model, which linearizes the equations at the mean position and assumes small displacements.

3.3.2 Power extraction under irregular waves (Frequency domain)

In the frequency domain method, the nonlinear forces are neglected, which can result in enormous displacements. In order to restrict the stroke length, and create a tool to analyze if the device hits the stroke limit, an assumption is suggested: the point absorber can extract energy only if the buoy displacement is inferior to the stroke length. This assumption reduces the energy for elevated displacements. As a result, the optimal condition increases the system survivability, owing to the reduction of the system impacts to the hard stop, which is located at the end of the stroke. Moreover, without this restriction, the buoy can move out from the water without any effect in the frequency domain model. The stroke limitation is made via Gaussian distribution to determinate the probability of occurrence of a displacement lower than the stroke length. Figure 3.24 illustrates the flow chart representation, including the stroke limitation.

Figure 3.24: Flow chart representation with stroke limitation

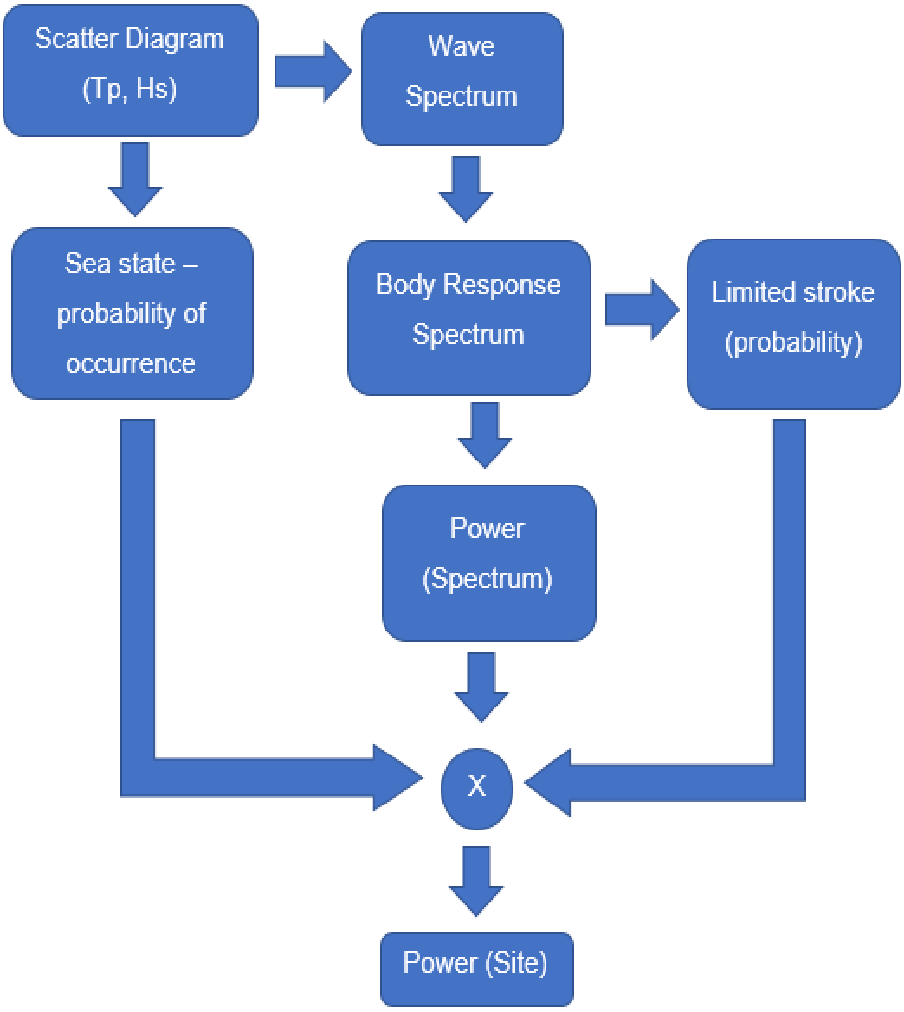

Source: Author (2017).

The source of energy was modeled previously, such as Wave spectrum and Sea State probability of occurrence, based on the scatter diagram. Therefore, in this subsection, just the following steps presented in the flow chart are conducted.

The body response is calculated using Equation 2.108, which contains the RAO function previously verified, and the power function of the sea state. Figure 3.25 shows the body response to the specified condition of:

- $Tp = 12.5\ s$
- $Hs = 2.5\ m$
- $K_{mooring} = 64\ kN/m$
- $B_{PTO} = 64\ \mathrm{N.s/m}$

Figure 3.25: PSD of the wave spectrum and the Point Absorber

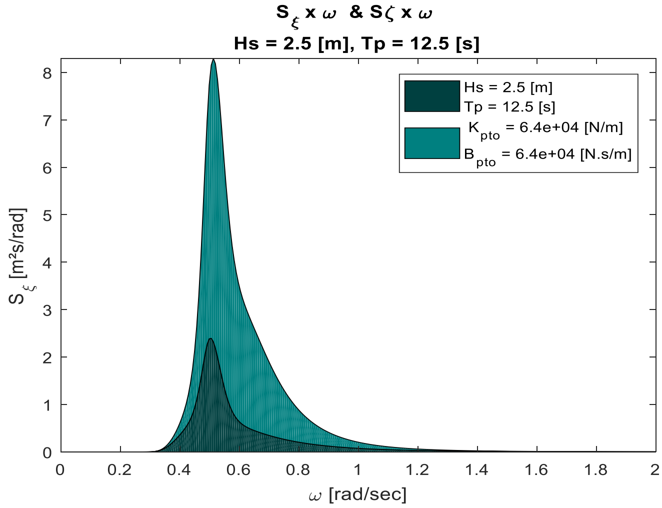

Source: Author (2017).

It can be observed that the motion of the buoy is larger than the wave in the condition specified. The body response is converted to displacement ξ using the same procedure as Equation 2.54, and the power in each frequency is calculated as:

$$P(\omega) = \frac{1}{2} B_{PTO} * \left|\dot{\xi}(\omega)\right|^2 \qquad (3.44)$$

Where,

$$\left|\dot{\xi}(\omega)\right|^2 = |\xi(\omega) * \omega|^2 \qquad (3.45)$$

Figure 3.26 shows the power result of the same condition specified in Figure 3.25. It is important to notice that the frequency discretization impacts the plot according to Equation 2.61, which in this example $d\omega = 0.007 \text{ rad/s}$.

Figure 3.26: Power – single condition - Sea State

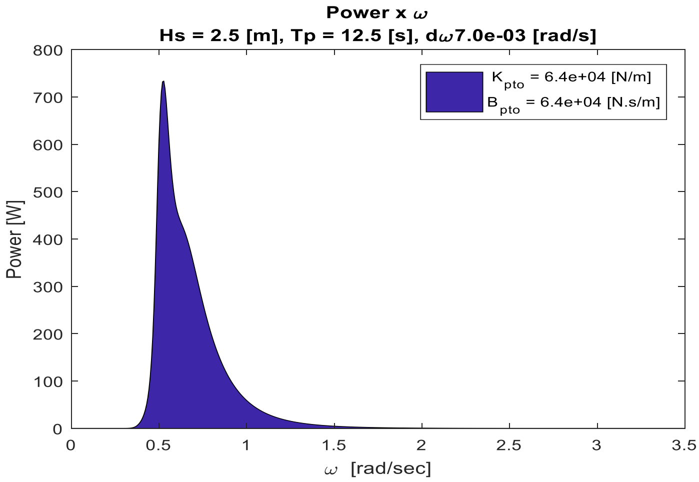

Source: Author (2017).

The power extracted from the specified sea state was calculated using Equation 2.109, and the result for this example was:

$$P_{mean} = 25.97\ \mathrm{kW}$$

The power extracted including stroke limitation at a specific spectrum is assumed to be equal to the power extracted from the sea state multiplied by the probability of occurrence a displacement inside the stroke limit:

$$P_{extracted} = Prob\left\{-\frac{L_{stroke}}{2} \leq \varsigma(t) \leq \frac{L_{stroke}}{2}\right\} * P_{mean} \tag{3.46}$$

The probability distribution of Point Absorber displacement is calculated according to Parseval theorem that relates the frequency domain to the time domain, which was described in Equation 2.66 and Equation 2.74 respectively. Figure 3.27 illustrates buoy response in time domain generated using a random phase angle and based on the power spectrum density; and on the right side, the probability distribution of displacements. As defined by Babarit et al. (2012), the stroke has a length of 6 meters, which is used during this analyzes.

Figure 3.27: Time domain representation and probability distribution – Condition 1

$Hs = 2.5\ [m], Tp = 12.5\ [s]$

$K_{pto} = 64\ [\mathrm{k}N/m], B_{pto} = 64\ [\mathrm{k}N.s/m]$

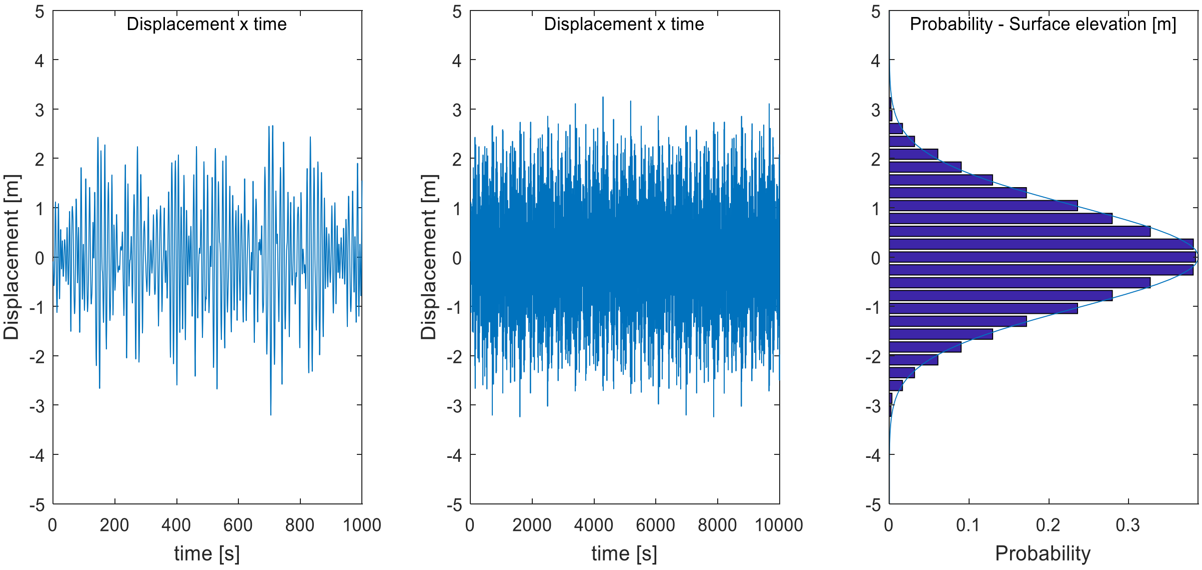

Source: Author (2017).

As illustrated in Figure 3.27, the limited stroke presented a minor impact on the power extraction for the specified PTO configuration, because the buoy displacement was nearly within the stroke limits. However, for a wave condition with a superior wave height, and/or a PTO with a lower damping, the Point Absorber tends to move higher than the stroke length. Figure 3.28 illustrates the buoy displacement in the time domain and the probability distribution of the displacements, for a lower damping coefficient, where the stroke length is important.

Figure 3.28: Time domain representation and probability distribution – Condition 2

$$Hs = 2.5\ [m], Tp = 12.5\ [s]$$

$$K_{pto} = 64\ [\mathrm{k}N/m], B_{pto} = 32\ [\mathrm{k}N.s/m]$$

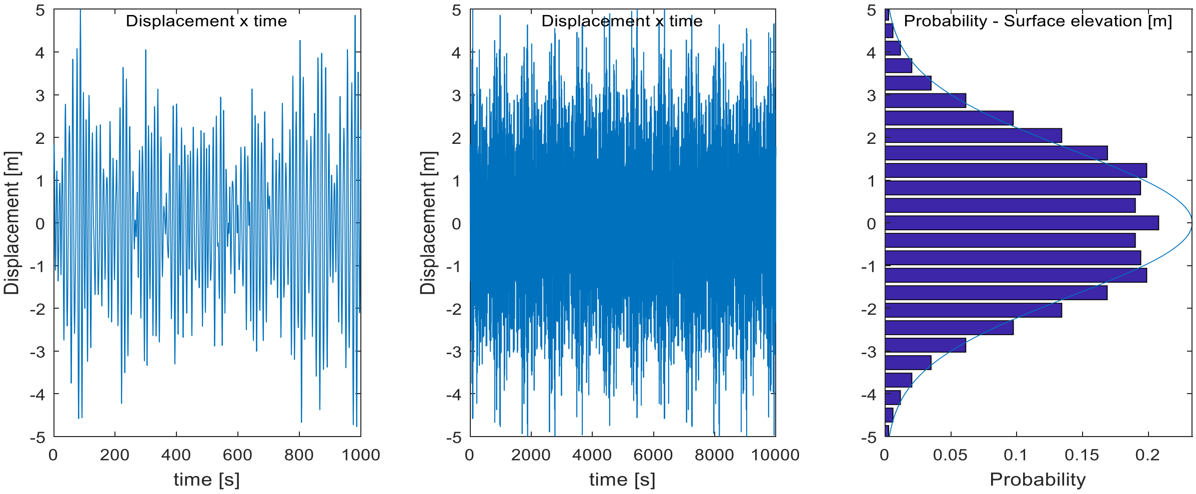

Source: Author (2017).

3.3.2.1 Optimal power – site – Frequency domain

The selection of the best optimal stiffness and damper is made calculating the power absorbed for several stiffness coefficients and damping coefficients. This work based on Babarit and Hals (2011) to define the range of interest, which is specified in Table 3.3:

Table 3.3: The range of parametric analysis of the PTO coefficients.

	$K_{mooring}\ kN/m$	$B_{PTO}\ kN.s/m$
Minimum	20	10
Maximum	200	200

Source: Babarit and Hals (2011).

The range of parametric analysis was discretized into 60 elements, and for each condition, the same procedure to calculate the mean power of the spectrum was applied using a loop function to cover the entire range of combinations. Figure 3.29 illustrates the power extracted for the specified sea state condition, with and without the stroke limitation. The condition selected on the graph represents the body response condition simulated in Figure 3.26.

Figure 3.29: Power – sea state optimization

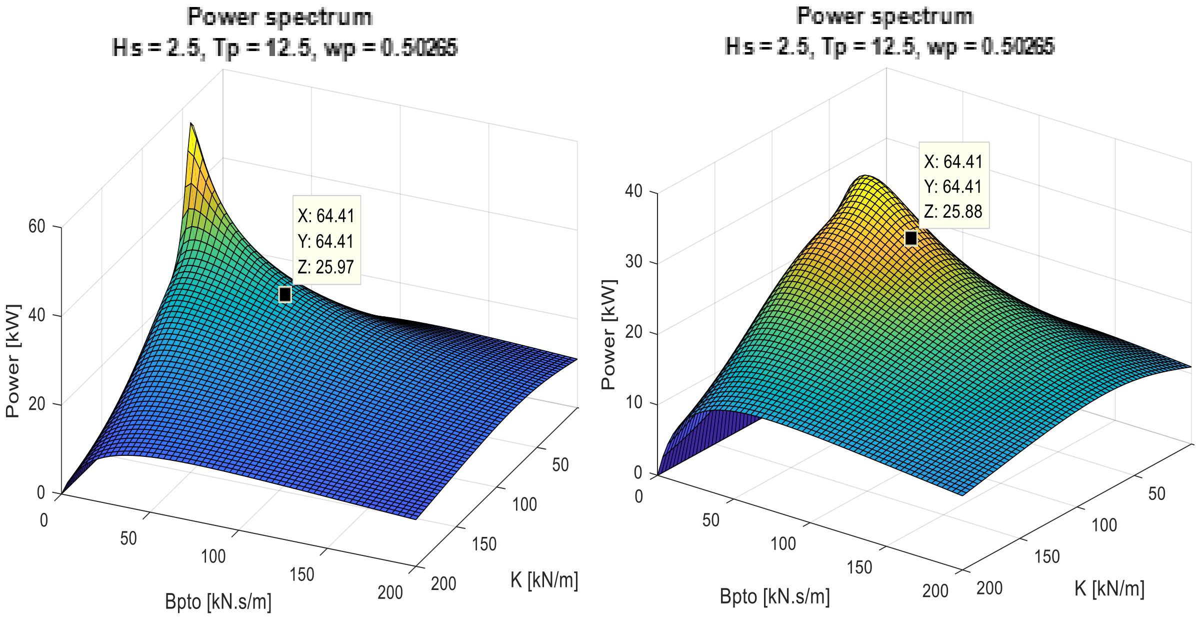

Without stroke limitation

With stroke limitation

Source: Author (2017).

Finally, the site power absorbed is calculated multiplying the power of each sea state by its respective probability of occurrence and the probability of a displacement within the stroke length, and summing all sea states contributions. Figure 3.30 illustrates the power extracted from the site for the entire range of PTO coefficients with and without the stroke limitation.

Figure 3.30: Power – site optimization

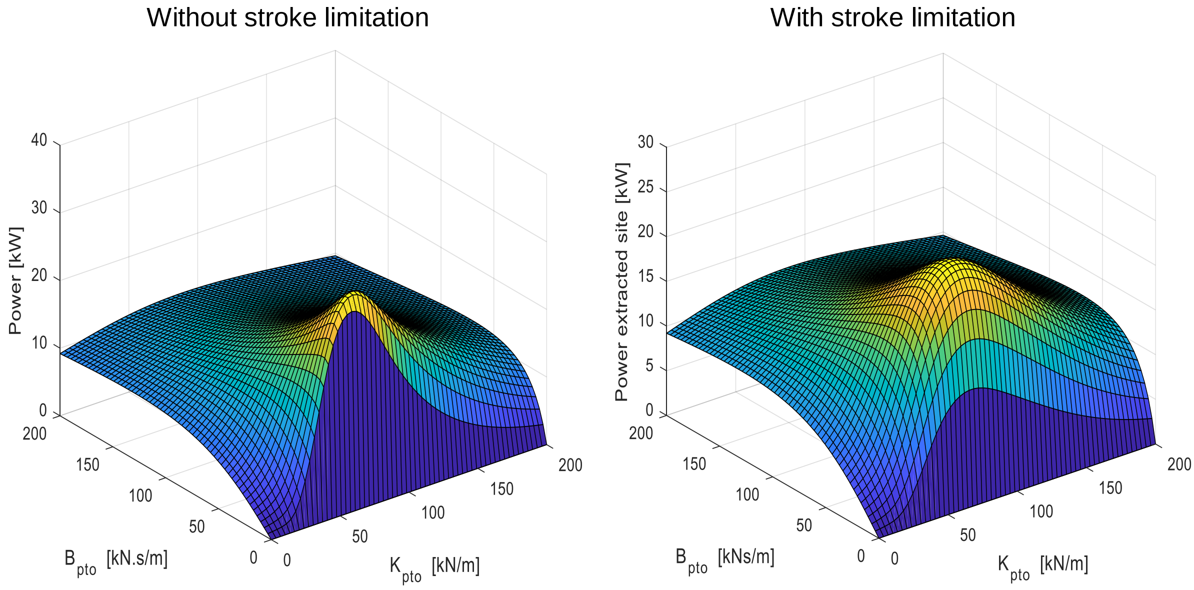

Source: Author (2017).

It can be observed that the maximum power of the site occurs for the following conditions:

Without stroke limitation:

- B_{pto} = 10.1 [kN.s/m]
- K_{tether} = 64.4 [kN /m]
- P_{mean}= 31.1 [kW]

With stroke limitation:

- B_{pto} = 27.1 [kN.s/m]
- K_{tether} = 74.5 [kN /m]
- $P_{extracted}$= 25.2 [kW]

As expected, in order to decrease elevated displacements and maintain suitable power extraction, the damping coefficient is higher for the setting with stroke limitation. The stiffness of the system is nearly identical, as it depends mostly on the wave period to match the natural frequency.

3.3.3 Power extraction under irregular waves (Spectrum domain)

As mentioned in the literature review, the spectrum domain uses the frequency domain model as an initial guess. Therefore, the model described previously is used as an initial guess to start the iteration to estimate the viscous damping. The drag coefficient used to estimate the viscous damping was the same as in Babarit and Hals (2011):

- $C_D = 1$
- $\rho = 1025\ [\mathrm{kg}/m^3]$
- $S_{\mathrm{Area}} = 38\ [m^2]$

The relaxation rate (Equation 2.114) for convergence was set to be 0.5. The displacements in spectral domain were calculated using Equation 2.113. Figure 3.31 compares the Point Absorber PSD with and without viscous damping. It can be verified that the viscous force has a large impact on the body motion for high displacements.

Figure 3.31: PSD comparison – with and without viscous force

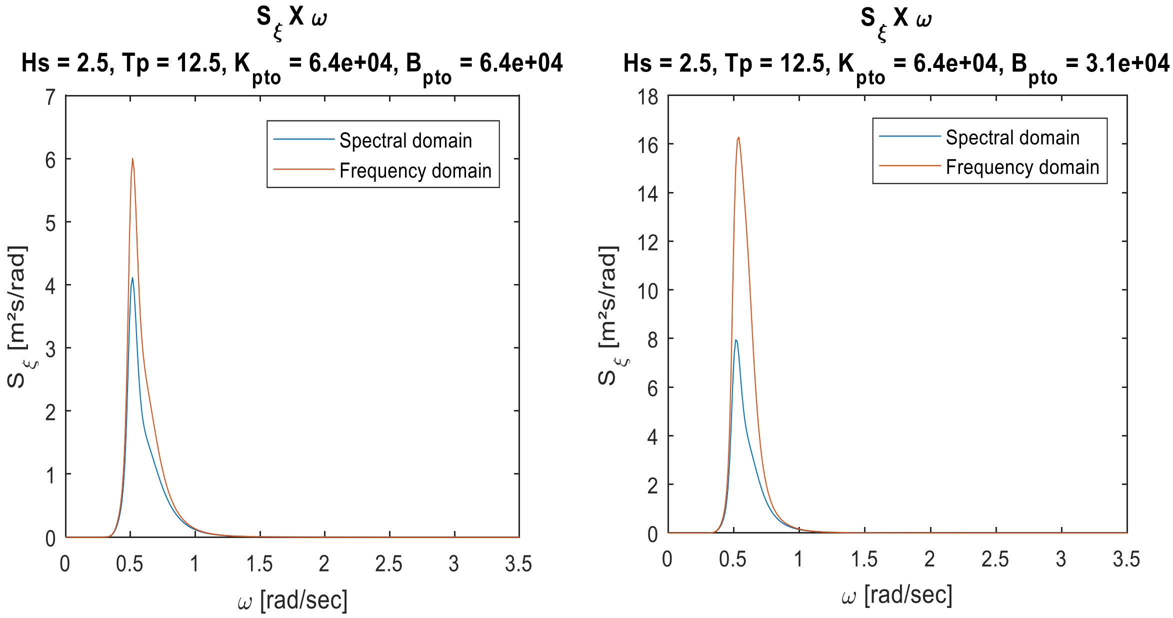

Source: Author (2017).

The tool that limits the displacement is also included in this model to estimate the influence of the stroke length. However, as the displacement is reduced due to viscous drag, the stroke limitation effect is nearly neglected for a stroke length equal to 6m. Similarly to the analysis in Frequency domain, the power extracted is obtained following the procedures described in the flowchart in Figure 3.24. Figure 3.32 shows the power absorbed in a sea state on the left side, and the power absorbed in the site on the right side.

Figure 3.32: PTO optimization

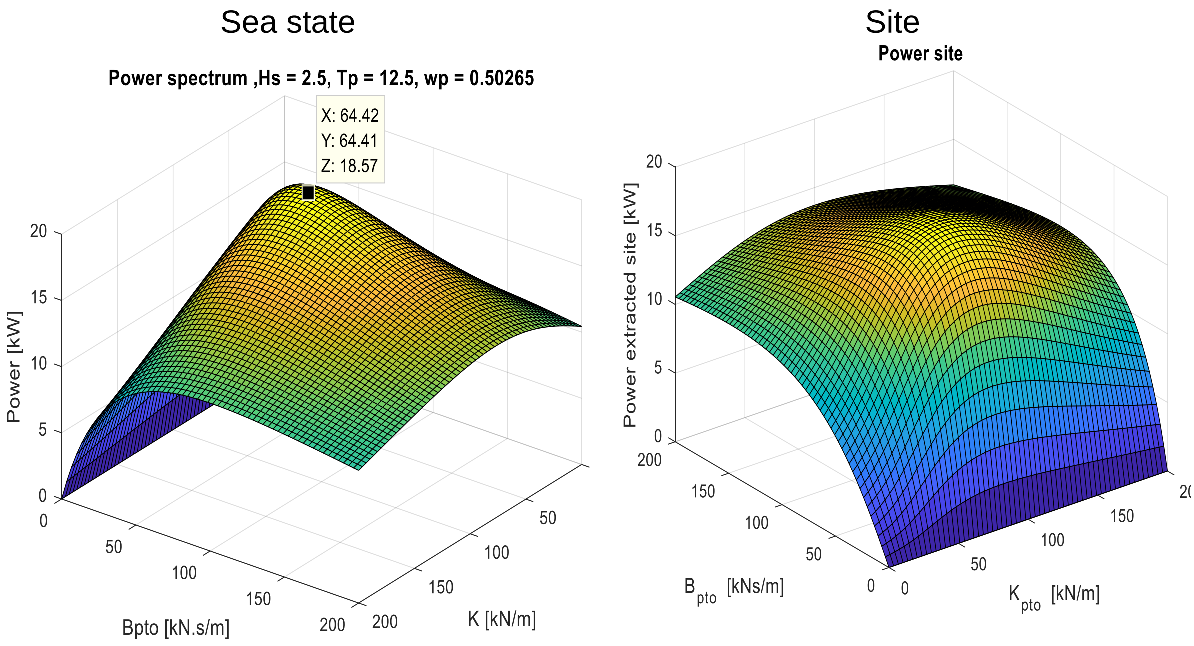

Source: Author (2017).

It can be observed that the maximum power of the site occurs for the following conditions:

- B_{pto} = 67.8 [kN.s/m]
- K_{tether} = 88.1 [kN /m]
- P_{mean}= 18.7 [kW]

3.3.4 Variable stiffness and damping

In this analysis, it is investigated the effect of a variable stiffness and damping to enlarge the power absorption. The proposed a control system identifies the sea state (Tp and Hs), via analyzes of the sea elevation and adjust the best PTO configuration. The control is slow and simple to implement, thus it should be considered in the design (Babarit and Hals, 2011).

The selection of the best stiffness and damping coefficients for each sea state was calculated previously, which is illustrated on the left side of Figure 3.32. The results of the best PTO configurations for each Tp and Hs are illustrated in Figure 3.33.

Figure 3.33: PTO optimization – site – with stroke limitation

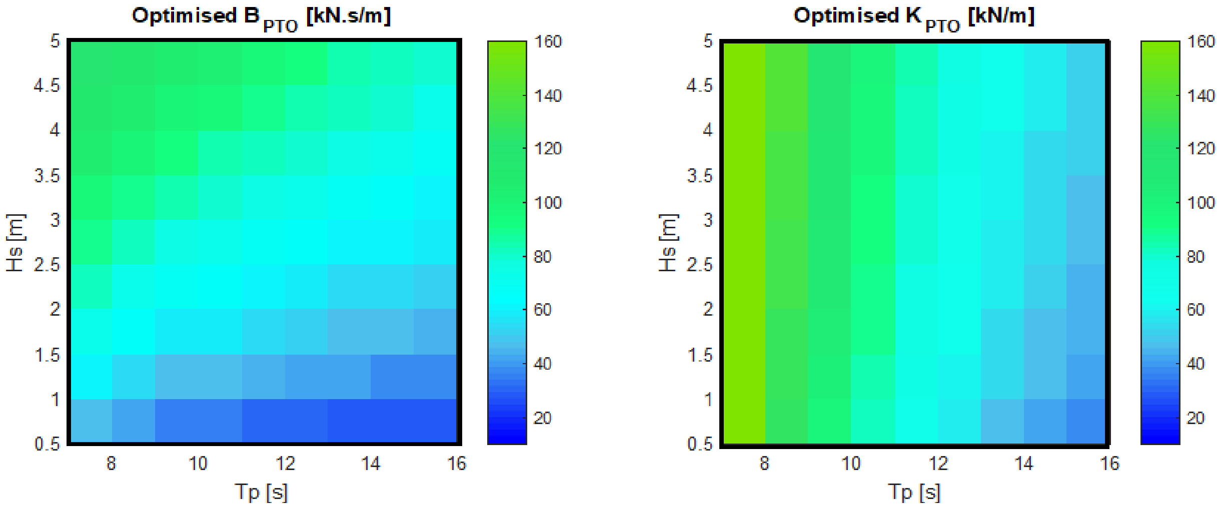

Source: Author (2017).

As stated before, the stiffness coefficient varies mainly with the wave period to tune the natural period of the system. On the other hand the damping coefficient changes due to the radiation damping and wave height to reduce the total displacement. The results are consistent with Babarit and Hals (2011), which is illustrated in Figure 3.34. The results presented in Babarit and Hals (2011) used a time domain method which included three degrees of freedom and viscous drag.

Figure 3.34: Power optimized (sea state) by Babarit and Hals (2011)

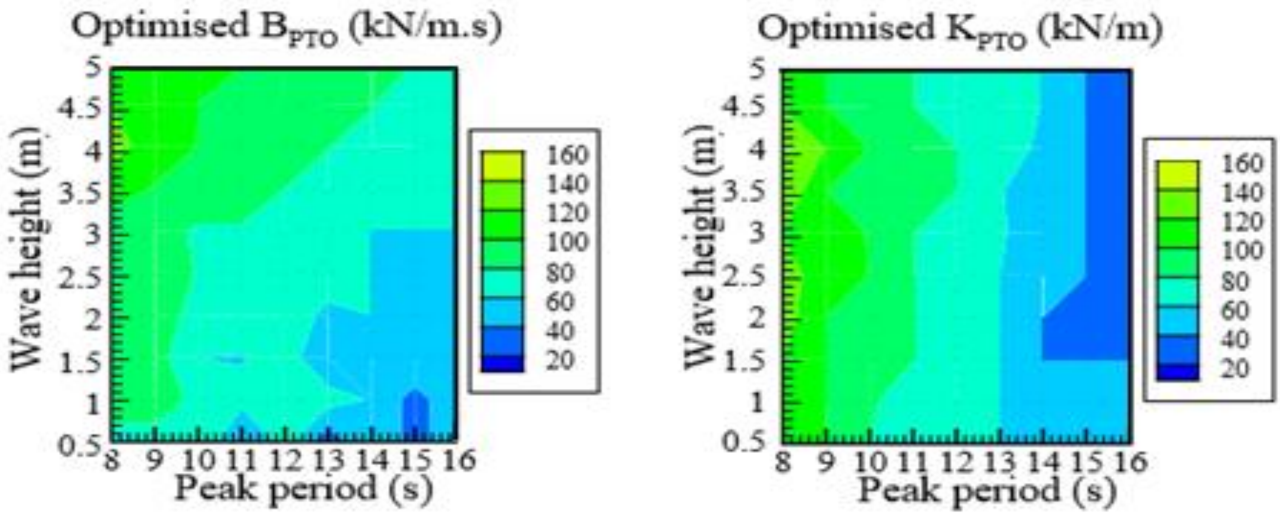

Source: Babarit and Hals (2011).

The mean optimized power absorbed at each sea state using the optimal PTO coefficients is illustrated on the left side of Figure 3.34.The results are comparable to Babarit and Hals (2011), which is illustrated on the right side of Figure 3.35.

Figure 3.35: Mean Absorbed Power (optimized for each sea state)

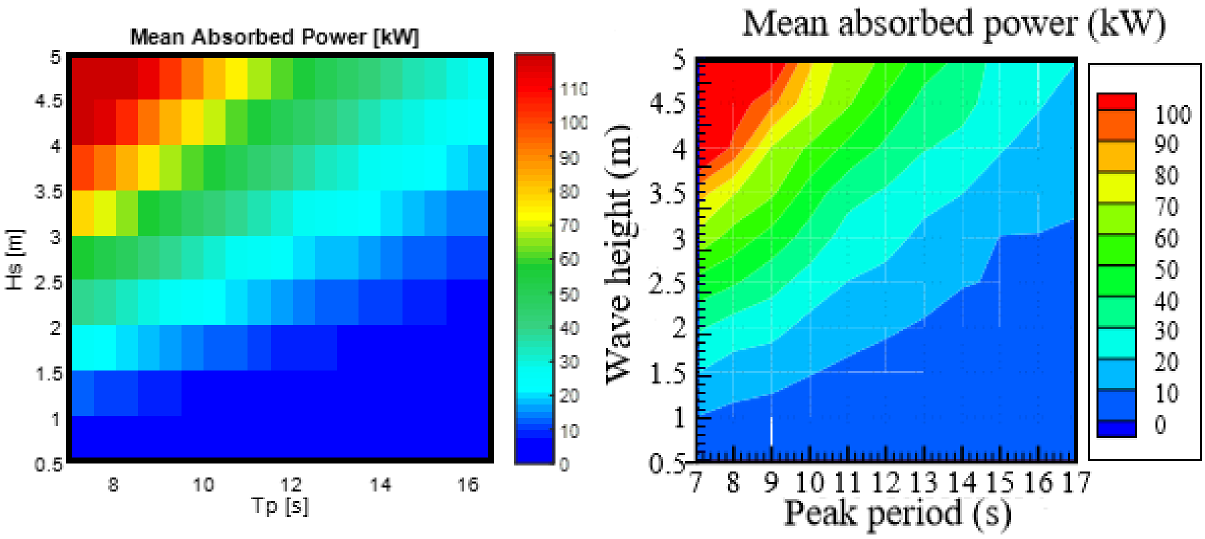

Source: Author (2017). Source: Babarit and Hals (2011).

The multiplication of the mean optimized power absorbed by each sea state by its respective probability of occurrence results in the mean optimized power absorbed of the site, which is equal to:

- P_{mean}= 19.5 [kW]

Assuming that the control system operates properly, the power absorbed increases 4.3% compared to the optimal fixed PTO coefficients. The improvement in the energy absorption is low due to the sea state distribution that is concentrated. However, for others sea sites, where the sea states are more distributed, the control can improve the energy substantially.

3.3.5 Verification and viscous drag influence

The verification of the viscous drag influence was conducted analyzing the data provided by Babarit and Hals (2011). The Point Absorber specifications were the same, and the sea state was also described using a JONSWAP spectrum ($\gamma = 3.3$). During the study, the authors varied the drag coefficient and investigated the effects on the power extraction. For each case, it was calculated the maximum absorbed power base on the optimum condition in each sea state. Figure 3.36 illustrates the effect of the viscous drag, where the nominal drag coefficient used is one.

Figure 3.36: Mean absorbed power x viscous damping coefficient (Yeu)

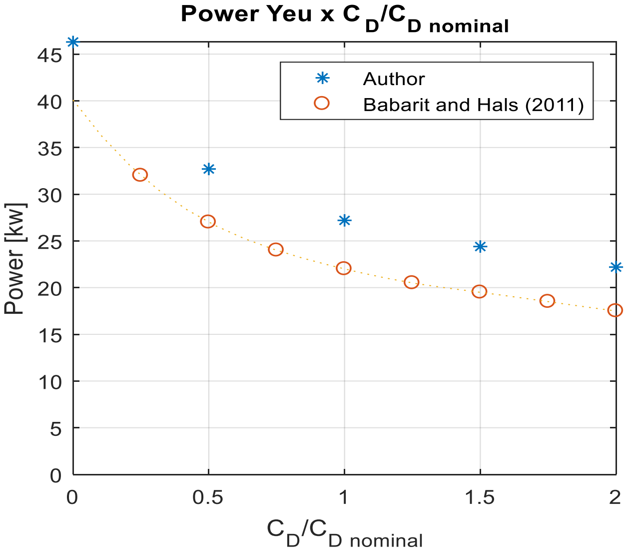

Source: Author (2017).

The results show a correlation in the curve tendency. However, the spectral domain model has a power overestimation of 20% compared to the time domain model. Hence, assuming that this time domain model would be used to calculate the power in Imbituba, and the overestimation was the same, the power extracted in would be approximately 15 kW.

The same sensitivity analysis was conducted in Imbituba. The nominal value of drag coefficient was divided by two, and doubled to estimate the range of reliability. The results show that the power extracted is estimated to be 18.7 kW [+20, -20%].

3.3.6 Stroke limitation effect

The tool developed in this work allows the investigation of the stroke limitation on the power absorbed. In this regards, the stroke length was varied to check if the Point Absorber hits the stroke limit, which is analyzed via the reduction of the power absorbed. Table 3.4 presents the results of a fixed PTO configuration in Imbituba.

Table 3.4: Stroke limitation x Power absorbed.

Stroke length $[m]$	**B_{pto} $[\mathrm{kN.}s/\mathrm{m}]$**	**K_{tether} [kN /m]**	**P_{mean} [kW]**
7	67.8	88.1	18.7
6	67.8	88.1	18.7
5	71.2	88.1	18.5
4	74.5	91.5	18.4

Source: Babarit and Hals (2011).

It can be observed that a stroke length of 7 meters has the same performance as a stroke of 6 meters, with the same optimal condition. This result shows that the Point absorber does not hit the stroke limits and the power extraction is not limited due to the stroke length. On the other hand, if the stroke length is reduced to 5 or 4 meters, it will change the best coefficients for power extraction. However, the optimal power has a neglectable reduction in the power extraction. This event occurs because the increase of damping reduces the total displacement which also reduces the viscous forces. In case of biofouling at the buoy, the damping should increase its damping to reduce the velocity that reduces to the viscous drag.

3.3.7 Results

Capture Width is a quantity used to evaluate the WECs performance. The parameter measures the ratio of the total mean power absorbed to the mean power per unit of crest wave width. As the buoy geometry has 7 meters of radius, the power absorbed is divided by seven times the wave power. Table 3.5 compares the power absorbed at different locations according to Babarit et al. (2012).

Table 3.5: Performance comparison

Site	**SEMREV**	**EMEC**	**Yeu**	**Lisbon**	**Belmullet**	**Imbituba***
Annual mean absorbed power [kW]	8.8	18.5	22.0	19.0	31.0	18.7 - 15.0
Capture width ratio (%)	9	13	13	8	6	11 - 9

Adapted from Babarit et al. (2012).

The first value of the Imbituba absorbed power refers to the results calculated in this work using spectrum domain, and the second is an approximated extrapolation of Babarit et al. (2012) results. In both cases, the point absorber operates in an appropriated range of efficiency compared to other sites. The main difference is the use of a fixed PTO optimized for the entire sea, instead of an optimized PTO configuration for each sea state using a control system.

3.3.8 Comparison of results

Table 3.6 presents the power extraction results calculated in this work. The frequency domain method does not include viscous drag, therefore, it results in high power and low damping. Moreover, the stroke limitation affects the response. On another hand, the viscous drag is important for the Spectrum domain method, which results in higher optimal damping to limitate the viscous losses. Futhermore, the power extraction is not limited by the stroke length.

Table 3.6: Comparison of results

Optimization	**Model**	K_{tether} **[kN/m]**	B_{pto} **[kN.s/m]**	P_{mean} ***[kW]***	**Limitations**
Site	Frequency domain	64.4	10.1	31.1	-
Site	Frequency domain	74.5	27.1	25.2	Stroke limitation
Site	Spectrum domain	88.1	67.8	18.7	-
Site	Spectrum domain	88.1	67.8	18.7	Stroke limitation
For all sea states	Spectrum domain	Figure 3.33	Figure 3.33	19.5	Stroke limitation

Autor (2017).

4 FINAL CONSIDERATIONS AND FUTURE WORK

Renewable sources of energy exerts an important role in the risen demand of energy due to the limited reserve of fossil fuels and environmental awareness. The ocean waves have a substantial amount of power, which can contribute to the future of energy production. The aim of this project was to design a fully submerged Point Absorber in Santa Catarina. Firstly, the wave resources of Imbituba site were assessed. Secondly, the mathematical modeling of the proposed WEC device was derived, and the assumption to simplify the model was applied, which resulted in a single degree of freedom. Finally, sensitivity studies were conducted to estimate the best stiffness and damping and estimate the best configuration.

From the wave resource analyses, it was concluded that Imbituba presents a feasible location for wave energy implementation with a power estimated at 24 kW of wavefront. One of the advantages is the concentrated sea state probability that reduces the operating range of the WEC device. As a result, the optimized variable stiffness and damper do not increase considerably the energy extraction compared to the fixed optimal parameters. Hence, a fixed PTO configuration can be used in Imbituba, resulting in an efficiency similar to other sites with optimized variable PTO.

The stroke reduction had a neglected power loss. Even with a lower efficiency at higher damping, the reduction of the buoy displacement minimized the viscous losses, which resulted in a similar power extraction of higher displacement. Moreover, at a stroke length equals to 6 meters, no reduction in the power due to the limited stroke is experienced.

For future works, the optimization of the buoy size, geometry, and economic assessment are can result in a valuable information. Repeat the analysis in Time Domain, including more degrees of freedom. Methods to reduce the cost associated with the construction, and reduce the biofouling at the bouy. Vortex-induced vibrations. Comparison between other WEC devices.

5 REFERENCES

AGENCIA NACIONAL DE ENERGIA ELÉTRICA (ANEEL). **Programa de Incentivo às Fontes Alternativas.** Criado pela Lei nº 10.438/2002, o Proinfa tem o objetivo de aumentar a participação de fontes alternativas renováveis. Available in: <http://www.aneel.gov.br/proinfa>. Accessed in: 22 jun. 2017.

AQWA THEORY MANUAL (ANSYS). **Aqwa can simulate linearized hydrodynamic fluid wave loading on floating or fixed rigid bodies.** Aqwa can estimate the equilibrium characteristics and static and dynamic stability of coupled (by moorings and/or connectors) bodies under steady state environmental loads. Available in: < http://148.204.81.206/Ansys/150/Aqwa%20Theory%20Manual.pdf>. Accessed in: 22 jun. 2017.

ALVES, M.; MELO, E. Measurement and modeling of wind waves at the northern coast of Santa Catarina, Brazil. **Bras. Oceanogr**., v.49, p.13-28, 2001.

BABARIT, A.; HALS, J.; MULIAWAN, J.; KURNIAWAN, A.; MOAN, T.; KROKSTAD, J. Numerical benchmarking study of a selection of wave energy converters. **Renewable energy**, v. 41, p. 44-63, 2012.

BABARIT, A.; HALS, J. **Numerical estimation of energy delivery from a selection of Wave Energy Converters -** Bottom reference submerged heave buoy report, 2011.

BRAZIL PORTAL. **Energia renovável terá prioridade em financiamentos do BNDES.** Banco vai manter em até 80% sua participação em projetos de eficiência energética e extinguirá apoio a térmicas a carvão e óleo. Available in: <http://www.brasil.gov.br/economia-e-emprego/2016/10/energia-renovavel-tera-prioridade-em-financiamentos-do-bndes>. Accessed in: 22 jun. 2017.

CARNEGIE CLEAN ENERGY LIMITED. **Carnegie is the 100% owner and developer of the CETO Wave Energy Technology.** EMC specialises in the delivery of mixed renewable energy microgrid projects to islands and remote and fringe of grid communities. Available in: < http://carnegiewave.com/>. Accessed in: 22 jun. 2017.

CHAKRABARTI, K. **Hydrodynamics of offshore structures**. Illinois: Springer, 1987.

CONSTESTABILE, P.; FERRANTE, V.; VICINANZA, D. Wave Energy Resource along the Coast of Santa Catarina (Brazil). **Energies**, v. 8, p. 14219-14243, 2015.

CORNETT, M. A global wave energy resource assessment. **International offshore and polar engineering conference Vancouver**, 2008.

CRUZ, J. **Ocean Wave Energy Current Status and Future Perspectives**. Bristol: Springer, 2008.

DE BACKER, G. **Hydrodynamic Design Optimization of Wave Energy Converters Consisting of Heaving Point Absorbers**, Dissertation submitted to obtain the academic degree of Doctor of Civil Engineering Ghent University, 2009.

DREW, B.; PLUMMER, A.; SAHINKAYA, N. A review of wave energy converter technology, **Power and Energy**, v. 223, n. 782, p. 887-902, 2009.

FALCÃO, O. Wave energy utilization: A review of the technologies, Renewable and Sustainable. **Energy Reviews**, v. 14, p. 899–918, 2010.

FALNES, J. A review of wave-energy extraction. **Marine Structures**, v. 20, p. 85–201, 2007.

FOLLEY, M.; WHITTAKER, T. Spectral modelling of wave energy converters. **Coastal Engineering**, v. 57, p. 892-897, 2010.

FOLLEY, M. Numerical Modelling of Wave Energy Converters . **State of the Art Techniques for Single Devices and Arrays**, Elsevier, 2016.

FUJARRA, C. Lecture notes of **Dinâmica de Sistemas II** Subject, University of São Paulo, 2009.

FUJARRA, C. Lecture notes of **Hidrodinâmica Aplicada II** Subject, Federal University of Santa Catarina, 2017.

HIBBELER, C. **Mechanics of Materials.** 8. Ed. Boston: Pearson, 2011.

HIBBELER, C. **Engineering Mechanics Dynamics**. 14. Ed. Prentice Hall, 2015.

JEFFERYS, R. Device characterization. **Power from sea waves**. Academic Press, p. 413–438, 1980.

JOURNÉE, J.; MASSIE, W. **Offshore Hydromechanics**. 1. Ed. Delft University of Technology, 2001.

KARIMIRAD, M. Offshore Energy Structures For Wind Power. **Wave Energy and Hybrid Marine Platforms**. New York: Springer, 2014.

LI, Y.; YU, H. A Synthesis of Numerical Methods for Modeling Wave Energy Converter-Point Absorbers. **Renewable and Sustainable Energy Reviews,** v. 16, p. 4352–4364, 2012.

MAIS ENERGIA SC**. Programa Catarinense de Energias Limpas**. Available in: <http://www.scmaisenergia.sc.gov.br/sds/>. Accessed in: 22 jun. 2017.

MINISTÉRIO DE MINAS E ENERGIA(MME). **Programa de incentivo às Fontes alternativas de energia elétrica.** Diversificação da matriz energética brasileira, aumentando a segurança no abastecimento. Available in: <http://www.mme.gov.br/programas/proinfa/galerias/arquivos/apresentacao/PROINFA-ANEXO1-InstitucionalMME.pdf> Accessed in: 20 jun. 2107.

MULTON, B. **Marine Renewable Energy Handbook.** 1. Ed. Wiley, 2012.

PARKINSON, S.; DRAGOON, K.; REIKARD, G.; GARCIA-MEDINA, G.; OZKAN-HALLER, T.; BREKKEN, A. Integrating ocean wave energy at large-scales: A study of the US Pacific Northwest. **Renew Energy,** v. 76, p. 551–559, 2015.

PAWLOWSKI, M. Sea spectra revisited, **10th International Conference on Stability of Ships and Ocean Vehicles**, v. 10, p. 463–472, 2009.

PECHER, A.; KOFOED, P. Handbook of Ocean Wave Energy, **Ocean Engineering & Oceanography**. 7. Ed. Springer Open, 2016.

PELC, R.; FUJITA, M. Renewable Energy from the Ocean. **Marine Policy**, v. 26, p. 471-479, 2002.

RAO, S. **Mechanical Vibrations.** 5. Ed. Prentice Hall, 2011.

SARPKAYA T.; ISAACSON M. **Mechanics of wave forces on offshore structures**. Van Nostrand Reinhold, 1981.

SADRAEY M.; VERLAG M. **Aircraft Performance Analysis**. Saarbrücken VDM, 2009.

XIE, J.; ZUO, L. Dynamics and control of ocean wave energy converters. **Int. J. Dynamic Control,** v. 1, p. 262–276, 2013.

6 APPENDIX A - ADDED MASS AND RADIATION DAMPING

Hydrodynamic Added Mass and Radiation Damping

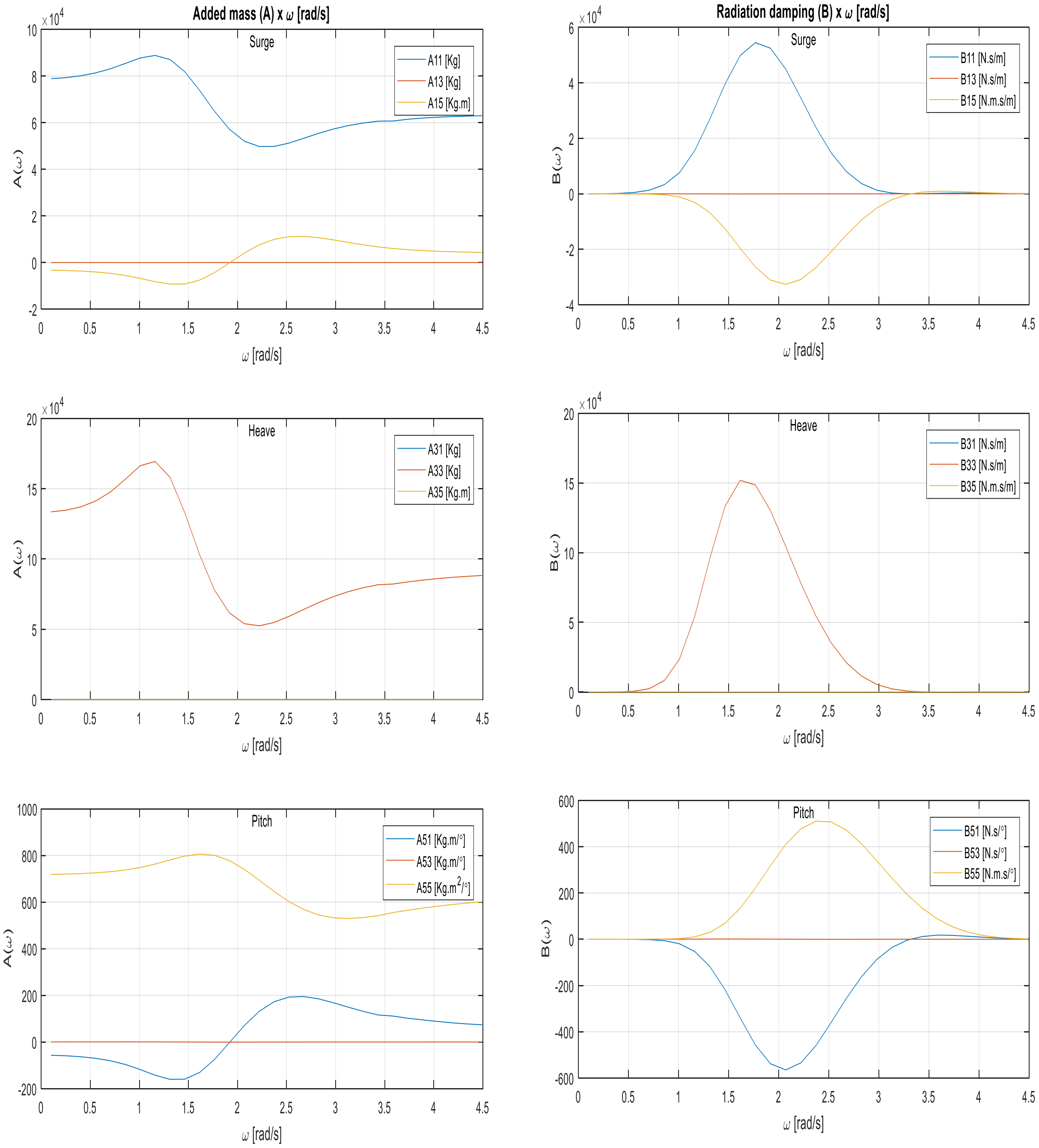

7 APPENDIX B - EXCITATION FORCE

Excitation force - $\varsigma_a(\omega) = 1\,m$

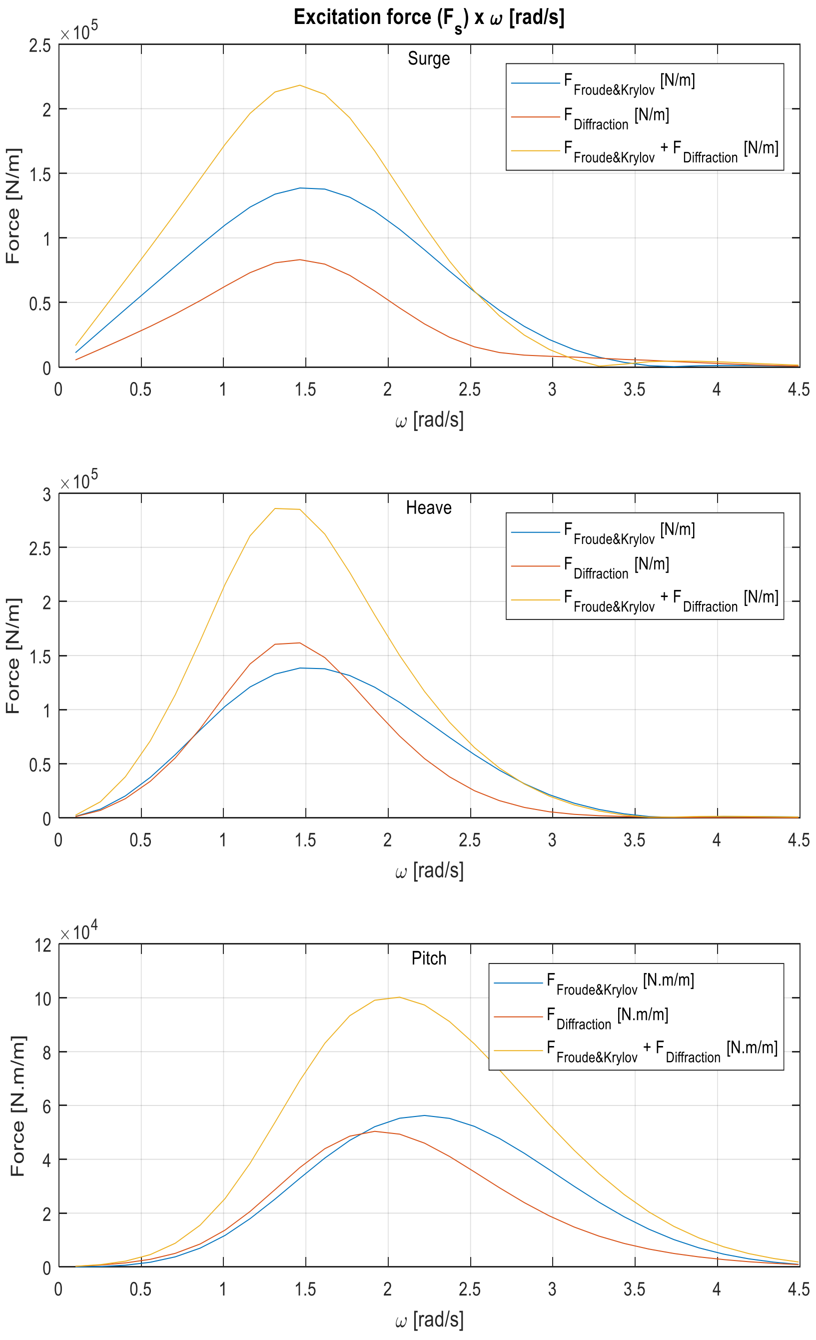

8 APPENDIX C - MESH STUDY

Hydrodynamic added mass - vertical axis

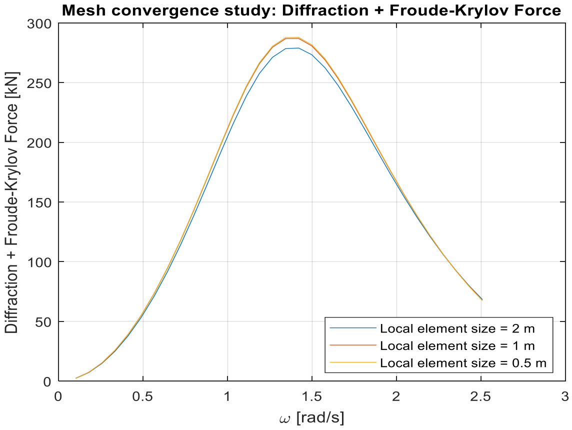

Radiation damping – heave motion

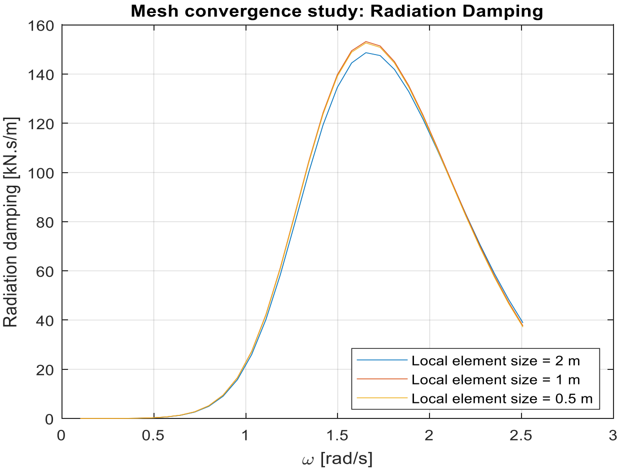

Excitation force – heave motion